



Tomas Bata University in Zlín
Faculty of Technology

Doctoral Thesis

Preparation and Characterization of Antibacterial Surfaces

Příprava a charakterizace antibakteriálních povrchů

Author: **Ing. et Ing. Kateřina Sulovská**

Study programme: P2808 Chemistry and Materials Technology
Study field: 2808V006 Technology of Macromolecular Compounds

Supervisor: doc. Ing. Marián Lehocký, Ph.D.

Zlín, March 2016

© Kateřina Sulovská

Klíčová slova: *antibakteriální aktivita, polyetylen, roubování, plazma, spektroskopie, charakterizace povrchu*

Key words: *antibacterial activity, polyethylene, grafting, plasma, spectroscopy, surface characterization*

Acknowledgement

I would like to express my deep and sincere thankfulness to associated professor Marian Lehocký for his constant support and patience throughout my doctoral studies. I am very grateful to him for the opportunity to work on such practical topic and the opportunity to learn a lot from him.

It is my great pleasure to thank all of my colleagues who helped me during the doctoral study – František Bílek for his help during initial experiments, Alena Kalendová and Jana Bartošová for their help with characterization techniques.

I would also like to thank my colleagues Marie Nedvědová, Hana Chudá and Silvie Bělašková for their moral support during my studies, their ideas and time spent in laughter.

Last but not least, my greatest gratitude belongs to my mum for her support, encouragement and ultra-all-inclusive service at home during my study, especially in time of exams and when finishing my doctoral study; and my dog Dášenka for her undying love and patience throughout my studies.

“Everything you can imagine is real.”

Pablo Picasso (1881 – 1973)

Resumé

Předložená dizertační práce se zabývá přípravou aktivních antibakteriálních povrchů na bázi nízkomolekulárního polyetylenu opracovaného nízkoteplotním plazmatem. Takto předpřipravené materiály byly vystaveny parám vybraných funkcionalizačních monomerů a následně ponořeny do připravených roztoků antibakteriálních činidel, jež byly v minulých pracích vyhodnoceny jako nejefektivnější, a které jsou zároveň i často používanými v komerční praxi. Účinnost vytvořených antibakteriálních povrchů byla charakterizována a zkoumána vybranými dostupnými metodami, např. FTIR spektroskopií, skenovací elektronovou mikroskopií nebo terahertzovou spektroskopií, jež patří mezi novější experimentální metody studia materiálů a mezi jejíž přednosti patří zejména studium mezimolekulových sil. Samotný antibakteriální efekt a jeho účinnost byla ověřena pomocí agarového difúzního testu, jenž je při dodržení postupů považován za stejně efektivní jako dlučnická metoda a patří mezi normované postupy; veškeré vytvořené materiály byly testovány na zástupci gram pozitivních a negativních bakterií. Z výsledků provedených experimentů lze konstatovat, že vytvořené materiály obsahující antibakteriální látky chlorhexidin a triclosan vykazují účinnost vůči růstu vybraných bakteriálních kmenů, zatímco materiály obsahující heparin a fucoidan účinnost neprokázaly.

Summary

Submitted doctoral thesis is dealing with a preparation of active antibacterial surfaces based on a low-density polyethylene pre-processed in a low-temperature plasma. Such prearranged material were exposed to selected functionalization monomers' vapours and consequently immersed into prepared solutions of antibacterial agents that were evaluated as most effective in previous testing, and which are commonly used in the commercial praxis at the same time. Efficacy of these antibacterial materials was studied by chosen methods, e.g. the FTIR spectroscopy, the scanning electron microscopy or the terahertz spectroscopy belonging to newer experimental methods for material study, with advantage in intermolecular forces detection. The antibacterial effect and its activity was verified by the agar diffusion test (standardized method), which is considered to be same effective as the dilution method while meeting the conditions during preparation; all materials were tested on representative of gram positive and negative bacterial strains. Results of our experiments showed that materials with antibacterial compounds chlorhexidine and triclosan embody efficiency against selected bacterial strains growth, while materials containing heparin and fucoidan did not prove its effectivity.

Content

Acknowledgement.....	4
Resumé.....	6
Summary	7
Content	8
1. Introduction.....	10
2. Current state of topic.....	11
3. Aim of work.....	16
4. Materials and Methods.....	17
4.1 Antibacterial and other agents.....	17
4.2 Testing microorganisms	20
4.3 Methods	22
4.3.1 Plasma treatment.....	22
4.3.2 Terahertz spectroscopy	35
4.3.3 Terahertz imaging	43
4.3.4 Fourier-transform infrared spectroscopy	46
4.3.5 X-ray photoelectron spectroscopy	52
4.3.6 Surface wettability and contact angle measurement.....	57
4.3.7 Scanning electron microscopy	63
4.3.8 Antibacterial activity assessment.....	68
4.4 Experimental setup	69
5. Results	74
5.1 Contact angle measurement.....	74
5.2 SEM.....	76
5.3 ATR-FTIR	78
5.4 XPS.....	82
5.5 Antibacterial activity	83
5.6 Terahertz spectroscopy.....	88

6. Contribution of work.....	100
7. Conclusion.....	101
List of references.....	103
List of figures	125
List of tables.....	126
List of symbols and abbreviations	127
Author's publication activities.....	133
Curriculum Vitae.....	134

1. Introduction

Health-care associated infections (HCAIs) are generally taken as one of the reason for patients' re-operations, serious health complications and deaths worldwide, connected not only to variety of surgeries or joint replacements but also to birth mortality. As the health-care was very unsatisfactory before the 1800's, the progress in medical care and access to hospital also took HCAIs into account. Between late 1800's and 1900's the mortality in hospitals was higher than 50 % and stayed high until 1860. In years 1880 – 1930, 11 patients out of 35 died due to various causes (with *Staphylococcus aureus* infections on 1st place). In contrast to mortality < 4% nowadays, between 1960's and 1970's the death rate was c. 25 %. On the other side stand standard infections (urinary – 40 %, wound 25 %, nosocomial pneumonia 20 %) [1] and infections from used medical items, e.g. bloodstream infections originated from central venous catheters in 87 % [2]. To lower this negative trend, antibacterial agents were an ideal solution for HCAIs' decrease to acceptable limits.

During past decades, plastic materials were created and are nowadays widely used in many different applications instead of metal, wooden or glass materials. One of such application spheres is medicine or food industry. Polymer materials have many advantages (e.g. low weight, durability, controlled surface architecture), and can be easily modified. An extensive research of polymeric materials for use in medicine (or food industry) is being made to be able to control the biodegradability of such materials and to lower the vulnerability to bacterial attachment to their surface.

Therefore, this doctoral thesis deals with preparation of active surfaces via multistep physicochemical approach suitable for medical use, their detailed characterization; and possible attachment of organic compounds that may be parts of multilayer thin films.

2. Current state of topic

Creating materials with antibacterial potential or features for main usage in biomedical applications (Table 1) is nowadays widely studied. So far, mostly studied and prepared materials are used for joint replacement, implants, impregnation of medical devices, antibacterial materials for various items (catheters, foils, etc.), or personal hygiene.

Generally polymers used in medicine are vulnerable to bacterial attack, respectively adhesion onto surface, which makes utilization of polymers without antibacterial treatment a disadvantage. Bacterial adhesion can be described in five basic steps (Figure 1), studied in aqueous conditions applicable to other environments, beginning with bacteria-surface interactions (1) resulting in stable bacteria attachment on the surface with monolayer formation (2) and clustering bacteria into micro-colonies with multi-layering cells (3). Then, cells produce extracellular secretion which demonstrate biofilm formation with characteristic “mushroom” formed of polysaccharide (4) (or “column-and-canopy” shaped biofilms). After achieving maximal bacteria number, the biofilm rupture (cells start to detach) and bacteria spread to the environment as a planktonic mode of growth (5). Furthermore, other organisms may attach to biofilm. [1],[3],[4],[5]

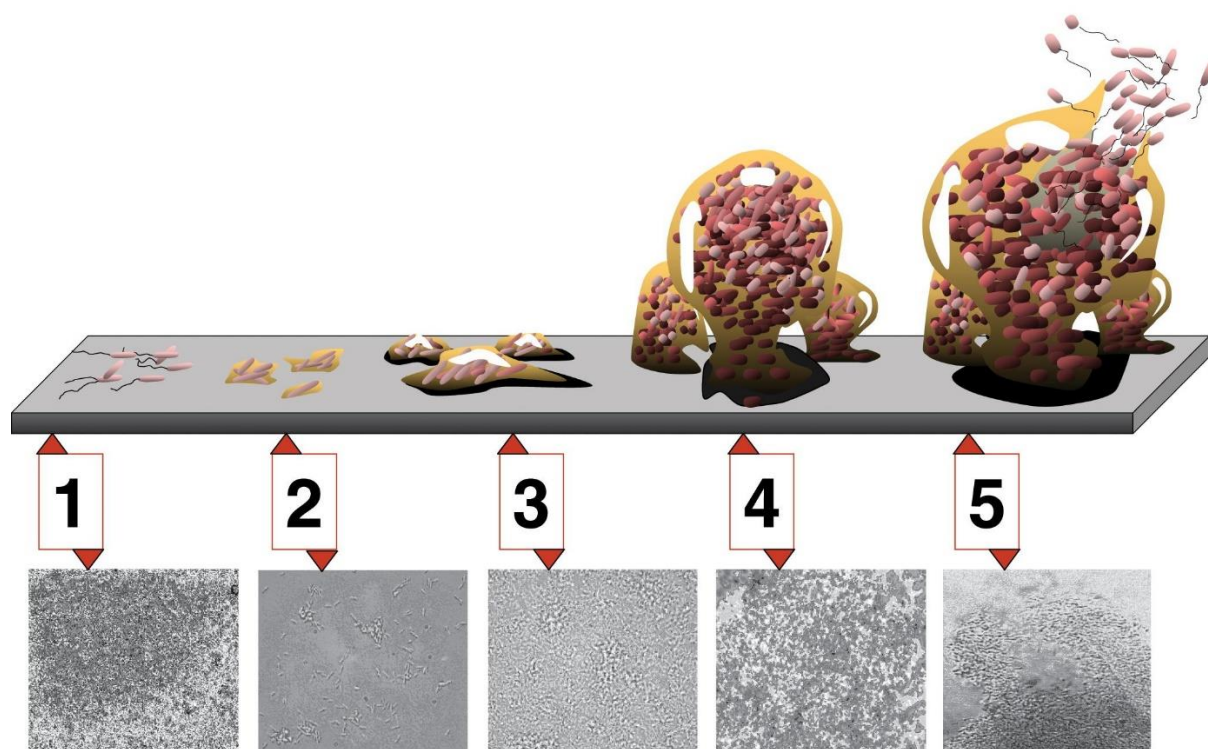


Figure 1 Bacterial colonization stages [1]; 1 – Conditioning phase (sec.), 2 – Irreversible attachment (sec. – min.), 3 – Maturation phase 1 (hrs. – days), 4 – Maturation phase 2 (hrs. – days), 5 – Distribution phase (hrs. - days – months)

Adhesion of bacteria onto polymeric surface depends on [1],[6],[7],[8]:

- Bacteria (strain, growth, conditions, surface charge and energy).
- Surface (chemical composition, surface charge and energy, topology).
- Environment (pH, temperature, presence of oxygen and other compounds, hydrodynamic parameters).

Table 1 Commonly used polymers in medicine [1]

Polymer	Application
Polyethylene	Orthopaedic implants, containers, catheters, non-woven textiles
Polypropylene	Disposable items, non-woven textiles, membranes, sutures
Polyurethanes	Films, tubing, catheters
Polyvinylchloride	Catheters, tubing
Polyamides	Sutures, packaging, dental implants
Polyethylene terephthalate	Sutures, artificial vascular grafts
Polycarbonates	Containers, construction material
Poly(methyl methacrylate)	Membranes, implants, bone cement parts
Polydimethylsiloxane	Implants, catheters
Polytetrafluoroethylene	Artificial vascular grafts
Polyether ether ketone	Tubing
Poly lactide	Resorbable implants

To obtain functional antibacterial system, several ways of modification is possible, whether it is a chemical, physical or combination attempt. If an antibacterial modification is needed, following factors should be considered [1]:

- Polymer properties (chemical and physical).
- Envisaged utilization (humidity, temperature, pH, roughness, etc.).
- Selected antimicrobial agent (toxicity, thermal stability, affinity, economy).
- Technological factors (reproducibility, functionality, complexity).
- Financial factors (certification, costs, possible margin).

There are four main processes to obtain antibacterial material [1],[9],[10]:

- Modification without antibacterial agent (wet chemistry or high energy electromagnetic radiation) – no antibacterial effect.

- Direct deposition of antibacterial agent onto surface (used immediately before treatment in a form of solution or ointment) – very low efficacy.
- Surface modification and chemical deposition of antibacterial agent (deposition of antibacterial agent onto surface after pre-activation, or by the help of a relevant mediator) – efficient over a long period of time.
- Bulk modification of polymer with antibacterial agent (not more than 20 % of antibacterial agents directly incorporated into polymer matrix) – low efficiency.

Selection of antibacterial agent depends on many factors including the application methods and possible contaminants. Antibacterial agents may act as bacteriostatic (inhibits only microorganisms' growth) or bactericidal (affects death of microorganisms) compounds. [11]

Following text divides antibacterial applications of interest, respectively surface modification and chemical deposition of antibacterial agent process, into two bigger groups. The first group of antibacterial applications is connected with joint replacements, where the target is not only inhibition of bacteria growth (or kill bacteria in early stages of adhesion before creating biofilm) but also avoidance of loosening without infection (so called aseptic loosening caused e.g. by osteoclasts). The main task for antibacterial agents in joint implants is reduction of bacterial adhesion and prosthetic infections leading to re-implanting (re-operating) subjected joint, which can further contribute to re-infection and re-operations. Therefore coatings and their combinations such as silver ions, nitride oxide, antibiotics (vancomycin, gentamicin), antiseptics (triclosan, octenidin), antimicrobial peptides or drugs (strontium), chitosan, titanium oxide, heparin, and calcium phosphate is utilized; these compounds can be anchored onto surface by different approaches (e.g. grit-blasting, acid etching, plasma or thermal spraying, sputter coating, pulsed laser deposition, dip-coating, electrophoretic deposition, hot isostatic pressing and ion beam assisted deposition). As the bacteria protein's adhesion and consequent colonisation is higher on metallic surfaces, surfaces with higher surface energy (hydrophilic) or surface with roughness (values exceeding a threshold of 0.2 μm) and nanoscale architecture (silver nano-pins, microspheres etc.), the adjustment of antibacterial agent is justified. However, some of the agents may cause corrosion (silver, titanium compounds), oxidation (nitride oxide) or may create weak positive charges (chitosan); some need UV or visible light to produce ions and act bactericidal/bacteriostatic (titanium oxide). Commonly used applications are to inhibit or completely suppress following

bacteria strains: *Staphylococcus aureus*, *Escherichia coli*, *Shigella flexneri*, *Acinetobacter baumannii*. In most cases, antiseptic agents act as effective as antibiotics. [12]

The second group of antibacterial surface is dealing with inhibition of bacterial growth or killing existing bacteria without any other special functions. This group comprises in majority of cases pre-activation of future active antibacterial material by cold plasma treatment. Cold plasma (e.g. dielectric barrier discharge) was selected for its high cleanliness, increase in material hydrophilicity, no changes in bulk polymer as only the uppermost layer is modified, environmental friendliness, and relative inexpensiveness. The atmosphere used during experiments varies according to intended surface structure, where the increase in roughness is higher with gaseous atmosphere like argon, nitrogen, oxygen, helium than with air [13]. On the other hand, air plasma treatment is more effective in incorporating oxygen containing groups and reducing contact angle because an oxidized cross-linked structure is not made [14]. During plasma treatment, wide spectrum of ions, electrons, excited neutrals, radicals, metastable molecules and UV radiation appears and influences the material [14],[15],[16]. This leads to enhanced adhesive properties of modified surface (several μm) exploitable for deposition to functionalization layer [17]. Some researches revealed decreased hydrophilicity with time due to diffusion of the hydrophilic functional groups into the bulk material (regeneration to original state) [1],[18], others studied plasma enhanced oxidative degradation reactants of polyethylene (H_2 , H_2O , CO_2 , CO) [19] that are substantially lower than in case of polyethylene terephthalate and polyimide. In some cases, such reaction happens during transfer (contamination) from plasma generator after initial modification of samples [20],[21], or a secondary contamination by microorganism product [9]. The longer the plasma treatment (> 5 min.), the higher the surface damages, the greater the degradability of the material and changes in melting point and brittleness. The morphology change is greater after longer treatment (> 20 min) due to breaks in LDPE chain, possible cross-linking, free radicals formation, etc. No change in crystallinity was observed in short-time treatment of LDPE. The ideal storage of plasma treated surface is under 20 % relative humidity and 20 °C not to boost aging and rearrangements of the structure (although the surface, according to treatment, in less than 1 hours begins to re-arrange). [21],[22] The most mentioned antibacterial agents are: triclosan, bronopol, chlorhexidine, silver nanoparticles (respectively ions), zinc or copper, chitosan, pectin, nisin, essential oils, (cationic antimicrobial) peptides, minocycline-rifampin, etc. [7],[9],[10],[16],[18],[23],[24],[25],[26],

[27],[28],[29]. The antibacterial activity baseline is set to 24 hours, but most of manufactured surfaces stays active for at least 3 weeks, but some as in case of [24] exhibit functionality for 6 weeks or as in [2] a one year shelf-life (continue to inhibit at satisfactory level).

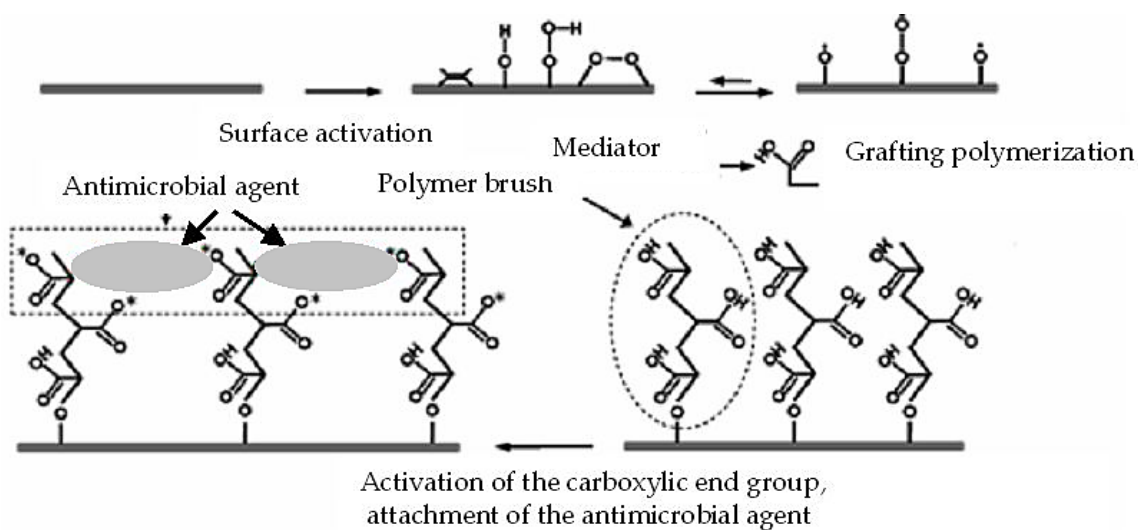


Figure 2 General process of antibacterial agent immobilization onto pre-activated surface [1],[30]

3. Aim of work

The aim of this work is the study of active antibacterial surfaces (low-density polyethylene (LDPE) as a base) preparation and consequent characterization. LDPE was chosen for its acceptable flexibility, transparency, easy processability, thermal stability, recyclability, good properties, and inexpensiveness. The multistep physicochemical approach is used to graft different monomers onto the plasma treated reactive surface to create monomer brush to bond selected antibacterial agents. Such samples are characterized by several methods.

Following monomers were selected for functionalization of the LDPE:

- Allylamine ($\text{H}_2\text{C}=\text{CH}-\text{CH}_2-\text{NH}_2$).
- *N*-Allylmethylamine ($\text{H}_2\text{C}=\text{CH}-\text{CH}_2-\text{N}(\text{H})\text{CH}_3$).
- *N,N*-Dimethylallylamine ($\text{H}_3\text{C}-\text{N}(\text{CH}_3)-\text{CH}_2-\text{CH}=\text{CH}_2$).

As antibacterial agents, compounds as these were selected:

- Triclosan.
- Chlorhexidine.

Bacterial representatives were chosen as follows:

- *Escherichia coli*.
- *Staphylococcus aureus*.

The further work contains utilization of a Terahertz spectroscopy (Attenuated total reflection and transmission mode, imaging), and study/description of created materials via this technique is one of the key tasks of this thesis.

Furthermore, an attempt to create surfaces that are can also act antibacterial with inhibiting the bacterial adhesion to the surface with other beneficial abilities, e.g. anticoagulant or thromboresistat effects. These experiments contain fucoidan and heparin bonded onto the pre-activated surfaces with allyl alcohol ($\text{HO}-\text{CH}_2-\text{CH}=\text{CH}_2$) vapours bonded, which could serve for wider range of medical applications (e.g. skin cancer treatment, blood thinning).

4. Materials and Methods

4.1 Antibacterial and other agents

Chlorhexidine

Chlorhexidine, 1,6-Di(*N-p*-chlorophenylbiguanidino)hexane, became the “gold standard” for infection reduction and prevention due to its effectivity in many applications. It is a broad-spectrum antimicrobial effective against gram-positive and negative bacteria, facultative anaerobes and aerobes, yeasts, protozoa and some lipid-enveloped viruses which are mostly connected with HCAs. [31] Chlorhexidine is commercially available in variety of concentrations (from 0.5 to 4 %) and formulation and is contained in many products [32],[33],[34]. At low concentrations, the membrane integrity is affected which results in cell death, while at high concentrations the cytoplasmic contents precipitate, congeal or solidify [35]. The benefit in contrast to antibiotics is no resistance, therefore long-term usage is possible. Chlorhexidine is deactivated by anionic compounds. The toxicity for mammalian cells and possibility of sensitivity to chlorhexidine is evaluated as minimal ($LD_{50} = 2000$ mg/kg for rat, oral route; $LD_{50} = 1260$ mg/kg for mouse, oral route). [36]

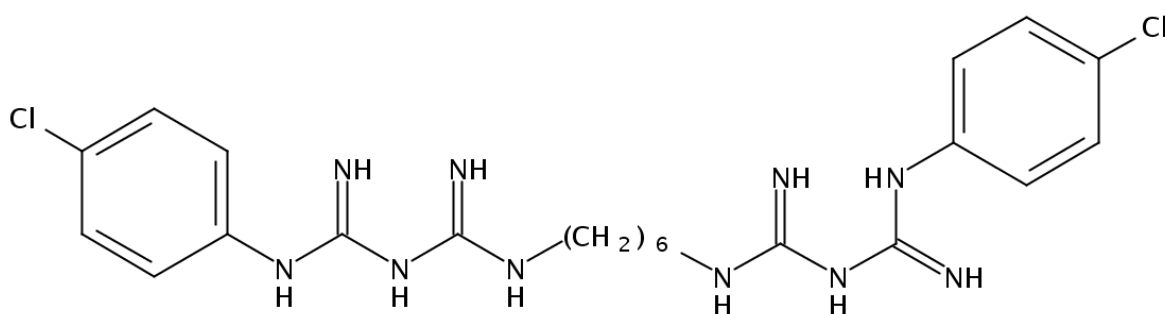


Figure 3 Chlorhexidine's chemical structure [Source: SciFinder]

However some disadvantages of chlorhexidine and products containing it (CHX) are known. Some studies provided evidence that CHX is (cyto)toxic for variety of cell types (e.g. leukocytes and kidney cells, human (dermal) fibroblasts, periodontal tissues) [37],[38], may alter macrophages functions [39], accumulate in natural biofilm [40], or cause other health problems due to its degradation product (e.g. *p*-chloroanilin) [41].

On the other hand, CHX serves since 1950s in health care environment with one of the best effectiveness as mentioned above [42], where CHX provides better antibacterial/antiseptic activity than other commonly used agents (e.g. povidone

iodine, sodium hypochlorite) [43],[44]. CHX are mainly used in e.g. dentistry as mouth rinses [45] and toothpastes, in medical care [46],[47] as surgical scrubs, health care personnel soaps, preoperative skin preparations, skin antiseptics, skin cleaners, wound protectants, catheter-connected infections [48], burn ointments, and can be found in applications like acne creams, cosmetic preservatives, ophthalmic solutions or animal ear cleaning treatment.

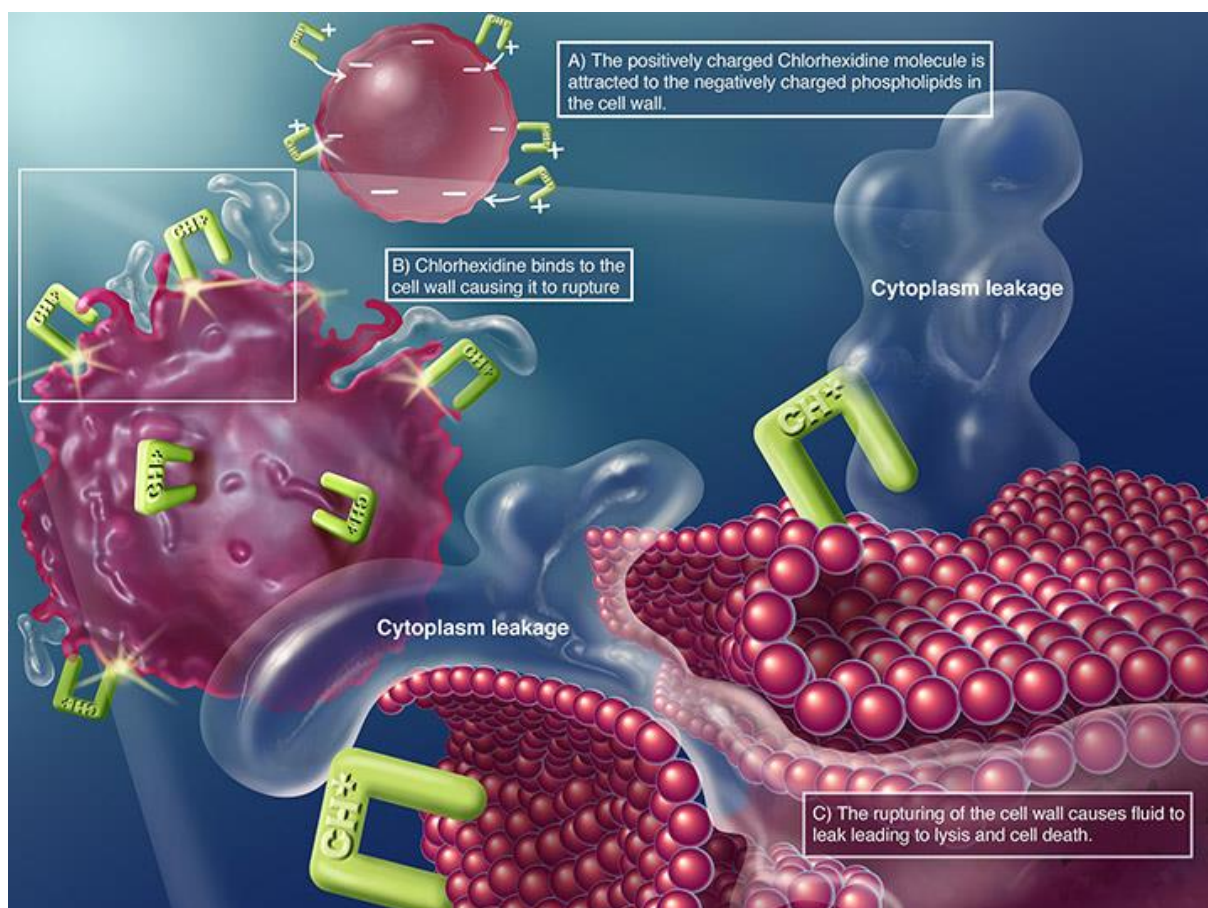


Figure 4 Mechanism of chlorhexidine action [Source: <http://chlorhexidinefacts.com/>]

Triclosan

2,4,4'-Trichloro-2'-hydroxydiphenyl ether, is used as an broad-spectrum antibacterial agents in many products such as soaps, toothpastes, dishwashing liquids, cosmetics, fabrics, plastics, pesticides and others for more than 50 years. Triclosan can therefore be a preservative, fungicide and biocide. The advantage of utilization of triclosan is its ability to control the colonization of methicillin-resistant *S. aureus* in clinical settings, on the other hand some bacteria are intrinsically resistant to triclosan, such as *P. aeruginosa*, *S. enterica* (serovar

Typhimurium), *E. coli* mutants, *A. baumannii* or bacterial endospores. Triclosan is a highly stable chemical, being extremely resistant to high and low pH, but is readily degraded via photodegradation to eight photoproducts that may be toxic. [49]

The antibacterial effect of triclosan in lower concentrations is demonstrated by binding to the enzyme (enoyl-acyl carrier protein reductase, ENR) involved in fatty acid synthesis, the nicotinamide adenine dinucleotide (NAD⁺) binds and prevent this enzyme from participating in the synthesis cycle, which results in inhibition of bacterial cell growth. [50] At high concentrations, triclosan demonstrates itself as a biocide (bacteriostatic) with multiple cytoplasmic and membrane targets (e.g. membrane destabilizing effects). [51]

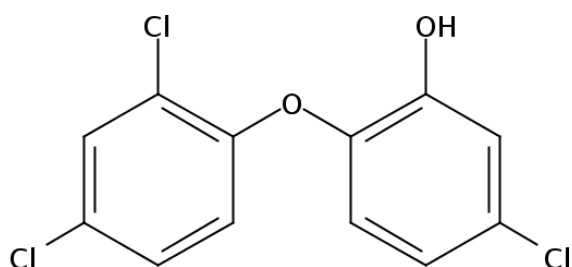


Figure 5 Chemical structure of triclosan [Source: SciFinder]

Triclosan is nowadays under comprehensive review of U.S. Food and Drug Administration (FDA) and U.S. Environmental Protection Agency (EPA) due to conflicting findings [52],[53],[54]. Products containing triclosan under regulation of EPA are rated as highly toxic, marked as a possible carcinogen (LD₅₀ > 5000 mg/kg for rat, oral route; LD₅₀ > 9300 mg/kg for rabbit, dermal route, and LD₅₀ > 0.15 mg/L for rat, inhalation route [55]. The possible health effects are said to be for example: thyroid and estrogen-related modulation and regulation (endocrine effects), immune system failures, dermal irritation, triclosan in urine and other tissues (body and environment contamination), chronic, developmental and reproductive toxicity, change in enoyl acyl carrier reductase, hinder muscle movement, and reduced sperm production in male rats. Another concern connected with triclosan usage is possible development of antibiotic-resistant germs.

4.2 Testing microorganisms

Escherichia coli

E. coli is widely distributed Gram-negative facultative anaerobic, rod-shaped enteric bacterium. The majority of strains are avirulent, but some pathogenic serovars (e.g. *E. coli* O157:H7 or non-O157:H7 serovars O26, O45, O103, O121, O145) produce Shiga toxin which is responsible for outbreaks associated with vegetables production and ground beef. [56] *E. coli* is commonly found in warm-blooded organisms (mainly in lower intestine) producing vitamin K₂ and preventing colonization of the intestine by pathogenic bacteria. Non-pathogenic strains (Nissle 1917, O83:K24:H31 – Colinfant) are utilized as probiotics for gastroenterological disease treatment, including inflammatory bowel disease. [57],[58],[59]

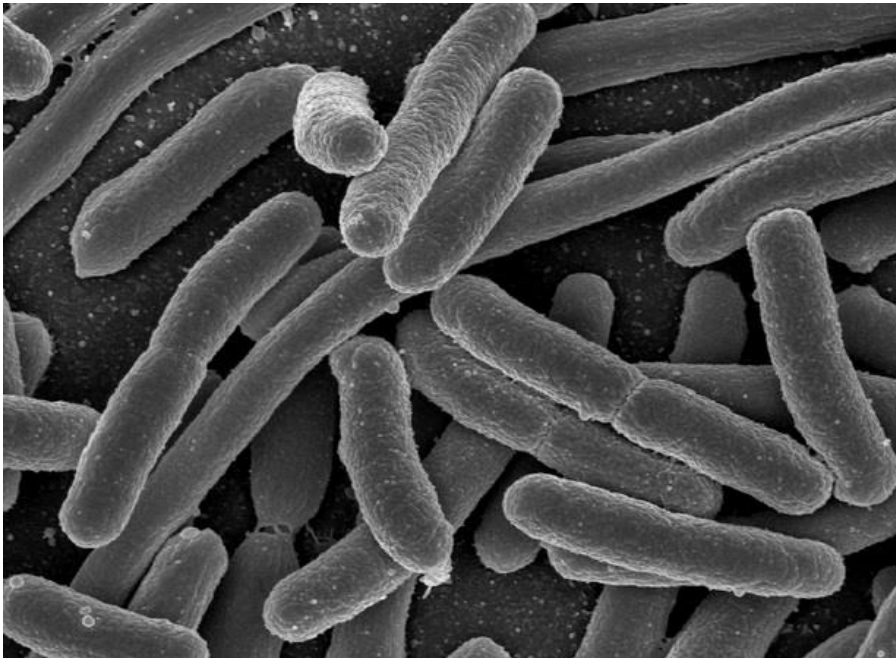


Figure 6 *E. coli* [Source: <http://fermentationanalysis.co.uk/>]

Virulent strains of *E. coli* are connected to following health problems: gastroenteritis, urinary tract infections, neonatal meningitis, haemolytic-uremic syndrome, peritonitis, mastitis, septicaemia and Gram-negative pneumonia, strokes, oedema, increased fluid build-up, increased blood-pressure. [60]

Staphylococcus aureus

S. aureus is known pathogen for more than 130 years (in clinical settings), and increased the amount of research with antibiotic-resistant strains (e.g. methicillin-resistant). *S. aureus* is a Gram-positive facultative anaerobic cocci bacterium, which is positive for catalase and nitrate reduction. It is a common cause of skin infections, respiratory diseases and food poisoning. The infection is promoted by protein toxins production by disease-associated strains. The biggest issue nowadays is an emerging amount of antibiotic-resistant strains (e.g. MRSA). [61]

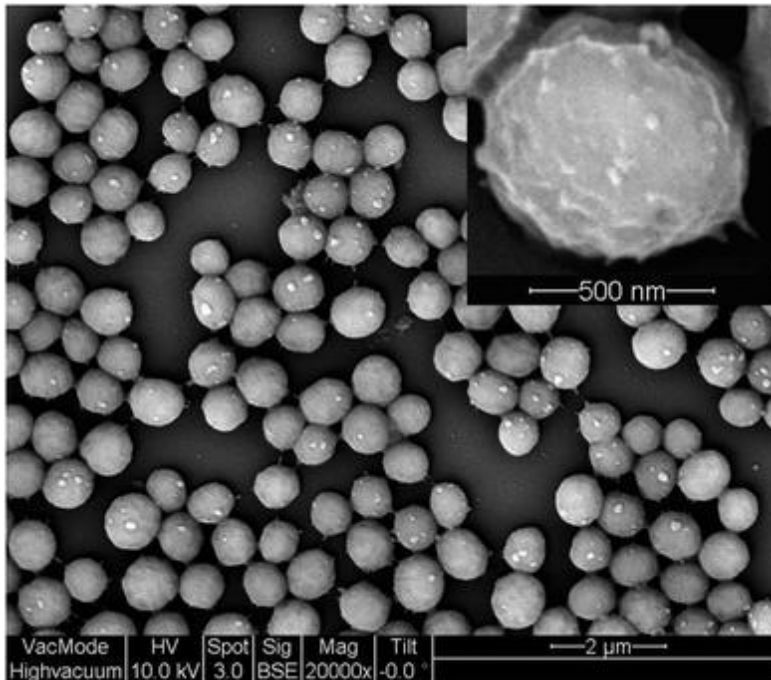


Figure 7 S. aureus [62]

Nearly all strains of *S. aureus* secrete enzymes and cytotoxins including haemolysins (alpha, beta, gamma, and delta), nucleases, proteases, lipases, hyaluronidase and collagenase, which help bacteria to growth on converted host tissues. Some strains produce additional exoproteins with influence on immune system cells (e.g. toxic shock syndrome toxin-1, staphylococcal enterotoxins, exfoliative toxins and leucocidin). [63] Most of the toxins produced by *S. aureus* are highly heat-stable. *S. aureus* is a frequent commensal of all humans (many persons are non-symptomatic carriers) and it is commonly found in environmental samples [56]. If a proper precautions to reduce the risk of contamination are taken, its critical levels can be lowered to harmless ones. The promotion of hazard analysis and critical control points today lessens the opportunities for growth to numbers sufficient to produce the heat-resistant enterotoxins [64].

4.3 Methods

4.3.1 Plasma treatment

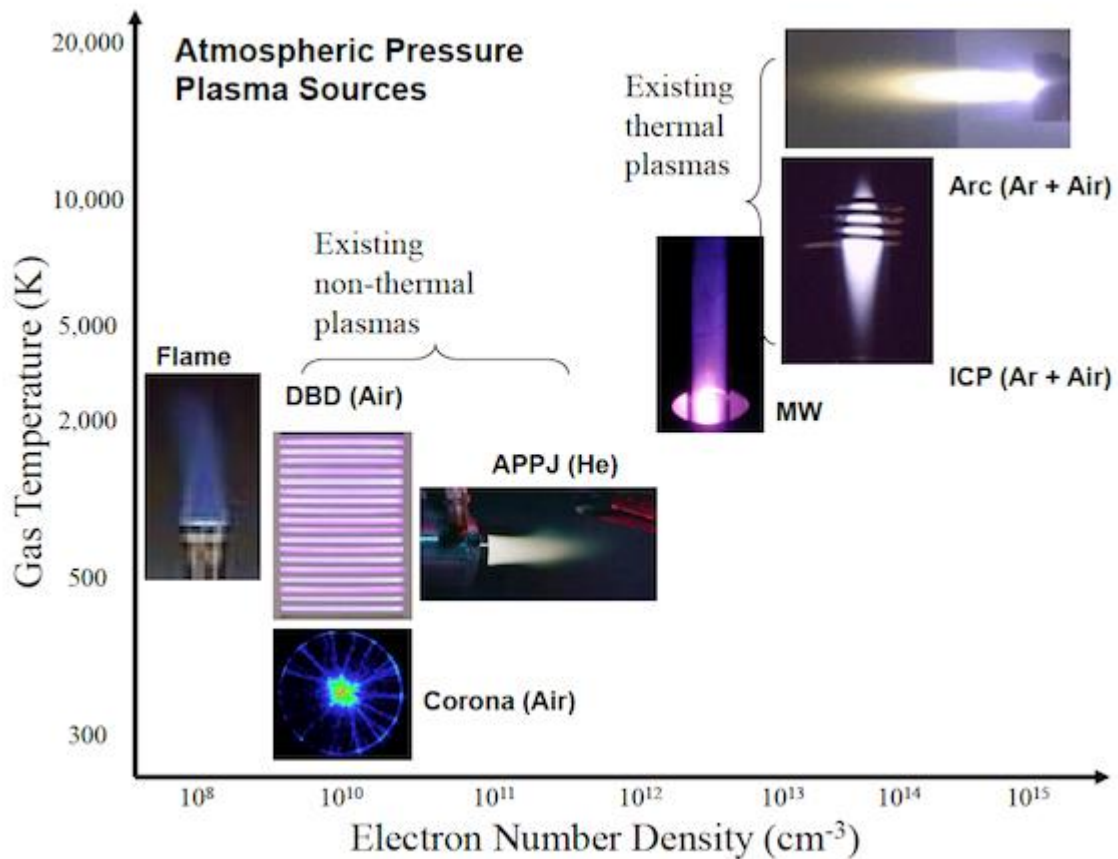


Figure 8 Low-temperature atmospheric pressure plasma sources [65]

Plasmas are the most common forms of matter, comprising more than 99 % of the visible universe (e.g. lightning, nebulae-luminous clouds, solar wind, auroras, interstellar space, galaxies). Plasma is a high energetic form of partially-ionized ionized gas (ions, neutrals and charged particles), the fourth state of matter. The term plasma was first introduced by Irving Langmuir (1928) as it reminded him of blood plasma named by Jan Evangelista Purkyně. Plasma serves to describe the area (not influenced by its boundaries) containing balanced charges of ions and electrons (that means electrically neutral). Plasma is defined as a quasineutral gas, while from microscopic viewpoint, free electrons and ions cause all characteristic effects by their electromagnetic interactions (e.g. various electron and ion temperatures in one plasma, drifting particles in magnetic field, waves in plasma, nonlinear phenomenon). Natural and man-made plasmas occur over a wide range of pressures, electron temperatures, and electron densities. Most plasmas of practical significance have temperatures about 1 – 20 eV, with electron densities from 10^6 to 10^{18} cm^{-3} (in conventional system is in the range 10^{-7} – 10^{-4} cm^{-3}). Not all particles need to be ionized in plasma (in plasma chemistry it is only partially

ionized). When the ionization degree is near to unity, the plasma is called completely ionized plasma (traditional in tokamaks, stellarators, plasma pinchers, etc.). When the ionization degree is low, the plasma is called weakly ionized plasma (the main interest of plasma chemistry). The term sheath stands for transition zone between the plasma and its boundaries. [66],[67],[68]

The temperature of plasma is affected by mean plasma particle energy and degree of freedom. Therefore, multicomponent systems are able to embody several temperatures. In laboratory generators, the electric field energy is first accumulated by electrons amongst collisions and then transported from electrons to heavy particles. Electrons gain energy from the electric field during mean free path and with consequent collisions with heavy particles lose only small portion of energy (higher temperatures of electrons than heavy particles). Further collision may these temperatures equilibrate. Besides the astrophysical plasmas, one can distinguish two main groups of artificial plasmas, i.e. low temperature plasmas ($\leq 50\,000$ K) and so-called high-temperature (or fusion) plasmas ($50\,000 - 10^6$ K). In general, another division can be made – plasmas in the thermal equilibrium (temperature of active species is the same) and plasmas that are not in thermal equilibrium (electrons have much higher temperatures in contrast to heavy ions). [68],[69]

Plasma offers following major features [66]:

- Temperatures or at least some plasma components and energy density can significantly exceed conventional technologies
- Plasmas can produce very high concentrations of energetic and chemically active species
- Plasma systems can essentially be far from thermodynamic equilibrium, providing extremely high concentrations of the chemically active species and keeping bulk temperature as low as room temperatures

Temperature in plasma is determined by an average energies of plasma particles and their relevant degrees of freedom and can exhibit manifold temperatures. In laboratory plasma generators, the energy from electric field is first accumulated by electrons (during mean free path) between collisions and is transferred to heavy particles, while electrons lose only a small portion of that energy. Subsequently, collisions of electrons and heavy particles (Joule heating) can equilibrate their temperature or an intensive cooling mechanism precluding heating of the entire gas is present. A basic requirement for local thermodynamic equilibrium (LTE) in plasma is a temperature difference between electrons and heavy neutral

particles which is, due to Joule heating in the collisional weakly ionized plasma, conventionally proportional to the square of ratio of electric field (E) to the pressure (p); only in an event of small E/p values do the temperatures approach each other. Furthermore, the LTE conditions require chemical equilibrium and restrictions of gradients. Ionization and chemical processes in these plasmas are determined by temperature (indirectly by electric fields through Joule heating). Such quasi-equilibrium plasma is usually called thermal plasma. Variety of plasmas exist very far from the thermodynamic equilibrium and are characterized by multiple different temperatures (related to particles and different degrees of freedom). It is the electron temperature often exceeding significantly temperature of heavy particles ($T_e \gg T_0$). Ionization and chemical processes in such non-equilibrium plasmas are not so sensitive to thermal processes and temperature of gas. The non-equilibrium plasma of this type is than called non-thermal plasma. Relationships between different plasma temperatures in non-thermal plasmas can be presented in the collisional weakly ionized plasmas as $T_e > T_v > T_r \approx T_i \approx T_0$ (where T_e – electron temperature, T_v – temperature of vibrational excitation of molecules, T_0 – heavy neutrals translational degree of freedom/gas temperature, T_i – ions temperature, T_r – temperature of rotational degrees of freedom of molecules). In many non-thermal systems, the electron temperature is about 1 eV and the gas temperature is close to room temperature as they are usually generated at low pressure/low power levels/different kinds of pulsed discharge systems. [66]

Table 2 Plasma divided according to temperature (legend: T_i – ion temperature, T_e – electron temperature, T_g – plasma gas temperature, n_e – electron density) [67]

Plasma	State	Examples
<i>High-temperature (equilibrium/isothermal)</i>	$T_i \approx T_e \approx T_g > 10^6\text{K}$ $n_e > 10^{20} \text{ m}^{-3}$ Fractional ionization up to 100 %	Laser fusion plasma
<i>Low-temperature plasma</i>		
Thermal plasma (quasi-equilibrium)	$T_i \approx T_e \approx T_g < 2 \cdot 10^4\text{K}$ $n_e > 10^{20} \text{ m}^{-3}$ Fractional ionization up to 1 - 10 %	Arc plasma, plasma torch, RF inductively coupled plasma
Cold plasma (non-equilibrium/non-isothermal)	$T_i \approx T_g \approx 300 \text{ K}$ $T_i < T_e \leq 10^5 \text{ K}$ $n_e \approx 10^{10} \text{ m}^{-3}$ Fractional ionization up to 1 - 10 %	Glow, corona, dielectric barrier discharge, plasmatic field beam, hollow cathode discharges

Electron energy distribution function (EEDF) $f(\varepsilon)$ describes rates of electrons transmitting the energy to other plasma components and providing it for ionization, excitation, dissociation and other plasma-chemical processes dependent on number of electrons with enough energy for this job. EEDF is strongly dependent on electric field and gas composition, mainly in non-thermal discharges, and may be very far from the equilibrium distribution. It can be described by the quasi-equilibrium Maxwell-Boltzmann distribution function: [66],[70]

$$f(\varepsilon) = 2 \sqrt{\varepsilon/\pi(kT_e)^3} \exp\left(-\frac{\varepsilon}{kT_e}\right) \quad (1)$$

where k is a Boltzmann constant (when the temperature is in energy units, than $k = 1$ and can be omitted). The mean electron energy (1st distribution function moment) is proportional to temperature in the conventional way: [66],[70]

$$\langle \varepsilon \rangle = \int_0^{\infty} \varepsilon f(\varepsilon) d\varepsilon = \frac{3}{2} T_e \quad (2)$$

Positive ions are formed in the ionization process by electrons loss in atoms and molecules. In relatively cold plasmas used in technological processes the charge is usually equal to 1 e. Electron attachment leads to formation of negative charge -1 e. [66],[70]

Elementary processes can be divided into two general classes – elastic and non-elastic class. Elastic collisions represent internal energies in which colliding particles do not change, so the kinetic energy is conserved and results in geometric scattering and kinetic energy redistribution. Inelastic collisions covers all other collisions (e.g. ionization) resulting in energy transfer from kinetic energy of colliding partners into internal energy (which can be sometimes transferred back to plasma electron kinetic energy). These processes are often named superelastic collisions. The six major collision parameters are: cross section (essential characteristic interpreted as an imaginary circle of are σ moving together with one of the collision partners; if the centre of other partner crosses the circle, the reaction takes place), probability, mean free path, interaction frequency, reaction rate, reaction rate coefficient. The dimensionless probability of the elementary process is the rate of the inelastic collision cross section to the corresponding cross section of elastic collision in the same conditions. The mean free path λ of collision partner A with respect to the elementary process $A + B$ with another collision partner (B) can be calculated as: [66],[70]

$$\lambda = 1/n_B\sigma \quad (3)$$

where n_B is the particle B concentration. The interaction frequency ν of one collision partner A with another collision partner B is defined as [66],[70]:

$$\nu_A = n_B\sigma v \quad (4)$$

where v is a relative velocity. The velocity distribution function $f(v)$ and dependence of cross section σ on the collision partners' velocity should be averaged to [66],[70]:

$$\nu_A = n_B \int \sigma(v)vf(v)dv = \langle\sigma v\rangle n_B \quad (5)$$

Number of elementary processes w , which take place per unit volume per unit time is called reaction rate, that can be for bimolecular processes $A + B$ calculated as follows [66],[70]:

$$w_{A+B} = \nu_A n_A = \langle\sigma v\rangle n_A n_B \quad (6)$$

where $\langle\sigma v\rangle$ is reaction rate coefficient that can be also calculated for bimolecular reaction [66],[70]:

$$k_{A+B} = \int \sigma(v)vf(v)dv = \langle\sigma v\rangle \quad (7)$$

Ionization can be subdivided into following five categories [66]:

1. Direct ionization by electron impact – ionization of neutral and previously unexcited atoms, particles or molecules by electron. Most important in cold or non-thermal discharges.
2. Stepwise ionization by electron impact – ionization of preliminary excited neutral species. Mostly important in thermal or energy-intense discharges.
3. Ionization by collision of heavy particles – during ion-molecule or ion-atom collisions, collisions of electronically or vibrationally excited species, when total energy of partners exceeds ionization potential. Chemical energy of colliding neutral species can also contribute to ionization in the associative ionization processes.
4. Photo-ionization – collisions of neutrals with photons resulting in formation of an electron-ion pair. Mostly important in thermal plasmas and some mechanisms of non-thermal discharges.
5. Surface ionization (electron emission) – provided by electron, ion and photon collisions with different surface or by surface heating.

Electron-electron, electron-ion, and ion-ion scattering processes are the so-called Coulomb collisions that are less frequent in discharges with low degrees of ionization, and a strong dependence of their cross sections on the kinetic energy of colliding particles occurs. A scattering takes place if the Coulomb interaction energy ($U \sim q^2/b$, where b is the impact parameter) is about kinetic energy ε of a moving particle. The impact parameter ($b \sim q^2/\varepsilon$) and the reaction of cross section σ can be estimated as πb^2 : [66]

$$\sigma(\varepsilon) \approx \pi \frac{q^4}{(4\pi\varepsilon_0\varepsilon)^2} \quad (8)$$

Electron-electron scattering cross sections at room temperature are about 1000 times greater than at an electron temperature 1 eV typical for discharges. Energy transfer during elastic collisions is possible only as a transfer of kinetic energy: [66]

$$\gamma = \frac{2mM}{(m+M)^2} \quad (9)$$

where γ stands for average fraction of kinetic energy transferred from one particle of mass m to another particle of mass M ; an elastic collision of electrons with ions or heavy neutrals ($m \ll M$, $\gamma = 2m/M$; $\gamma \sim 10^{-4}$) explains the predomination of direct electron impact ionization. Only electron-electron collisions allow significant energy transfer.

Direct ionization is a result of the interactions of an incident electron having a high energy ε with a valence electron of a preliminary neutral atom or molecule. Ionization occurs when the energy $\Delta\varepsilon$ transferred to the valence electron exceeds the ionization potential I , with clear physical understanding described by the classical Thomson model and multiplied Thomson formula with a kinetic energy ε_v of the valence electron: [66]

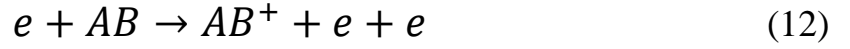
$$\sigma_i = \frac{1}{(4\pi\varepsilon_0)^2} \frac{\pi e^4}{\varepsilon} \left(\frac{1}{\varepsilon} - \frac{1}{I} + \frac{2\varepsilon_v}{3} \left(\frac{1}{I^2} - \frac{1}{\varepsilon^2} \right) \right) \quad (10)$$

All the modification of the Thomson formula can be combined, as well as utilization of formulas for direct ionization cross section estimation by ionization rate coefficient $k_i(T_e)$ assuming the Maxwellian EEDF can be utilized: [66]

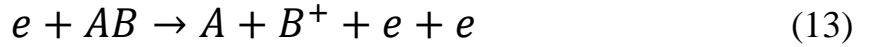
$$k_i(T_e) = \sqrt{\frac{8T_e}{\pi m}} \sigma_0 \exp\left(-\frac{1}{T_e}\right) \quad (11)$$

where the cross section $\sigma_0 = Z_v \pi e^4 / I^2 (4\pi\epsilon_0)^2$ is about geometric atomic cross section (for molecular nitrogen, 10^{-16} cm^2 , and for argon $3 \times 10^{-16} \text{ cm}^2$), where Z_v is the number of valence electrons in an atom.

Non-dissociative ionization of molecules by direct electron impact, which takes place when the electron energy does not greatly exceed the ionization potential, can be presented for the event of diatomic molecules AB as: [66]



The fastest internal motion of atoms inside molecules is molecular vibration, with typical periods of $10^{-14} - 10^{-13} \text{ s}$ that are longer than interaction times between plasma electrons and molecules ($a_0/v_e \sim 10^{-16} - 10^{-15} \text{ s}$, where a_0 is atomic unit of length). The result of this quote is that all atoms inside a molecule may be considered as frozen during the process of electron transmission simulated by electron impact and which is also known as Frank-Condon principle. The non-dissociative ionization of molecules usually results in formation of the vibrationally excited ion $(AB^+)^*$ and requires more energy than corresponding atomic ionization. When the electron is relatively high substantially exceeds the ionization potential, the dissociative ionization process can take place: [66],[70]

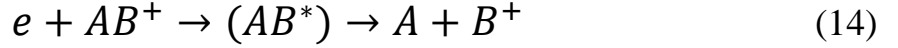


This corresponds to electronic excitation into a repulsive state of the ion $(AB^+)^*$, followed by a decay of this molecular ion. The dissociative ionization is essentially greater than that for the non-dissociative one. [66]

Apparently the key actors in plasma-chemical processes are positive ions, whose exothermic reactions with neutrals have usually no activation energy and hence is their role significant (especially in plasma catalysis or reactive ion etching). Electron-ion recombination is highly exothermic process and that is why the process should have a specific channel of accumulation of the energy released during the neutralisation of the positive ion and electron. The majority of these channels of recombination energy consumption are related either to dissociation of molecules or to three-body collisions or to radiation determining three major groups of mechanisms of electron-ion recombination, where cross section of process is relatively low and can compete with the tree-body recombination only when the plasma density is not high: [66]

1. Dissociative electron-ion recombination (fastest neutralisation in molecular gases or ions) – dissociation products are excited. These mechanism is also

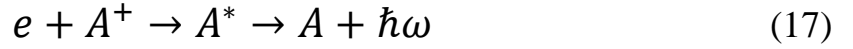
important for atomic gases because of the formation of molecular ions in the ion conversion processes.



2. Electron-ion neutralisation is due to a three-body electron-ion recombination in atomic gases in the absence of molecular ions. Excess of energy goes to kinetic energy of a free electron participating as a third-body partner in recombination act (unlike heavy particles).



3. Conversion into radiation – radiative electron-ion recombination process.



The tremendously high chemical activity of plasmas is based on a high and frequently super-equilibrium concentration of active species, including chemically aggressive atoms and radicals, charged particles and excited atoms and molecules. Vibrational excitation is probably the most important elementary process in non-thermal molecular plasmas responsible for the major part of energy exchange between electrons and molecules making a significant contribution in kinetics of non-equilibrium chemical processes in plasmas. Elastic collisions of electrons and molecules are not effective in vibrational excitation because of their masses ($m/M \ll 1$) significant difference and the typical energy transfer from the electron with kinetic energy ε to the molecule in the elastic collision is about $\varepsilon(m/M)$, while the vibrational quantum can be estimated much higher energy due to $\hbar\omega \approx I\sqrt{m/M}$ (describing low classical cross section of the vibrational excitation in the elastic electron-molecular collision). The cross section of the resonant vibrational excitation process may be found in the quasi-steady-state approximation using the Breit-Wigner formula that illustrates the resonance structure of the cross-section dependence on electron energy: [66]

$$\sigma_{12}(v_i, \varepsilon) = \frac{\pi\hbar^2}{2m\varepsilon} \frac{g_{AB^-}}{g_{AB}g_e} \frac{\Gamma_{1i}\Gamma_{i2}}{\frac{1}{\hbar^2}(\varepsilon - \Delta E_{1i})^2 + \Gamma_i^2} \quad (18)$$

where ε is the electron energy, v_i is the vibrational quantum number of the non-stable negative ion, ΔE_{1i} is the energy of transition to the intermediate state $AB(v_i) \rightarrow AB^-(v_i)$, g_{AB^-} , g_{AB} and g_e are statistical weights, Γ_i is the probability of $AB^-(v_i)$ decay through channels, $\hbar\Gamma_i$ is the energy width of the resonance pikes related to the lifetime of the non-stable intermediate negative ion $AB^-(v_i)$.

The energy dependence of the vibrational excitation cross section depends on the lifetime of the intermediate ionic states (resonances); the short-life resonance (H_2 , N_2O , H_2O , etc.) has the lifetime of the auto-ionization states $AB(v_i)$ much shorter than the period of oscillation ($\tau \ll 10^{-14}$ s) with the very large energy width (Uncertainty principle) resulting in maximum pikes and no fine energy structures for $\sigma_{12}(\varepsilon)$. The displacement of the nuclei is small, so that the low vibrational levels of excitation occurs. The boomerang resonance has an intermediate ion lifetime about molecular oscillation period ($\tau \sim 10^{-14}$ s; i.e. N_2 , CO_2 , CO) and the model gives the formation and decay of the negative ion during one oscillation as interference of incoming and reflected waves resulting in oscillating dependence of the excitation cross section on electron energy (typical peaks 0.3 eV) needing higher energy levels. The maximum of the vibrational excitation cross section decreases with vibrational quantum number. The long-lifetime resonances (i.e. O_2 , NO , C_6H_6) correspond to auto-ionization states $AB^-(v_i)$ with much longer lifetime ($\tau = 10^{-14} - 10^{-10}$ s). The electron energies most effective in vibrational excitation are 1 – 3 eV usually corresponding to maximum electron energy distribution function. Vibrational excitation by electron impact is preferably one-quantum process. [66]

If electron energy exceed ~ 1 eV, rotational excitation can proceed resonantly via the auto-ionization state similarly to the case of vibrational excitation (however the contribution is small). The cross-section of the non-resonant rotational excitation are able to overreach the non-resonant value by about 100 times. Homonuclear molecules (N_2 , H_2) have no dipole moment and the rotational excitation is because of the electron interaction with their quadruple moment. The cross-section of the rotational excitation by a low-energy electron is lower. For evaluation of quasi-elastic energy transfer (electron gas \rightarrow neutral molecules) the rotational excitation may be combined with elastic collisions characterized by the gas-kinetic rate coefficient $k_{e0} \approx \sigma_0 \langle v_e \rangle \approx 3 \cdot 10^{-8}$ cm³/s (where $\langle v_e \rangle$ is averaged thermal velocity of electrons), with an energy loss about $\varepsilon(m/M)$ for each collision.

Electronic excitation by electron impact requires higher electron energies, $\varepsilon > 10$ eV. The Born approximation ca be applied to calculate the cross section of these processes when the electron energies are high enough ($\varepsilon \gg \Delta E_{ik}$): [66]

$$\sigma_{ik}(\varepsilon) = 4\pi a_0^2 f_{ik} \left(\frac{R_y}{\Delta E_{ik}} \right)^2 \frac{\Delta E_{ik}}{\varepsilon} \ln \frac{\varepsilon}{\Delta E_{ik}} \quad (19)$$

where i is the transition from an atomic state to another state k , R_y is the Rydberg constant, a_0 is the Bohr radius, f_{ik} is force of oscillator for transition $i \rightarrow k$ and ΔE_{ik} is the energy of the transition. $\sigma_{ik}(\varepsilon)$ dependence is different for excitation in electronic terms, from which optical radiation is forbidden and the maximum cross section ($\sigma_0 \sim 10^{-16} \text{ cm}^2$) are possible to be reached at lower electron densities ($\frac{\varepsilon}{\Delta E_{ik}} \approx 1.2 - 1.6$ leading to the effect of predominant excitation of the optically forbidden and metastable states by electron impact in non-thermal discharges. [66]

Electron impact is also able to stimulate dissociation of molecules by both vibrational and electronic excitation. Vibrational excitation usually ends in the initial formation of molecules with single or few quanta. Dissociation is then a non-direct multistep process with energy exchange between molecules to gather vibrational energy sufficient for dissociation (this process is effective for a limited gases as N_2 , CO_2 , H_2 , CO . On the other hand, dissociation over electronic excitation can progress in just one collision (i.e. stimulated by direct electron impact). The elementary process can proceed through different intermediate steps of intramolecular transitions: [66]

- Mechanism A – direct electronic excitation from the ground state to a repulsive one with resultant dissociation; required electron energy significantly exceeds dissociation energy; generates high-energy neutral fragments (e.g. affecting surface chemistry in low-pressure non-thermal discharges).
- Mechanism B – direct electronic excitation of a molecule from the ground state to an attractive state with energy exceeding the dissociation threshold; excitation results in dissociation, energies of dissociation fragment are lower this time.
- Mechanism C – direct electronic excitation from the ground state to an attractive state accordant with electronically excited dissociation products; may lead to radiative transition to the low-energy repulsive state with subsequent dissociation; generates high-energy neutral fragments.
- Mechanism D (also called predissociation) – direct electronic excitation from the ground state to the attractive state corresponding to electronically excited dissociation products; excitation leads to radiationless transfer to the highly excited repulsive state with subsequent dissociation into electronically excited fragments.

- Mechanism E – direct electronic excitation from the ground state to the repulsive state with the ensuing dissociation into electronically excited fragments requiring highest electron energies values.

Electron gas energy received from the electric field in non-thermal plasma is distributed between elastic energy losses and different channels of excitation and ionization. All the energy distributions are very similar in general features. At the temperature of electron at 1 eV (common for non-thermal discharges) most of the electron energy can be localized within vibrational excitation of molecules, while the rotational excitation of molecules and elastic energy losses are essential at low electron energies (as it is a non-resonant process). [66]

Electron energy distribution functions (EEDFs) in non-thermal discharges can be very sophisticated and different from quasi-equilibrium statistical Boltzmann distribution and more relevant for thermal plasma conditions. EEDFs are mostly strongly exponential and significantly influence plasma-chemical reaction rates:

- Fokker-Planck kinetic equation – EEDF distribution evolution considered as electron diffusion and drift in the space of electron energy.
- Druyvesteyn distribution – utilized when the electron mean free path is constant; distribution decreases faster than Maxwellian one for the same mean energy.
- Maxwellian distribution – used when elastic collisions dominate electron energy losses and electron-neutral collision frequency is approximated by constant frequency of collisions between electrons and neutrals.
- Margenau distribution – generalized Druyvesteyn distribution for the use with alternating electric fields.
- Distributions controlled by vibrational excitation – if electron energy losses dominate elastic collisions the vibrational excitation of molecules by electron impact strongly influence EEDF in molecular gases as the vibrational excitation uses more electron energy than elastic collisions (e.g. strong increase of EEDF and ionization and electronic excitation rates with vibrational temperature). [66]

EEDF in non-equilibrium discharges in noble gases are usually close to Druyvesteyn distribution if the degree of ionization is not high enough for a significant contribution of electron-electron collisions, while $f(\varepsilon)$ for molecular gases is closer to Maxwellian function. Also a small mixture of molecular gas (c. 1 %) into a noble gas changes EEDF substantially, strongly decreasing the fraction of high-energy electrons; this inevitable effect of admixture is called the

Ramsauer effect. Electron-electron collisions can affect EEDF and make it Maxwellian if the ionization degree is high. [66]

Plasma treatment

Radiofrequency (RF) plasma is strongly non-equilibrium and cold at low pressure. The electron-neutral collision is less regular when the gas is cooled intensively by walls (i.e. $T_e \gg T_0$ as in glow discharges). The upper frequency limit of discharges is due to wavelengths close to system sizes, the lower frequency limit is due to frequencies of ionization and ion transfer. As the ion density is considered to be constant during a period of electromagnetic field oscillation, the RF usually exceed 1 MHz (usually used value is 13.56 MHz). Discharges moderated at low pressure (1 – 100 Torr) have the electron energy relaxation length smaller than characteristic system sizes and the EEDF is determined by a local electric field. When $p \text{ (Torr)} \cdot L \text{ (cm)} < 1$ for inert gases, the electron energy relaxation length is comparable to discharge sizes and EEDF is determined by the electric field distribution in the entire discharge. [66]

Non-thermal RF discharges can be divided into two groups: capacitively (CCP) or inductively coupled discharge. The CCP discharges provide an electromagnetic field by electrodes situated inside or outside a chamber primarily stimulating a (higher) electric field and facilitating ignition. RF power supplies requires typically an active load 50 – 75 Ω . The CCP coupling circuit includes inductance in series with the generator and discharge system because of the formation of the AC resonance in series with the generator and the discharge system within its idle operation to start the discharge. [66]

The external circuit in CCP discharges brings fixed voltage or fixed current. The fixed current regime may be characterised by current density $j = -j_0 \sin(\omega t)$ between two parallel electrodes. It is assumed that the RF plasma density ($n_e = n_i$) is high and the electron conductivity current exceeds the displacement current. Hereby, the ion conductivity current can be marginalized with respect to the displacement current and the ion drift motion during an oscillation period of electric field can be vanished. Electrons are in the sheath of width near the electrode only for a plasma phase oscillation period (space charge phase = no electrons in the sheath). The oscillation space charge generates an electric field forming displacement current and closing the circuit. The quasi-neutral plasma zone is called the positive column. The space charge oscillating electric field with

constant components (providing faster ion drift to electrodes than in the event of ambipolar diffusion) are aimed from plasma to electrodes resulting in ion density in the space charge layers near electrodes lower than that in the plasma. [66]

Moderate pressure CCP discharges assume energy relaxation lengths smaller than sizes of plasma zone and sheaths corresponding to the pressure interval 1 – 100 Torr, where electrons lose and gain their energy in a matter of time interval shorter than the period of electromagnetic RF oscillation. EEDFs, ionization and instantaneous values of the electric field resulting in an essential contribution of ionization sheaths with electric field on maximum values providing maximum electron energies. Moderate pressure RF CCP discharges are sustained in two forms: α -discharge (low luminosity in a plasma volume, brighter layers located closer to electrodes, dark layers immediately adjacent to electrodes) and γ -discharge (much higher current density, relatively thin bright discharge layers immediately adjacent to electrodes, plasma zone luminous separated from bright electrode layers by dark layers, ionization occurs). Both forms operate at normal current density, the current increase is provided by a growth of the electrode area occupied by discharge with constant current density; normal current density is proportional to the frequency of electromagnetic oscillations and in the case of γ -discharge exceeds current density of α -discharge more than 10 times. Current < 1 A belongs to the α -discharge, while higher currents are common for γ -discharge. The α -discharge is abnormal after breakdown where the current density is so small that discharge occupy the entire electrode immediately after breakdown leading to the voltage growth with current (abnormal regime). The transition from α to γ -regime occurs when the current density exceeds critical value depending on pressure, frequency, electrode material and gas type, accompanied by discharge contraction with more than 10-fold increase of current density. Increase of current does not change voltage in γ -discharge, with discharge continuing in normal regime. [66]

Widely used type of RF discharge is low-pressure CCP (≤ 0.1 Torr). The plasma zone is bright and separated from electrodes by dark pre-electrode sheaths. Discharge is generally asymmetric – the sheath, c. 1 cm thick, is placed by the electrode where the RF voltage is used, whereas other is about 0.3 cm. The plasma fills out the entire gap, while the normal current density is not present. The electron energy relaxation length exceeds characteristic sizes of the plasma zone and sheaths. The EEDF is not local and is determined by electric fields (composed of constant – balance of electron and ion fluxes and quasi-neutrality providing current and heating of plasma electrons – and oscillating components) in the zone

of about electron energy relaxation length, and the time of EEDF formation is longer than the period of RF oscillation and permits it to be stationary. The electric field in the space charge sheath exceeds that in the plasma so a sharp change of potential occurs on the boundary of the plasma and the sheath. Plasma electrons move between sharp potential barriers. Electron heating in discharges of not very low pressures is due to electron collisions that can be transferred to chaotic electron motion during the next collision (energy of systematic oscillations). The stochastic heating effect is described as an electron flux to the boundary moving from the electrode exceeding that of the other boundary and so the energy is mostly transferred to the fast electrons. The RF CCP discharges are usually organized in grounded metal chambers where one electrode is connected to the chamber wall (capacitive current in moderate pressure, and higher current densities in low-pressure discharges, where the lower current density is in the sheath) and grounded, and the second one is powered (creating asymmetric discharge). The auto-displacement voltage (constant potential difference) occurs between electrodes if covered by a dielectric layer or if capacitance is installed in the electric circuit to keep similar current between electrodes. [66]

4.3.2 Terahertz spectroscopy

Terahertz (THz) technology is nowadays on the verge of commercial applications (e.g. security, biomedicine, broadband, communication, non-destructive testing and process control). The focus is on established THz techniques and instrumentation over the frequency range 0.3 – 10 THz (1 mm – 30 μm) as the THz waves are electromagnetic waves in the frequency range between 100 GHz and 10 THz. Within this region many molecules exhibit characteristic signatures in their absorption spectra. In addition to this, many substances impermeable to visible light or IR are transparent to terahertz waves. These waves are able to excite soft polar phonons in solids, vibrations of larger chains in biomolecules, to induce plasma oscillations of free charge carriers with concentrations of $\sim 10^{14} - 10^{18} \text{ cm}^{-3}$ and to interact with carriers localized in nanoparticles. Due to the lack of bright sources and sensitive detectors the THz spectroscopic applications about 20 years ago concerned mainly the astronomy and analytical science. Advances in laser and semiconductor technologies during the past years made it possible to develop suitable sources and detectors for terahertz radiation. Recent developments in THz spectroscopy are likely to become standard techniques in the future. [71],[72],[73]

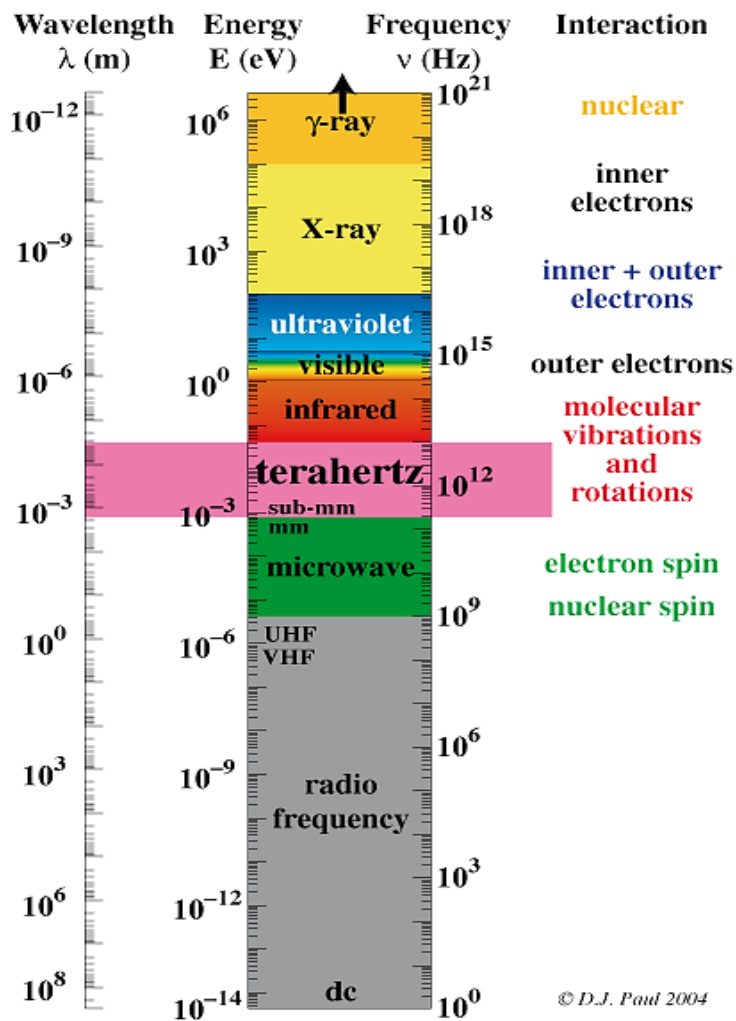


Figure 9 Electromagnetic spectrum [74]

The terahertz (THz) spectral range is one of the least explored part of the electromagnetic spectrum. The term far-infrared (FIR) was used to cover all wavelengths between 20 μm up to shortest millimetre region. Also, the sub-millimeter waves was used, although it provides only the cut-off at 1 mm. The term THz is generally agreed for the spectral range 0.1 – 10 THz (1 mm – 30 μm) no matter whether approached from the IR or mmW direction (therefore some properties are similar to those in visible and IR waves, and others bear a resemblance to propagation in mmW region). Researches in THz region began in early 20th century (before 1892) with a leading personality of Heinrich Rubens, following the remarkable research of the nineteenth century focusing on microwave region with personalities as Lodge, Fleming, Popov, Lebedov, Rayleigh, Bose, Marconi and Righi. Nichols made first significant experiments in FIR region working with crystalline quartz discovering that its reflectivity over a narrow wavelength range near 9 μm rose from a few percent to nearly that of a silvered surface (residual ray effect), which is due to lattice vibrations. Rubens

with his colleagues later extended techniques to wavelengths beyond 50 μm (6 THz). Together with Kurlbaum with the usage of residual ray spectrometer, necessary data were obtained and these results were given to Planck, who created the Planck's radiation law and helped him with inventing his quantum theory. [72],[75]

A major problem in THz research is a very high absorption of the Earth's atmosphere (over most of the frequency range), mainly due to vibrational-rotational levels of water vapour. Above the 2.2 THz, the absorption increases very rapidly and was the biggest restriction of THz research. THz region is fascinating due to the electron energy spread. The value of THz frequencies for a wide range of applications can be understood by the reference to the unit conversions. The room temperature corresponds to c. 6 THz according to the: [72]

$$h\nu = kT \quad (20)$$

Accordingly, kT can be made equal to $h\nu$ in the region from 0.3 – 10 THz (corresponding with 1.2 – 37 meV) with comparative simplicity by varying the temperature in the range of 14 K – 210 °C, which is a unique feature of this part of electromagnetic spectrum. This matches with energy levels of various phonon bands, shallow impurities and rotational interactions in gases. [72]

Gaussian beams describes the best the radiation propagation at THz frequencies. A Gaussian intensity distribution determines the Gaussian beam profile. It is radially symmetric in its simplest form. If the phase over the radius r is uniform, the Gaussian intensity reproduces itself under Fourier transformation and represents the unique property of such beams. The electric field of the Gaussian beams is represented by following equation: [72]

$$E = E_0 \exp\left(-\frac{r^2}{w^2}\right) \quad (21)$$

With the full solution of the Fresnel integral, the Gaussian distribution is present at each point longitudinal the propagation direction in the optical system (the transverse distribution). Focusing or defocusing changes only the size not the Gaussian character. As the electromagnetic field remains self-reproducing after repeated oscillation in the resonator, the laser often oscillate in the Gaussian mode, which multiplication with certain polynomials either leads to the higher order transverse modes (distributions). The Gaussian beam waist radius w is defined to assign the physical dimension to the infinite field distribution, where the intensity drops to 0.135 $((1/e)^2)$ of the intensity at the w from the optical axis.

The Gaussian beam radius and the wavefront curvature radius can change. The curvature is infinite at the position of the beam waist minimum w_0 , where the flat phase front is found corresponds e.g. to the flat outcoupling mirror of the laser in the confocal laser design. The Gaussian beam radius $w(z)$ and the curvature radius $R(z)$ of the wavefront can be described by these two parameters only: [72]

$$z_R = \frac{\pi w_0^2}{\lambda} \quad (22)$$

$$w(z) = w_0 \sqrt{1 + \left(\frac{z}{z_R}\right)^2} \quad (23)$$

$$R(z) = z \left(1 + \left(\frac{z_R}{z}\right)^2\right) \quad (24)$$

The wavefront is flat at the minimum waist radius position ($R(z \rightarrow 0) \rightarrow \infty$). The curvature complex radius q is defined by the w and the curvature radius R [72]:

$$\frac{1}{q(z)} = \frac{1}{R(z)} - i \frac{\lambda}{\pi w^2(z)} \quad (25)$$

The infinite curvature radius R has only the imaginary part equal to Rayleigh range z_R for the q at the position of the minimum waist $w(z = 0) = w_0$. The change of the Gaussian beam intensity may be approximated by a linear relationships as the $w(z)$ grows nearly linearly with z at a distance. From a far distance the Gaussian beam can be sighted as a point source originating from the centre of the minimum waist. The enabling angle θ determines the beam divergence defined in the sphere due to the beam curvature: [72]

$$\tan(\theta) = \frac{\lambda}{\pi w_0} = \frac{w_0}{z_R} \quad (26)$$

The tangent can be approximated by the self angle if the opening (enabling) angle is small. The beam parameter product is often used to describe laser beam profiles, depending only upon the wavelength and it does not change while the beam is passing through linear optical systems. For a real laser, the Gaussian beam with minimal divergence is hard to obtain due to the presence of higher order modes or inhomogeneous gain medium. Higher transverse modes lead simultaneously to the increase of the waist radius and divergences accounted for by the M factor increasing the fundamental Gaussian mode, the transverse electric and magnetic TEM₀₀ model. [72]

$$\theta w_0 = M^2 \frac{\lambda}{\pi} \quad (27)$$

To measure the quality of the beam, the beam propagation factor $k = 1/M^2$ is utilized. Parameter k and M^2 are experimentally determined and are both equal to one for ideal Gaussian beams (k is smaller than one for larger beam divergence and lower beam quality; if M^2 is smaller, it leads to smaller focus spot and divergence after lens). [72]

In geometric optics, the full viewing angle $\theta' = 2\theta$ corresponds to lens diameter used. The angle is calculated from the focal length f and the lens diameter D as: [72]

$$\theta' \approx \frac{D}{f} = \frac{l}{f\#} \quad (28)$$

The F-number ($f\#$) stands for the relative aperture (speed of lens), expressed as f/D . The depth of focus is twice larger than the value of confocal parameter (or Rayleigh range), which is a useful quantity describing the length scale where the Gaussian beam propagation changes from a near-field to a far-field dominated region (i.e. Fresnel \rightarrow Fraunhofer diffraction), and giving the length scale of well collimated beam. Therefore, it can be used as a parameter in many equations related to Gaussian beam propagation. [72]

Light ray propagation in geometric optics can be calculated by the matrix formalism, where the matrices 2×2 elements represent different optical elements. Gaussian beams (originating from an extended source) can be analogically to ray in geometric optics defined by beam parameters, where these Gaussian beams (fundamental ones represent wave propagation properly for limited divergence) are described by paraxial wave equation (simplified Helmholtz wave equation), approximated as:

- the variation of the field amplitude for a distance comparable to the wavelength along the direction of propagation is small,
- the axial variation is small in comparison to the variation perpendicular to this direction. [72]

When focusing is going to result in the beam waist comparable to the wavelength or less corresponding to the angle of $\theta < 18^\circ$ (equation 26), corrections leading to the field amplitude distribution deviating from the Gaussian beam distribution are required beyond the paraxial limit. [72]

Propagation of the beam through the optical element is mathematically equivalent to the linear matrix transformation of its parameters, where the parameter

transformation through elements is calculated by a left-multiplication (the incoming beam is incident from the left by the convention) of each matrix/matrix-multiplication or all individual matrices resulting in a total of 2×2 matrix. The ray transfer matrix of the system simulates single proliferation via whole system. Those parameters (A, B, C, D) form a complex bi-linear transformation:

$$\begin{pmatrix} r_{out} \\ \phi_{out} \end{pmatrix} = \begin{pmatrix} A & B \\ C & D \end{pmatrix} \begin{pmatrix} r_{in} \\ \phi_{in} \end{pmatrix} = \begin{pmatrix} Ar_{in} + B\phi_{in} \\ Cr_{in} + D\phi_{in} \end{pmatrix} \quad (29)$$

where (in geometric optics) r_{in} stand from incoming ray distance to the axis of propagating along z with the ray slope ϕ_{in} . Resulting ray is given by r_{out} and ϕ_{out} . The curvature radius is expressed by the complex radius curvature q for Gaussian beams, where the elements of the matrix (A, B, C, D) are the same as in geometrical optics. The focus is on the propagation waist, so the $q_{in} = iz_R$. One of the most challenging issues in THz experiments is the efficient transport of the electromagnetic wave from the source to the detection system (even with neglecting water vapours) done by coupling of Gaussian beams with components used in the microwave region, which are also utilizable in THz region. The THz spectroscopic system with efficient power coupling between detector and source is not sufficient enough, and furthermore can be lowered by inserted sample. Further optimization is therefore necessary with all its limits. The Gaussian beam propagation analysis is therefore a crucial requirement for proper beam propagation in the THz frequency range as from small optical systems. [72],[76]

All materials absorb radiation in certain degree. The THz window and filters are designed for minimum absorption, while the samples are usually of very high absorption intensity. The Lambert-Beer absorption law is used to characterize losses:

$$I = I_0 \exp(-\alpha d) \quad (30)$$

where (with no reflection losses) I_0 stands for the initial light source intensity, α is the linear absorption coefficient and d material thickness. When the Fourier-transform spectrometers, the absorbance $A = -\log_{10}(I/I_0)$ is measured for a transmitted intensity I and I_0 with a relationship to the absorption coefficient $\alpha = \ln(10)A/d$. The penetration depth $d_p = 1/\alpha$ of a wave into the material may be defined by determining depth at which the intensity is reduced to $1/e$ of the initial value. Generally, the electromagnetic wave is described by the propagation of electric or electromagnetic field. The wave propagation via the $+z$ direction through a medium is described by equation:

$$E = E_0 \exp(i\phi) = E_0 \exp(i(\hat{k}z - \omega t)) \quad (31)$$

where E_0 is the amplitude, and ϕ is the complex phase. [72]

The introduction of high-power lasers and short fs-pulse lasers in 1970s was followed by the THz time-domain spectroscopy (TDS) and other pulse detection techniques, which have a potential to drive materials into nonlinear regimes. Using the system, the refractive index can be determined experimentally by the utilization of the Maxwell relation:

$$\hat{n}^2 = \varepsilon\mu \quad (32)$$

$$Z = \sqrt{\frac{\mu\mu_0}{\varepsilon\varepsilon_0}} \quad (33)$$

where \hat{n} is the complex refractive index, μ is the relative magnetic permeability, Z is the wave's impedance, and ε stands for the relative dielectric permittivity. The refractive index in materials is not constant – it varies as a function of frequency leading to the dispersion phenomena. The absorption corresponds with a complex quantity and an anisotropic material is described by a tensor. When n has a negative value (simultaneously ε and μ are negative), the material is called metamaterial (artificially structured quasi-bulk materials with properties unattainable in unstructured bulk homogenous material, posing as “invisible cloak” for THz beams). [72]

The complex dielectric constant of the medium ε is expressed by the complex refractive index and separated into real ($\varepsilon' = n^2 - \kappa^2$) and imaginary ($\varepsilon'' = 2n\kappa$) parts describing material properties (e.g. polarizability): [72]

$$\varepsilon = \hat{n}^2 = (n + i\kappa)^2 = \varepsilon' + i\varepsilon'' \quad (34)$$

From the resonant Lorentz dielectric permittivity with adjustment and simplification with introduction of total number of electrons and definition of plasma frequency, the equations lead to the simple, but of fundamental importance, expression of dielectric permittivity

$$\varepsilon = 1 + \frac{\omega_p^2}{\omega_0^2 - \omega^2 - i\gamma\omega} \quad (35)$$

where ω_p stands for plasma frequency, ω_0 is oscillator resonance frequency, i is for oscillator, γ is damping constant. For high frequency beyond the resonance, the equation is: [72]

$$\varepsilon = 1 - \frac{\omega_p^2}{\omega^2} \quad (36)$$

which implies that if the frequency $\omega \ll \omega_p$ cannot penetrate and are reflected from the plasma, metal or semiconductor (heavily doped).

THz opto-parametric oscillators are efficient THz sources relying on nonlinear processes and together with THz TDS are a room temperature devices with added advantage related to the initial high intensity of visible lasers allowing more likely low conversion factors to generate THz photons. In the nonlinear process even three or four photons can be involved inducing three-wave and four-wave mixing processes. Optical rectification utilizes a nonlinear material to generate THz radiation. The process down-converts a visible photon into two photons in the IR and THz region. The second order rectification and generation of THz radiation is strongly depending on the material anisotropy. [72]

Polarization is an important feature to study materials. Nowadays, development is focused on suitable components for polarization's manipulation to get alike facilities as those available in the visible region (e.g. devices based on photonic bandgaps, metamaterials). Miscellaneous detectors and emitters specify the polarization and form of the response – dipole antennas for selecting preferably linear polarization, and systems in magnetic fields are capable of responding, emitting or transmitting circularly to elliptically to the suitable polarized light. [72],[76]

Ultrashort pulses used in THz TDS have a wide frequency spectrum. Elements as mirrors and lenses may not reflect, transmit or focus all frequencies in punctually the same way introducing the pulse broadening in time (pulse shaping). Generally, typically distinguishable effects – amplitude filters if waves are reflected at some frequencies with lesser amplitude or dispersion if the phase at different frequencies is changed – which are amplified in the laser cavity. [71],[72],[73],[76],[77],[78] THz TDS usually uses lasers with typical values of femtosecond lasers for optical materials at 800 nm range from 360 fs²/cm (fused silica) to 580 nm fs²/cm (sapphire). The solid state gain media Ti:Sa based fs lasers (developed 1986) enables variety of new techniques in the selected frequency range. The Turnkey fibre-based fs laser is compact and easily attainable. The mode-locked fs laser produces regularly spaced pulses corresponding to electric field amplitude regularly spaced in frequency (i.e. frequency combs). Lasers using Ti:Sa crystals can generate 10 fs or less pulses. This type of lasers are suitable for room temperature applications with enhanced data acquisition. The NIR fs lasers

with centre wavelengths in the 1500 nm band can use fibres to propagate the pulses of less than 100 fs with average power level of 100 mW with mode-locked repetition rates from 80 to 100 MHz. The lasers using Ti:Sa crystals can generate pulses as mentioned above (average power ≥ 500 mW, repetition rates in GHz). The most commonly used material for femtosecond mode-locked lasers is titanium-doped aluminium oxide (Ti:Sapphire) with spectral bandwidth 650 – 1000 nm, high thermal conductivity allowing high optical pumping. Other laser gain mediums regularly used are Nd:glass (1040 – 1070 nm), Nd-doped fibre (1040 – 1070 nm), Yb-doped fibre (1030-1080 nm) and ER-doped fibre (1520 – 1580 nm). [72],[75],[76]

The THz TDS consist of polarized fs lasers and three supplementary components: [72],[75],[76]

- emitter based on semiconductor switch or nonlinear crystal (LiTaO_3) - down-converting the THz frequency band from the VIS/NIR to THz region (i.e. generation or amplification of the THz wave),
- detector (semiconductor material or nonlinear crystal – usually LiTaO_3 or ZnTe) – detection of emitting and freely propagating THz pulse,
- method of various time delay introduction between second fs pulse utilized for detection and the THz pulse locked in time to the fs pulse and generated by down-conversion.

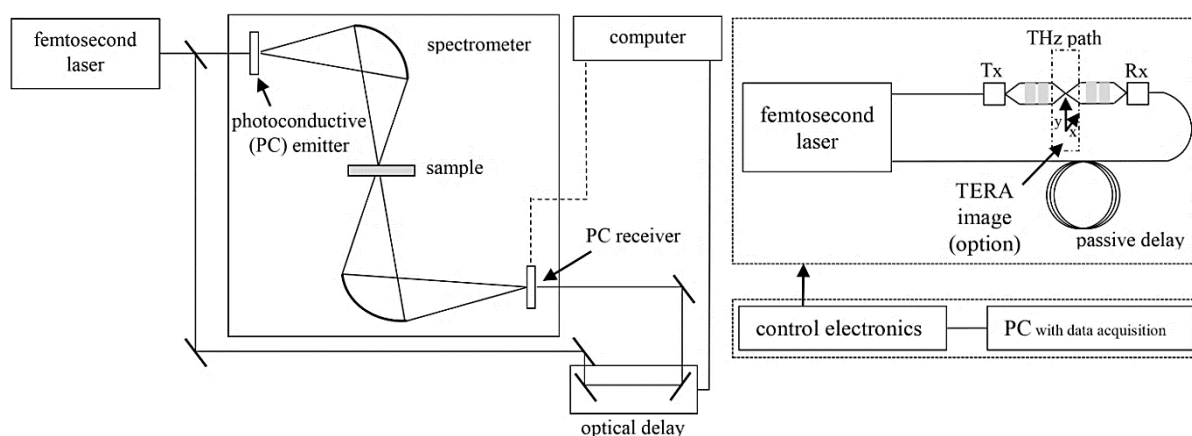


Figure 10 Schematic TPI Spectra 3000 showing coherent detection mechanism (left), Tera OSCAT spectrometer layout (right). [79]

4.3.3 Terahertz imaging

The THz TDS system can be also used for imaging. The image information can be obtained from the THz pulse (or phase) amplitude. Most of the systems are using raster scanning of THz beam or object, where one pixel contains large

amount of information to be processed (forming a THz waveform). To record the THz pulse waveform, the optical delay line requires to be scanned during the measurement of one pixel, which is fast in the case of standard step scan optical delay line (such time must be multiplied according to the required number of pixels for the image). Generally employment of the phase detection leads to detection of the peak arrival time change or the first zero crossing of the pulse. Changes in the arrival time are given by: [72]

$$\Delta t = \frac{1}{c} \int n(z) dz \quad (37)$$

where z is the THz beam direction and $n(z)$ is the refractive index in this direction, $c = 299792.458$ km/s. Changes in the THz pulse arrival time (position function) indicate changes in the optical path length caused by the sample thickness changes or refraction index changes. The phase or pulse delay are more accurate than the amplitude in case of detection as the noise is predominant as THz pulse amplitude fluctuation. The spatial resolution is influenced by broadband emission of TDS system. The focus diameter or minimum waist is frequency dependent. When a particular frequency interval is utilized to generate the image, the spatial resolution is roughly proportional to selected interval average wavelength; when the whole spectrum is utilized, the spatial resolution is determined by the frequency component wavelength with the largest amplitude. By calculating the spectrum for all pixels at frequencies from 0.3 to 2.4 THz a 3D image is attained with the possibility to define the spatial distribution of the compounds. When talking about 3D imaging (the time-of-flight imaging), the setup consists of TDS emitter illuminating the sample and a receiver detecting reflected pulses. After illumination with the THz pulse, the reflected THz pulse is generated in each step and in reflections measured signal consists of series of such pulses with unique time delay for each. The time delay between two pulses provides information about the optical thickness of the layer among them, whereas the amplitude of each pulse brings the information about the refractive index change magnitude at the layer interface. The depth resolution is assessed by the temporal duration of the THz pulse (shorter = better). [72],[75]

Concisely about the terahertz pulsed imaging (TPI), the beam splitter separates the NIR laser light into the excitation beam and the probe beam. THz pulses are generated by optical excitation of biased photoconductive antenna. Such emitted THz pulses are collimated and focused onto the sample by the silicon lens system. Reflected and backscattered pulses are afterwards collected and focused onto the unbiased photoconductive antenna for the laser-gated THz detection. [76]

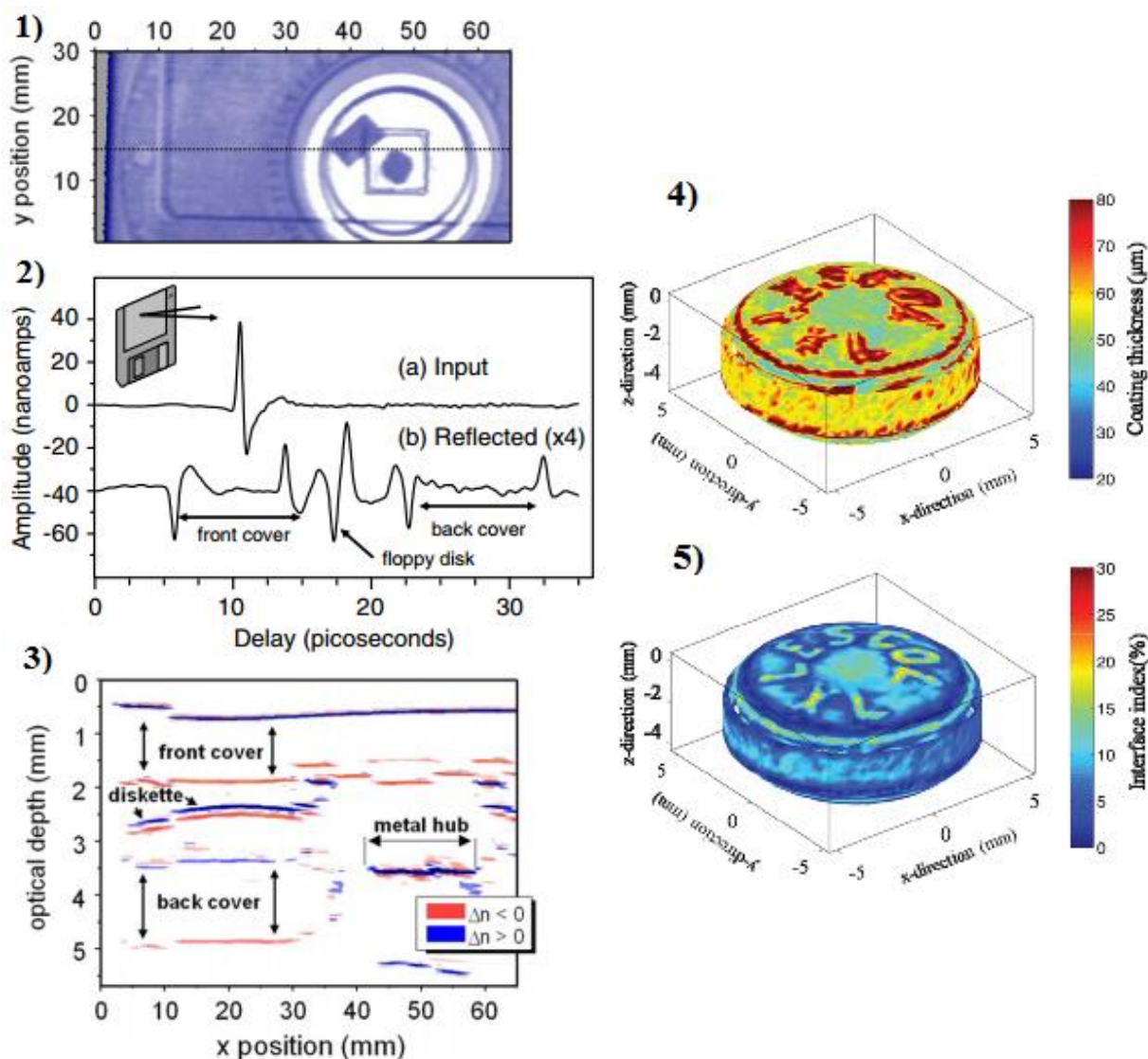


Figure 11 2D THz imaging: 1) THz reflection image of a floppy disk cut generated by the pulse amplitude. The image shows total terahertz power at each pixel as a function of two lateral dimensions. 2) THz pulse measured in the reflection geometry (a) the input pulse measured with a mirror at the confocal reflection location, (b) THz pulse reflected off of conventional floppy disk. Reflection from each dielectric interface can be seen. Lower curve is vertically offset for clarity, the upper one shows the input THz pulse reflected from a mirror. 3) Time-of-flight slice along one row of the 1) in the body of dotted line. All buried internal interfaces are clearly resolved, the metal hub on the right side is a strong reflector (rise to a multiple reflection appearing in the shadow region beneath it). 4) Example of 3D map of coating thickness of unstressed tablet Lescol[®] XL. 5) Example of 3D map of interface index of unstressed tablet Lescol[®] XL. [72],[76],[80],[81],[82]

The transient electric field of the THz pulses is recorded as a function of the time delay between the THz pulse and the optical probe pulse. The whole THz waveform can be measured in less than 10 ns by sweeping the optical delay using the rapid variable delay stage. The contrast mechanism is provided by portion of the THz pulse reflected back to the detector from material while penetrating through different coating layers. For most imaging systems, it is appropriate to investigate the sample in the chamber purged with dry nitrogen gas or evacuated

thorough the measurement to decrease the effect of water vapour absorption. The TPI is a 3D imaging technique where each measurement provides a true 3D data cube. The lateral resolution is limited by the wavelength of the THz radiation and the depth resolution is limited by the pulse duration. All pixels can be mapped out in a 2D map as well. Both 2D and 3D can be used for dataset's tomographic slices extraction. [76]

The coating thickness d can be extracted directly from the time-domain waveform: [76]

$$d = \frac{\Delta tc}{2n} \quad (38)$$

where Δt is the time delay between the surface reflection and the reflection from the coating/core interface, c is the speed of light and n is the refractive index of the coating layer. Another parameter extracted from the waveform is the interface index II calculated as:

$$II = \frac{|R_n|}{|R_0|} \quad (39)$$

where R_n is the amplitude of the reflection at the n^{th} interface, R_0 is the amplitude of the reflection from the surface of the sample. [76]

4.3.4 Fourier-transform infrared spectroscopy

Infrared (IR) spectroscopy is one of the most important analytical techniques enabling to study any type of sample in any state. Processes of change (vibration and rotation) associated with spectroscopy are represented in terms of quantized discrete energy levels $E_0 - E_n$. Each atom or molecule in a system is existing in one or other of these levels. When the molecules are assembled, the distribution of all atoms or molecules is among these various energy levels. The latter are the function of integer (the quantum number) and a parameter associated with the particular atomic or molecular process associated with the state. When a molecule interacts with radiation, the energy quantum is emitted or absorbed. The energy of the radiation quantum is to fit the energy gap $E_n - E_{n-1}$. The quantum energy is related to the frequency: [83]

$$\Delta E = h\nu \quad (40)$$

where h is the Planck's constant 6.66×10^{-34} J/s. The radiation emission/absorption frequency for the transition between the energy states E_0 and E_1 is given by: [83]

$$\nu = \frac{(E_1 - E_0)}{h} \quad (41)$$

The uptake of energy of quantized absorption is a deactivation mechanism, when the atom or molecule returns to its original state. The loss of energy quantum by emission is excitation mechanism. If the molecule is to show infrared absorption, the electric dipole moment of the molecule have to change during the vibration or rotations, which is also called the selection rule for the IR spectroscopy. IR absorptions are not infinitely narrow, several factors affecting the broadening exists:

- Doppler effect – radiation shifted in frequency while the radiation source is moving to/from the observer,
- collision between molecules,
- finite lifetime of states involved in the transition, which energies are not precisely defined,
- relationship between the lifetime of excited state and absorption bandwidth with transition to excited state. [83]

The vibrational modes frequency can be explained by stiffness, characterized by the proportionality constant k (force constant), and reduced mass μ providing calculations by combinations of individual atomic masses: [83]

$$\frac{1}{\mu} = \frac{1}{m_1} + \frac{1}{m_2} \quad (42)$$

where m_1 and m_2 are atoms' masses at the ends of the bond. The calculation of the reduced mass can be expressed as:

$$\mu = \frac{m_1 m_2}{m_1 + m_2} \quad (43)$$

Hooke's law describes the motion of a vibrating spring (stretching frequency of a bond) – i.e. simple harmonic oscillator, where the frequency energy is dependence on distance (molecule can absorb energy of any wavelength): [84]

$$\nu = \frac{1}{2\pi} \left[\frac{k}{m} \right]^{1/2} \quad (44)$$

quantized to follow quantum mechanics rules:

$$E = \left(n + \frac{1}{2}\right) h\nu \quad (45)$$

where m is the mass and n is the quantum number, while for the case of diatomic molecule showing the relationship between masses, the bond's force constant ($k \approx 5/10/15 \times 10^5$ dyne/cm) and wavenumber (ν), showing lighter atoms and stronger bonds leading to higher frequencies:

$$\nu = \frac{1}{2\pi c} \left[\frac{f(m_1+m_2)}{m_1 m_2} \right]^{1/2} \quad (46)$$

The molecule can absorb radiation only when the incoming infrared radiation is of the same frequency as the fundamental modes of vibration of the molecule, the rest frequencies are transmitted (some of the light can be also reflected back to the source). The equation relating the force constant, reduced mass, absorption frequency with the modification to use wavenumbers for bond vibrational frequencies directly is: [83], [84]

$$\bar{\nu} = \frac{1}{2} \pi c \sqrt{\frac{k}{\mu}} \quad (47)$$

The absorbance A , also describable by intensities, can be calculated as a logarithm of the reciprocal of the transmittance: [83]

$$A = \log_{10} \frac{1}{T} \quad (48)$$

where T is transmittance.

The vibration may involve change in bond length (stretching) or bond angle (bending). Some bonds can stretch in-phase (symmetrical stretching), some out-of-phase (asymmetric stretching); when a molecule has different terminal atoms then there will be varying proportions of stretching motion of each group – i.e. varying amount of coupling. Similarly, contributing bending vibrations can be in-plane and out-of-plane bending vibrations. The complexity of the infrared spectrum increases from coupling the vibrations over a large part (or complete) molecule, described by so-called skeletal vibrations, which corresponds with the fingerprint (pattern) of the molecule as a whole, rather than the specific internal group. [83]

The Fourier transform is a standard analytical tool, ideal for mathematical study of system, defining the relationship between the intensity falling on detector $I(\delta)$

and the spectral power density at particular wavenumber $B(\bar{\nu})$ (respectively $\bar{\nu}$): [83]

$$I(\delta) = \int_0^{+\infty} B(\bar{\nu}) \cos(2\pi\bar{\nu}\delta) d\bar{\nu} \quad (49)$$

$$B(\bar{\nu}) = \int_{-\infty}^{+\infty} I(\delta) \cos(2\pi\bar{\nu}\delta) d\delta \quad (50)$$

These functions are known as Fourier transform pair, which is interconvertible. The Fourier basic functions are pure sinusoids. Equation 49 describes the variation in power density as a function of difference in pathlength (an interference pattern), while formula 50 depicts variation in intensity as a function of wavenumber. The main task to obtain Fourier transform IR (FTIR) spectra is creation of interferogram with and without the sample in the beam and transforming such interferogram into: [83], [75]

- spectra of the source with sample absorption,
- spectra of the source without sample absorption.

The ration between former and latter is responding the double-beam dispersive spectrum. The invention of the fast Fourier transform (FFT) is a significant development of the classical Fourier transform providing a feasible method for computing it. [83],[75]

Commonly used interferometer used for FTIR spectroscopy is the Michelson interferometer consisting of two perpendicularly plane mirrors (one travelling in a direction perpendicular to the plane). The beamsplitter is a semi-reflecting film (from material selected according to the examined region – germanium/iron oxide coated on potassium bromide/caesium iodide for MIR or NIR, organic films for FIR region) bisecting the planes of these mirrors. The collimated beam of monochromatic radiation of wavelength λ passes to beam splitter (if ideal, than the radiation will be divided equally to reach each mirror); these two beams are reflected from mirrors to return to the beamsplitter to recombine and interfere. 50 % of the beam reflected from the fixed mirror is transmitted through the beamsplitter, and the rest is reflected back in the source's direction. The transmitted beam is the beam emerging from the interferometer at 90° to the input beam (and is detected in the FTIR spectroscopy). The moving mirror (essential component of the interferometer) creates the optical path difference between interferometer's two arms as the path that one beam travels is fixed length and the other is constantly changing as its mirror moves. The moving mirror must be

properly aligned and efficient of scanning two differences so that the path difference corresponds to the known value. [83],[85]

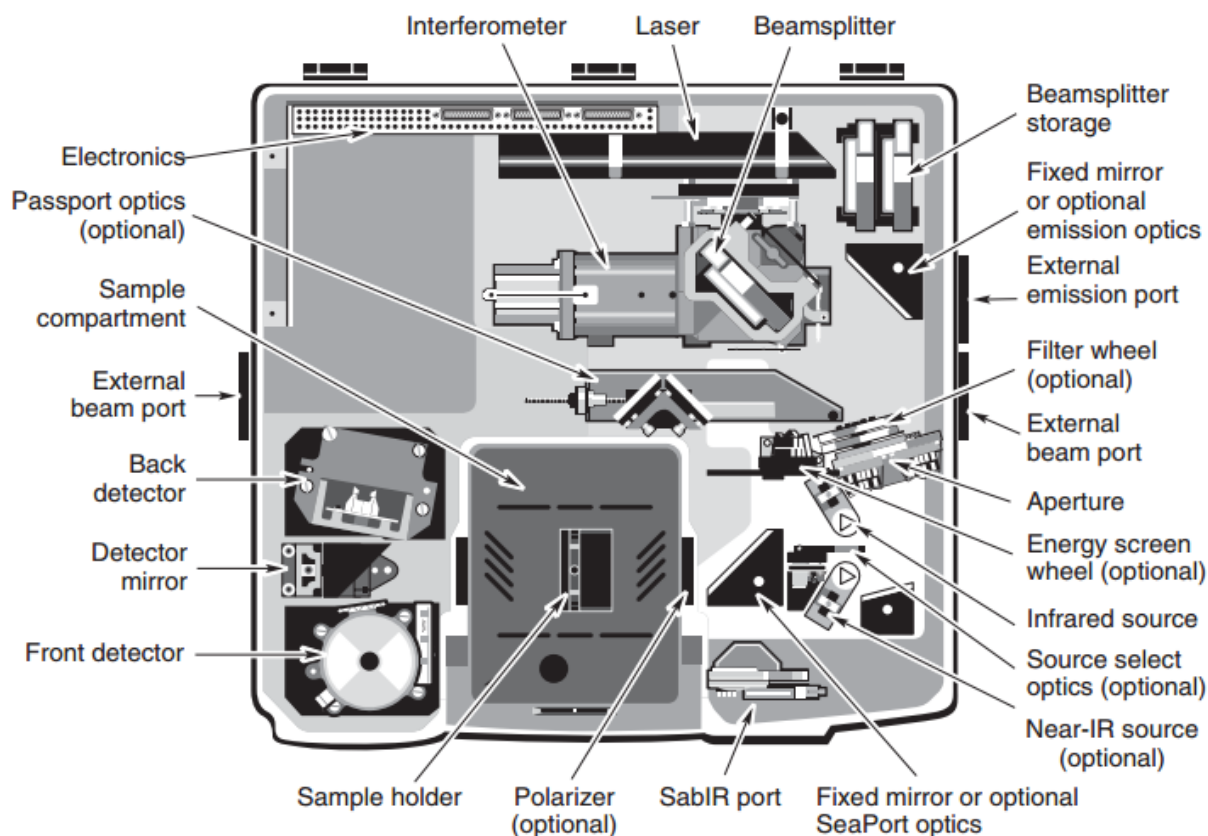


Figure 12 Example of FTIR spectrometer NICOLET layout by Thermo Electron Corporation [85]

The apodization process means removal of the side lobes (or pods) by the interferogram multiplication by a suitable function (which makes the interferogram intensity falling smoothly to zero at ends) before the Fourier transform is applied. The general purpose apodization is a cosine function providing a good compromise between reduction in oscillations and deterioration in spectral resolution:

$$F(D) = \frac{1 + \cos(\pi D)}{2} \quad (51)$$

where D is the optical path difference. For more accurate band shapes, more sophisticated mathematical function are needed. [83]

As a source of the FTIR spectrometer, different springs are used: Globar or Nernst for the MIR, high-pressure mercury lamps for the FIR, and tungsten-halogen lamps for the NIR. For detection in MIR region (the spectral range from 4000 to 400 cm^{-1} , where fundamental vibrations are typically excited), a pyroelectric device incorporating deuterium tryglycine sulfate in the temperature-resistant

alkali halide window (for routine) and mercury cadmium telluride cooled to liquid nitrogen temperature (for more precise work) detectors are usually utilized. As a detector for the FIR region, germanium or indium-antimony detectors are used (operating at liquid helium temperatures), while the NIR region detectors are mostly lead sulphide photoconductors. [83]

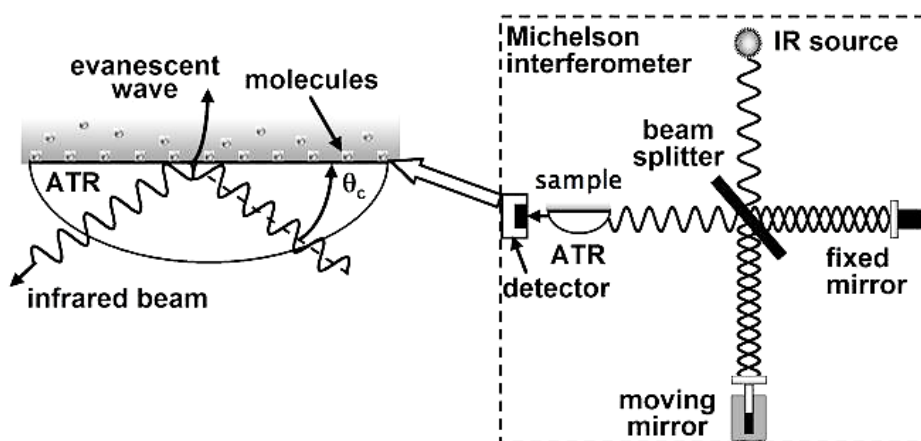


Figure 13 Example of ATR FTIR spectrometer layout [86]

The total internal reflection, the phenomenon used by ATR, describes the radiation beam entering the crystal and undergoing the total internal reflection when the angle of incidence at the interface between the sample and crystal is greater than the critical angle (function of the refractive indices of the two surfaces). The beam penetrates a fraction of a wavelength beyond the reflecting surface and when the material (selectively absorbing radiation) is in the close contact with the reflecting surface the beam loses energy at the wavelength where the material absorbs. The signal will be therefore attenuated in spectral regions where the sample is absorbing energy and the spectrum will be therefore obtained. Inside the crystal, the IR light undergoes several reflections to increase the interaction with the sample. ATR produces very short pathlength of the IR light in the sample, which makes the technique ideal for highly absorbing materials (e.g. aqueous solutions, rubber, polymers). The resulting attenuated radiation is measured and plotted as a function of wavelength by the spectrometer and intensifies the sample's absorption spectral characteristics. The penetration depth is given by following equation (for non-absorbing medium):

$$d_p = \frac{\lambda}{n_1 \sqrt{\sin^2 \theta - \left(\frac{n_2}{n_1}\right)^2}} \quad (52)$$

where n_1 is the sample's refractive index, d_p is the penetration depth, n_2 is the crystal's refractive index, θ is the incident radiation angle. The crystals for the ATR cells are non-soluble in water and with very high refractive index (e.g. ZnSe, Ge, KRS-5), and together with different designs enables examination of both liquid and solid samples. [83],[87]

Table 3 The properties of commonly used ATR crystals [88],[89]

Material	Spectral region (cm ⁻¹)	Refractive index n_1	Depth of penetration at 45°, 1000 cm ⁻¹ (μm)	Hardness (Knoop)
ZnSe	20,000 - 500	2.43	1.66	130
ZnS	22,000 - 750	2.25	1.54	355
Ge	5,000 - 600	4.01	0.65	550
Si	10,000 - 100	3.42	0.81	1150
Diamond	45,000 - 10	2.40	1.66	9,000

4.3.5 X-ray photoelectron spectroscopy

The fundamentals of X-ray photoelectron spectroscopy (XPS), a quantitative surface analysis of chemical composition, empirical formula, chemical and electron state of elements in sample, originates in the photoelectric effect (enabling to study the composition and electronic structure of the matter) discovered by Hertz in 1886 and further explained by Einstein (1905). The first XPS was developed by a Swedish research group of Siegbahn in mid-1960s and was called Electron spectroscopy for chemical analysis, and commercially available instruments were introduced in early 1970s. Measurements are performed in ultrahigh vacuum to control the cleanliness of the surface and to reduce the electron scattering on gas molecules. Device is equipped with the X-ray source (providing the photons beam with set characteristics) focused on the sample surface. Mg K α (1253.6 eV/0.70 eV), Al K α (1486.6 eV/0.85 eV), or monochromatic Al K α (1486.7 eV/0.25 eV) soft X-rays are usually used. In some cases, e.g. to excite the higher energy electron levels (1s level of heavy elements), Si K α (1739.5 eV/1 eV), Zr L α (2042.4 eV/1.7 eV) and Ti K α (4510.0 eV/2 eV) high energy anodes are used. These photons have limited penetrating power in the solid (order of 1 – 10 μm) interacting with atoms in surface region. Photoelectrons emitted from the sample at characteristic energies are analysed by a suitable analyser. The amount of electrons that escaped from the sample without energy loss is usually measured in the range of 20 – 2000 eV, with lateral resolution of few to 100 μm. The kinetic energy of emitted electrons (K.E.) follows

fundamental energy conservation equation for photoemission: [76],[90],[91], [92],[93],[94],[95],[96],[97]

$$h\nu = E_B + E_K + \varphi_a \quad (53)$$

where h is the Plank constant, ν is the photon frequency, $h\nu$ is the incident photon energy, E_B is the electron in the atom binding energy, E_K is the kinetic energy of emitted electrons, φ_a is the spectrometer work function. Binding energies' (B.E.) origin is related to the Fermi level E_F (corresponding to zero B. E.) and may be regarded as the energy difference between the initial and final states after the photoelectron has left the atom, while kinetic energies are connected with the vacuum level E_V ; differences between both levels correspond to the analyser function ϕ_a . When one knows the spectrometer work function and measures electron kinetic energies, it is possible to determine binding energies of various core electrons and valence electrons involved in chemical bonding. The spectrum consists of series of peaks on the background signal increasing at low kinetic energy because of secondary electrons (photoelectrons) inelastically scattered in the way out of the sample. Because the electrons (in solids) mean free path is very small, only the top few atomic layers of originated electrons are detected.

$$\varphi_a = E_F - E_V \quad (54)$$

This quantity is to be determined by calibration for the spectrometer used. [96]

The binding energy E_B is dependent on different terms [98]:

$$E_B = E_{B(atom)} + \Delta E_{chem} + \Delta E_{Mad} + \Delta E_{rel} \quad (55)$$

where the chemical shift ΔE_{chem} reflects the influence of chemical bonds with neighbouring atoms, the ΔE_{Mad} is the Madelung constant describing the lattice in the solid electrostatic energy, and the ΔE_{rel} is the relaxation effect describing many-body effects in the 1-hole final state of the investigated many-body object. Due to the following effect, multiple structures may occur:

- spin-orbit coupling – coupling within the same orbital state (spin s of the atom's (a) electron interacts with its orbital moment l , described by the Hamiltonian):

$$H_{sl} = as \times l \quad (56)$$

- magnetic spin-spin exchange splitting – full inner s-shells are spin-up and spin-down electron occupied (normally, spins are equal with same energy)

and wave function; but under certain conditions, the energy splitting of the s shell is caused).

To quantify the amount of each element, the integrated area of a particular peak should be divided by the corresponding relative sensitivity factor. A generalized equation for atom fraction determination (C_x) of constituent x in the sample is: [93],[97]

$$C_x = \frac{\frac{I_x}{S_x}}{\sum \frac{I_i}{S_i}} = \frac{N_x}{\sum N_i} \quad (57)$$

where I_x is the peak area, N_x stands for number of elements moles, S_x is the atomic sensitivity factor of the x^{th} element, denominator corresponds to the atomic fraction of other elements in the sample. When a homogenous distribution of elements is assumed, a strong line for each element of the spectrum is to be analysed. When the homogeneity requirement is not fulfilled, the homogeneity assumption may be used as a starting point for consequent calculations. Reference published data on elemental sensitivity factors can be used to determine the S , with consideration of measurement conditions. By measuring the high resolution/core level peaks, the chemical states are possible to be identified.

The position of the electron energy analyser with respect to the sample can be changed in order to vary the analysis depth of selected sample, resulting in the alteration of electron' take-off angle and a longer escape depth for electrons interdicting from layers below the surface influencing the attenuation of the intensity of the electrons that belong to bulk atom with regards to those on the surface. A procedure (utilization of angle-dependency) to estimate the thickness d if material and bulk atoms with different chemical shifts are used (e.g. W4f levels of tungsten coated glasses – take-off angles 90° and 30°) is calculated as follows for the oxide-overlayer: [94]

$$\frac{I_{Wox}}{I_W} = \frac{1 - \exp\left(\frac{-d}{\lambda \sin\theta}\right)}{\exp\left(\frac{-d}{\lambda \sin\theta}\right)} \quad (58)$$

where λ is the attenuated length, θ is the electron take-off angle with regard to the surface normal. Using this calculation, the approximate thickness of this native tungsten oxide is 4.5 nm. This method is rapid and versatile probe for a detection of concentration of element/certain functional group on the surface containing a uniform layers with thickness less than 10 nm.

Photoionization generally leads to two type emitted electrons (the photoelectron and the Auger electron). Auger electrons can be emitted together (roughly 10^{-14} s after photoelectric effect) with photoelectrons during photoelectric process because of relaxation of excited ions remaining after photoemission. In the Auger process, the outer electron falls into the inner orbital vacancy and the second electron is simultaneously emitted carrying off the excess energy. The Auger electron, which is independent of the mode of the initial ionization, has the kinetic energy equal to the difference between the energy of the initial and doubly charged final ion. [95]

The main information is obtained from the core level peaks and the nomenclature used to describe XPS features is based on the momenta associated with the orbiting electron paths around nuclei indicated by quantum numbers (n, l, j). The XPS uses the spectroscopic notation where first is the principal quantum number $n = 1, 2, 3, \dots$ followed by $l = 0, 1, 2, \dots$ (indicated as s, p, d, f) and finally the j value as a suffix ($1/2, 3/2, 5/2, \dots$). Another information obtained during experiments are different intensities (governed by different core shells ionization efficiencies designed by ionization cross section) and widths. The line width is defined as the full width at half-maximum intensity and is a convolution of several contributions – core level natural width, X-ray line width, analyser resolution. [96]

To interpret acquired data, two commonly applied techniques are linear least squares fitting (LLSF) and factor analysis (FA). Those techniques assume that each spectrum can be represented by the component spectra's linear combination: [97]

$$[D] = [R] \times [C] \quad (59)$$

where $[D]$ is the recorded XPS data matrix, $[R]$ is independent component spectra matrix and $[C]$ is weighting factors/concentrations matrix or linear least squares minimisation in LLSF. The FA analysis is more complex as first the number of independent components is identified and consequently true component spectra together with concentrations are determined.

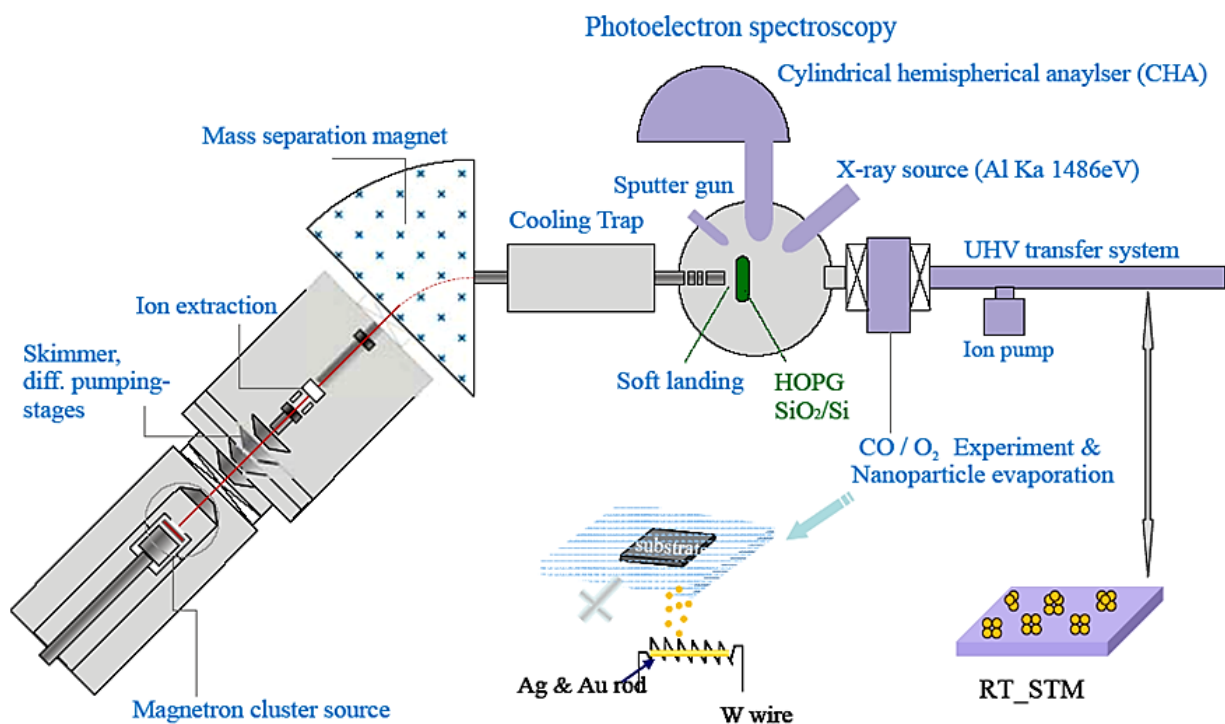


Figure 14 X-ray photoelectron spectroscopy layout [99]

The instrument contains mainly these parts: the primary beam source (X-ray source consisting of the filament (cathode) emitting thermal electrons through heating), the electron energy analyser (combined with detection system), and sample stage. The electron spectrometer and sample room is operating under ultra-high vacuum (UHV) – $10^{-8} - 10^{-10}$ Torr, because low energy electrons are scattered (elastically and non-elastically) by residual gas molecules leading to loss of intensity and energy, and because lowering the vacuum level under the e.g. 10^{-6} Torr will result in formation of the residual gas monolayer absorbed on the sample surface in < 1 s. The vacuum is generally based on diffusion, sputter ion, turbo molecular pumps combined with assistant tools. The UHV systems need to be occasionally decontaminated (chamber walls, stage, and contact points). For detection of electron energy, two main types of detectors are used – the cylindrical mirror analyser and the hemispherical sector analyser, while the predominant type of detector is the hemispherical sector analyser, even for multifunctional Auger electron & X-ray photoelectron spectrometers. This detector is used for electron dispersion analysis, and is designed to have a constant the highest possible energy resolution for photoelectrons detection with best energy resolution in 0.4 eV. For detection, two modes are used – fixed analyser transmission (also called constant analyser energy mode) and constant retard ratio (also called fixed retard ratio; used for Auger electron spectroscopy). For improved sensitivity, the multichannel

detector system is used electron detection. The pass energy E_{pas} is a crucial parameter of a setup (hemispherical capacitor). The highest contribution to the noise in the spectrum stems from electrons excited by low kinetic energy secondary processes. To avoid such noise, only electrons with $E_K > E_{pas}$ are to pass. In the XPS instrument, the sputtering is used by means of energetic primary ions beams. The sputtering is not only used to measure depth profiles (by measuring the recorded peaks intensity vs. sputtering time/etching), but also clean the sample before the analysis (remove atmospheric contamination and dirt; it must be stressed out that this technique is a destructive one). This is done by the ion gun (cold static spot gun, electron impact source or duoplasmatron type), which is turned off during the spectrum measurement. [97],[98]

XPS is used to analyse the surface chemistry of a material in its as-received state, or after some treatment, for example: fracturing, cutting or scraping in air or ultra-high vacuum to expose the bulk chemistry, ion beam etching to clean off some or all of the surface contamination (with mild ion etching) or to intentionally expose deeper layers of the sample (with more extensive ion etching) in depth-profiling XPS, exposure to heat to study the changes due to heating, exposure to reactive gases or solutions, exposure to ion beam implant, exposure to ultraviolet light.

4.3.6 Surface wettability and contact angle measurement

Surface is an interaction area for any communication between material and surroundings. Solid matter is more or less solid body, which surface is characterized by surface energy. Due to a plasticity, changes in surface body shape (that are said to be solid) abide by same laws as surface changes in liquid shapes only with a difference in very small changes dependent on substance type and temperature. Changes in shape are enabled by:

- Particles exchange between surface and substance vapours.
- Surface and volume movement of particles forming the solid body. [14]

Object surface is determined by its appearance and makes interface between two phases. Functional properties are not only dependent on outer layer (forming interface), but on area oriented below the surface. Such properties are certain classification degrees with surface area allocation. Surface polarity is a cause of surface energy formation, which is expressed by surface tension. The higher the degree of surface tension the more polar solid surface or liquid is. [100]

Contact angle measurement is one of the directly measurable characteristics of solid/liquid/gas phase interface. It is an angle that contain tangent to droplet surface led in a point of droplet contact with interface. The measurement can be often distorted by a surface inhomogeneity influence.

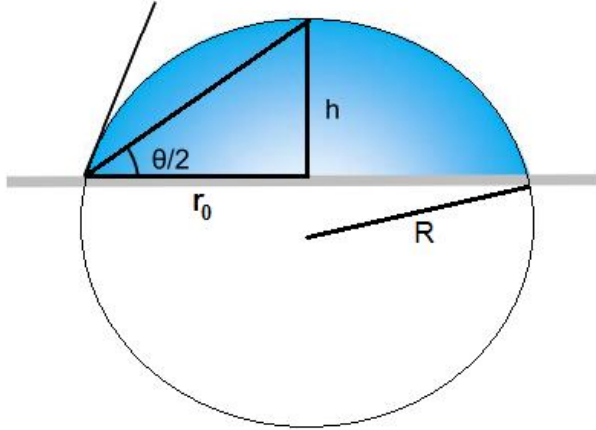


Figure 15 Droplet profile analysis [101]

To be able to measure the contact angle during the early years of the technique, the droplet should be extremely small to get insignificant circular shape error. In this analysis, the liquid drop is assumed to be part of a sphere. For the droplet height is applied: [101]

$$h = R(1 - \cos\theta) \quad (60)$$

The radius in the droplet contact is given by: [101]

$$r_0 = R\sin\theta \quad (61)$$

By integration of equation 60 and 61, we get: [101]

$$\frac{h}{r_0} = \frac{1 - \cos\theta}{\sin\theta} = \tan\left(\frac{\theta}{2}\right) \quad (62)$$

After measuring the h and r_0 , the contact angle can be consequently calculated. If the droplet is spacious, the above mentioned parameters can be biased by gravitation so that the equation cannot be used and more sophisticated calculations are needed. If one knows the volume of the droplet, the contact angle can be calculated from one of the following relations: [101]

$$\frac{r_0^3}{V} = \frac{3\sin^3\theta}{\pi(2 - 3\cos\theta + \cos^3\theta)} \quad (63)$$

$$\frac{r_0^2 h}{V} = \frac{3(1+\cos\theta)}{\pi(2+\cos\theta)} \quad (64)$$

The wetting angle (droplet shape) is dependent on inter-surface energies of three coexisting phase interface between [100]:

- Solid and liquid phase (γ_{sl}).
- Solid and gaseous phase (γ_{sg}).
- Liquid and gaseous phase (γ_{lg}).

The system is formed to minimize the total potential energies of all phase interfaces (with the possibility to vanish the gravitation effect).

Following liquids are the most widely used ones as probe liquids. The values of the component of the surface tension for these liquids are shown in Table 4.

Table 4 Examples of surface tension components' values for selected liquids [93]

Liquid	γ^f	γ^{LW}	γ^{AB}	γ^-	γ^+
Water	72.8	21.8	51.0	25.5	25.5
Glycerol	64.0	34.0	30.0	57.4	3.9
Formamide	58.0	39.0	19.0	39.6	2.3
Ethylene glycol	48.0	29.0	19.0	30.1	3.0
Diiodomethane	50.8	50.8	0.0	0.0	0.0

After the droplet is placed on solid material surface, following cases may happen [100],[102],[93]:

- If the material surface energy is higher than sum of liquid surface energy and solid-liquid inter-phase energy ($\gamma_{sg} > \gamma_{sl} + \gamma_{lg}$) the liquid spreads on solid surface. The final energy of system is lower as the solid-gas phase interface is replaced by two interfaces – solid-liquid and liquid-gas (both with same surface area as former interface). The limit case is called complete wetting ($\theta = 0$, $\gamma_{sg} = \gamma_{sl} + \gamma_{lg}$).
- If $\gamma_{sg} < \gamma_{sl} + \gamma_{lg}$, the droplet is in equilibrium state characterized by the contact wetting angle – the angle that contain tangent to droplet surface with solid-liquid interface in the point of wetting line. The size of angle is given by the Young-Dupré equation:

$$\gamma_{sg} = \gamma_{sl} + \gamma_{lg}\cos\theta \quad (65)$$

According to the wetting angle, liquids can act as following on solid surfaces [102]:

- Wet – $0 < \theta < 90^\circ$ ($0 < \cos\theta < 1$), where $\gamma_{sg} > \gamma_{sl}$.
- Non-wet – $90 < \theta < 180^\circ$ ($0 > \cos\theta > -1$), where $\gamma_{sg} < \gamma_{sl}$.
- Complete non-wet – $\theta = 180^\circ$, where $\gamma_{sg} = \gamma_{sl} - \gamma_{lg}$.

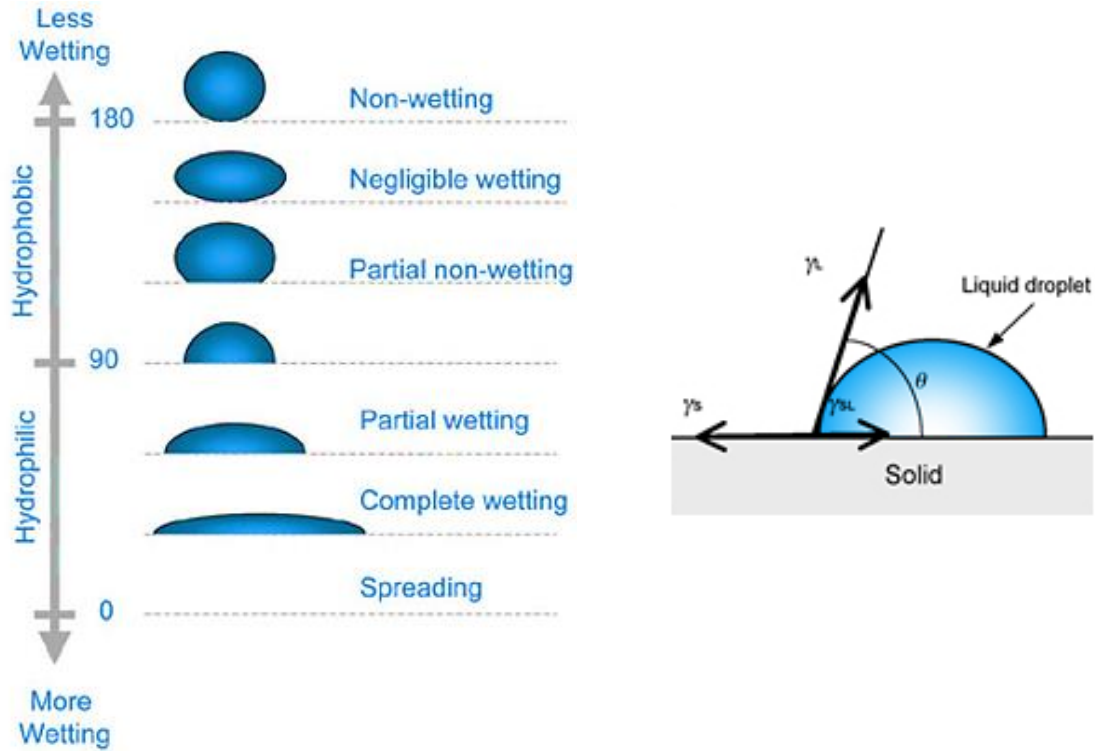


Figure 16 Surface tension and contact angles [102]

As the ideal solid surface is completely flat and chemically homogenous, the real data must be counted into the whole calculation. The real surfaces are rough and are chemically heterogenic due to the presence of impurities. When the examined surface is rough, the Wenzel equation is used [100]:

$$\cos\theta = \varepsilon \cos\theta_{zd} \quad (66)$$

where ε is surface roughness, θ is contact angle defined for ideal surface, and $\cos\theta_{zd}$ is contact angle on rough surface. Sub-microscopic and microscopic sizes surface roughness and especially chemical inhomogeneity of surface are significant factors for measured values of contact angles. The chemical inhomogeneity is described by Cassie equation

$$\cos\theta_{zd} = \Phi_1 \cos\theta_{zd} + \Phi_2 \cos\theta_{zd} \quad (67)$$

where indexes $1, 2$ stands for different surfaces (clear solids with impurities), Φ_1 , Φ_2 their relative representation in measured solid surface.

One of the often used methodology for calculation of surface energy is the Fowkes method. When intercourse of two random phases occurs, the Lifshitz-van der Waals component γ^{LW} is made by three types of power: [103]

- Coulomb forces (γ^C) – significant for permanent dipole (e.g. water, ammoniac, alcohols),
- induction powers (γ^I) – binding of fortified dipoles by electrostatic forces,
- dispersion powers (γ^D) – dispersion compound of surface energy.

Lifshitz-van der Waals powers contain all electromagnetic interactions based on permanent dipoles and induced dipoles. All of the three parameters above can be determinated by: [103]

$$\gamma = \gamma^C + \gamma^I + \gamma^D \quad (68)$$

Fowkes specified that the inter-phase interaction between two volume phases may occur only for powers of same type (e.g. dispersion-dispersion, polar-polar). The total surface free energy is a sum of all intermolecular forces occurring on the surface. The surface free energy can be divided only into two parts – dispersion (γ^d) and non-dispersion (γ^n). The dispersion part is set when at least one liquid is purely dispersive. Following equation is utilizable on systems, where only dispersion forces are joint for both phases (with adjustment and use of Young equation): [103],[104],[105]

$$\cos\theta = 2\sqrt{\gamma_s^d} \times \frac{1}{\sqrt{\gamma_l^d}} - 1 \quad (69)$$

If the non-polar liquid is used, then $\gamma_l = \gamma_l^d$: [103], [104], [105]

$$(1 + \cos\theta) = 2\sqrt{\frac{\gamma_s^d}{\gamma_l}} \quad (70)$$

If this equation is combined with Young-Dupré equation, the calculation for dispersion component surface tension determination formulated by Fowkes and Good is obtained (where θ , γ_l and γ_l^d are experimentally received) and valid if the liquid and solid are non-polar: [103],[104],[105]

$$W_A^d = \gamma_1(1 + \cos\theta) = 2\sqrt{\gamma_s^d + \gamma_l^d} \quad (71)$$

For polar component calculation, following equation applies: [104],[105]

$$\gamma_{sl} = \gamma_s + \gamma_l - 2(\sqrt{\gamma_s^d \gamma_l^d} \sqrt{\gamma_s^d \gamma_l^d}) \quad (72)$$

The adhesion work is a sum of dispersion and polar component: [104],[105]

$$W_A = W_A^d + W_A^p \quad (73)$$

$$W_A^p = \gamma_l(1 + \cos\theta) - 2\sqrt{\gamma_s^d \gamma_l^p} \quad (74)$$

Utilizing the last relation, the contact angle of liquid with dispersion and polar component is measured and the W_A^p is set for each liquid. The polar adhesion work is therefore: [104],[105]

$$W_A^p = 2\sqrt{\gamma_s^d \gamma_l^p} \quad (75)$$

The Owen-Wendt-Rabel-Kaelble (OWRK), based on Fowkes method, generally used when studying surface energy of polymer layers. These methods counts the surface energy in one step, with the utilization of at least two liquids with known polar and disperse components – the polar and nonpolar pair, where nonpolar liquid should have higher surface tension than expected value γ_s . The surface energy is then counted as sum of dispersion γ^d and polar γ^p components. The equations are: [100],[105]

$$\gamma_l = \gamma_l^d + \gamma_l^p \quad (76)$$

$$\gamma_s = \gamma_s^d + \gamma_s^p \quad (77)$$

$$\gamma^{tot} = \gamma^d + \gamma^p \quad (78)$$

According to Acid-base theory, the dispersion component can be divided to donor γ^- and acceptor γ^+ part: [100],[105]

$$\gamma^{AB} = 2\sqrt{\gamma^+ \gamma^-} \quad (79)$$

With the knowledge of such obtained data, it is possible to sufficiently describe hydrophilicity/hydrophobicity and surface energy of system, and set procedural parameter during production.

The contact angle measurement is used in e.g. the area of colours and paintings/lacquering, composite materials for car, aerospace, medicine, pharmaceutical, cosmetic, electronic and textile industry, packaging materials research, printing techniques, and in sphere of pesticides and fertilisers.

4.3.7 Scanning electron microscopy

A basic classification for most of the commonly available microscopes exists – optical (using a visible light and transparent lenses), charged particle (using charged particle beam and electromagnetic/electrostatic lenses) or scanning probe (using a physical probe to scan over the sample in contact or near-contact with the surface) microscope types. The 1920s discovery of accelerating electrons behaving much as light in the vacuum brought novel potentiality for the researchers. Such electrons travel in straight lines with wave-like properties (wavelength c. 100 000 times shorter than the visible light's one). The paths followed by electrons are shaped by electric and magnetic fields. The first microscope built upon these features was transmission electron microscope (TEM) in 1931 by Ruska (awarded by Nobel Prize in 1986). The first published description of the scanning electron microscopy (SEM) principle appeared in 1935 in a paper by Knoll, with consequent work of von Ardenne in 1937, the first SEM was introduced in 1942 by a team of Zworykin, Hillier and Snijder. A microscope combining both techniques (SEM and TEM) was first described in 1938 by von Ardenne under term scanning transmission electron microscopy (STEM). [106]

The SEM consist of the electron optical column, vacuum system, electronics and software. The electron gun at the top of the column produces the electron beam focused onto a fine spot (c. 1 nm in diameter) on the specimen surface. Main types of electron sources used are: tungsten (contains filament, Wehnelt cylinder and anode = triode gun, which is very stable source, providing very high total beam current), lanthanum hexaboride (LaB₆; offering higher brightness with significantly longer lifetimes) and field emission gun (FEG; offering high brightness, for some high current applications not very suitable). The tungsten filament (hairpin-shaped) excites electrons thermally so that they can be extracted from electron cloud near the filament. Such electrons are accelerated towards anode. The Wehnelt cylinder (variable potential slightly negative to the filament) heads the electrons off through a narrow cross-over improving the current density and brightness of the beam. The LaB₆ gun is based on thermionic electron

emission from heated source (LaB₆ crystal). This gun requires higher vacuum levels (s. Table 5). The emitting area is smaller than that for tungsten, which increases the brightness level but reduces total beam current capability. The FEG, where the electrons are extracted from very sharply pointed tungsten tip by an extreme high electric field provides the highest imaging and analytical results. The higher brightness and greater current density produces smaller beams with higher currents resulting in better spatial resolutions and more rigorous X-ray analysis. This type of source has two types – cold field emission and Schottky thermally assisted field emission. Cold field emission (thin tungsten wire cathode) gives very high brightness, however the beam currents are varying, and the tip needs to be frequently decontaminated by flashing. Schottky field emission (ZrO/W emitter cathode) offers high brightness (novel generation approximating the cold field emission levels) and high stable current with no flashing. [106],[107],[108]

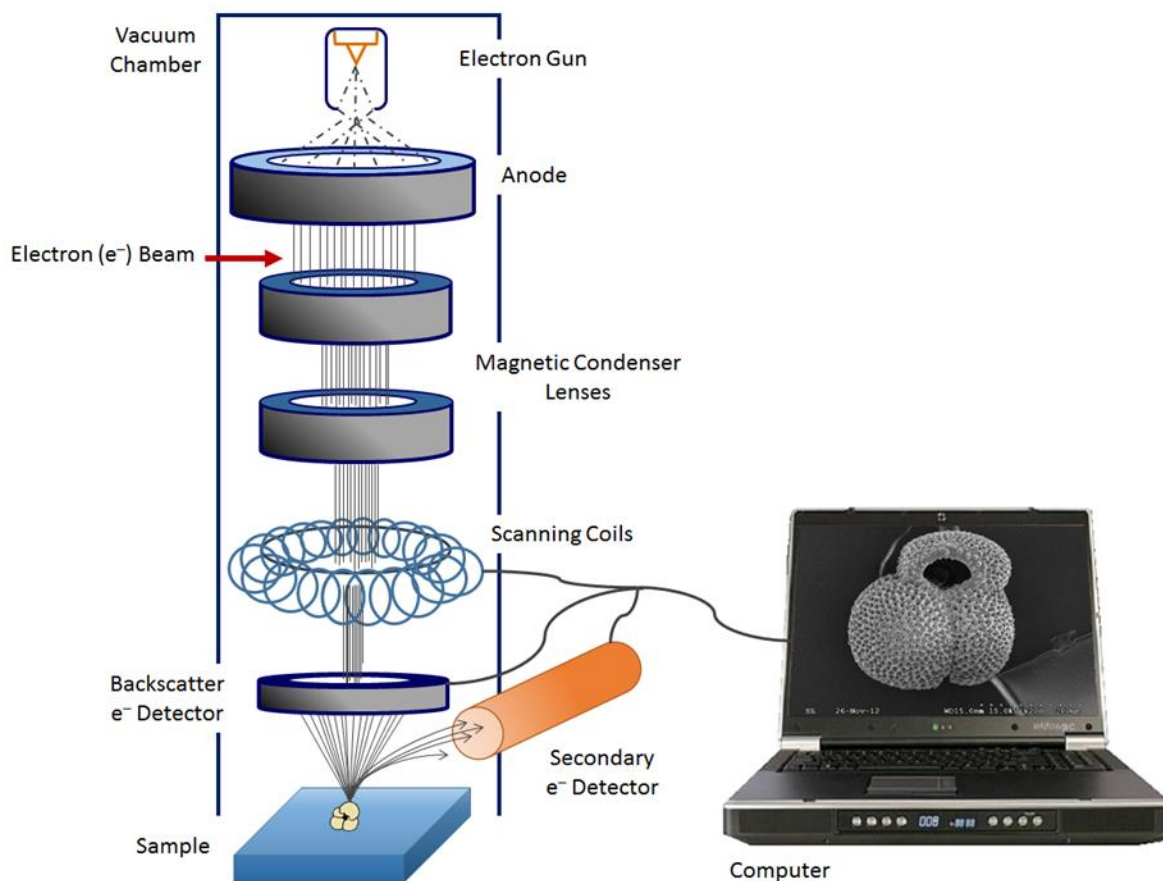


Figure 17 Scanning electron microscopy layout [109]

Table 5 Characteristics of commonly used electron guns (brightness obtained at 20 kV, FE stands for field emission); assumed from [108],[110]

	Tungsten	LaB₆	Thermal FE	Cold FE
Brightness (A/cm²str)	10 ⁵	10 ⁶	10 ⁸	10 ⁸
Lifetime (hrs)/avg.	40 - 100/50	200 - 1000/500	> 1000/ yrs.	> 1000/2 yrs.
Source size	15 - 100 μm	5 - 50 μm	< 20 nm	< 10 nm
Cathode temp. (K)	2800	1900	1800	300
Energy spread (eV)	1 - 4	1 - 3	0.7 - 1	0.3
Current stability (%/h)	< 1	< 2	< 5	> 5
Vacuum (Torr)	10 ⁻⁵	10 ⁻⁷	10 ⁻¹¹	10 ⁻¹¹

The higher the accelerating voltage, the faster the electrons. The wave particle duality concept of quantum physics asserts that all matter exhibits both wave-like and particle-like properties. The electron wavelength is given by: [106]

$$\lambda = \frac{h}{p} \quad (80)$$

where p is the relativistic momentum of electron. Knowing the rest mass of the electron m_0 with charge e , the velocity v imparted by the electric potential U is calculated by:

$$\lambda = \sqrt{\frac{2eU}{m_0}} \quad (81)$$

Integrating these two equations, one can count the wavelength at that velocity (with added relativistic correction in the last step): [106]

$$\lambda = \frac{h}{p} = \frac{h}{m_0 v} = \frac{h}{\sqrt{2m_0 eU}} = \frac{h}{\sqrt{2m_0 eU}} \frac{1}{\sqrt{1 + \frac{eU}{2m_0 c^2}}} \quad (82)$$

The beam is scanned in a rectangular raster over the specimen and intensities of various signals created by interactions between the beam electrons and the specimen are measured.

Following electrons types are used by SEM [107],[109]:

- Primary – released by electron jet, accelerated and moving through draw-tube, impinging on sample.
- Secondary – consequence of interaction of primary electrons with specimen atoms. Very low energy.

- Backscattered electrons – product of interaction of primary electrons with specimen atoms. Energy comparable to energy of primary electrons.

Detectors for backscattered electrons (BSE) and secondary electrons (SE) are generally: [106],[108],[111]

- scintillation detector (e.g. Everhart-Thornely) with following routine: electrons strike fluorescent screen emitting light, which is amplified and converted to electrical signal by a photomultiplier tube,
- solid-state detector (e.g. Schottky diode or P-N crossing) with following route: amplification of the minute signal produced by incoming electrons in the semiconductor device,
- detector monitoring the net current absorbed by the specimen or the current induced in the semiconductor junction by the incoming beam electron; enabling to perform dynamic electrical phenomena in electronic devices studies,
- detector for EDS/WDS (energy dispersive spectrometer) enabling detection of characteristic X-ray for chemical content analysis and assignment of element amount,
- EBSD detector for diffraction of backscattered electrons, mainly used for crystallographic analysis.

Stored values are consequently mapped as variations in brightness on the image display. The SE signal is the most frequently used signal varying with the topography of the sample surface (bright edges, dark recesses), while the BSE is used primarily for its strong atomic number contrast, and the X-rays are used for elemental microanalysis. The magnification is given by the ration between the displayed image and scanned area size on the specimen. [106]

The resolution is set by: [112]

$$\Delta = \frac{\lambda}{n \sin \alpha} \quad (83)$$

where $n \sin \alpha$ is the numeric aperture. The SEM's resolution depends on accelerating potential and magnification Z_m :

$$Z_m = \frac{d_0}{d_p} \quad (84)$$

where d_0 is resolution of display and d_p is the resolution of scanned specimen.

To focus the electron beam to final size ($50 \text{ \AA} - 1 \text{ }\mu\text{m}$) on the sample surface, the system (condensator/condensor and objective/projector) is used. The condensator is usually made by two lenses set not only the magnification, but also the electron beam flow on the sample surface. The last focus lens (the objective) determines the final size of the beam. The electron beam is focused by utilizing magnetic field on moving electrons. [113]

SE are produced from the emission of constituent atoms valence electrons in the sample. The energy of SE is very small, so that those generated at a deep region quickly absorbed by the sample, while those generated at the top of the surface are emitted outside of the sample, which implies sensitivity to the surface. The amount of SE is larger if the electron beam enters the sample obliquely. As a consequence of small energy and hence the near sample potential interference, the anomaly in contrast may occur if the sample is electrically charged. BSE (also called reflected electrons) are scattered backward and emitted out of the sample if the incident electrons are scattered in the sample. BSE have higher energy than SE and thus the information from relatively deep region is contained. BSE are sensitive to the sample composition. The larger the atomic number of constituent atoms in the sample, the larger the BSE yield (i.e. area consisting of heavy atoms – seems to be brighter in the BSE image and appropriate for compositional difference study). The BSE intensity is higher in the direction of specular reflection. [108]

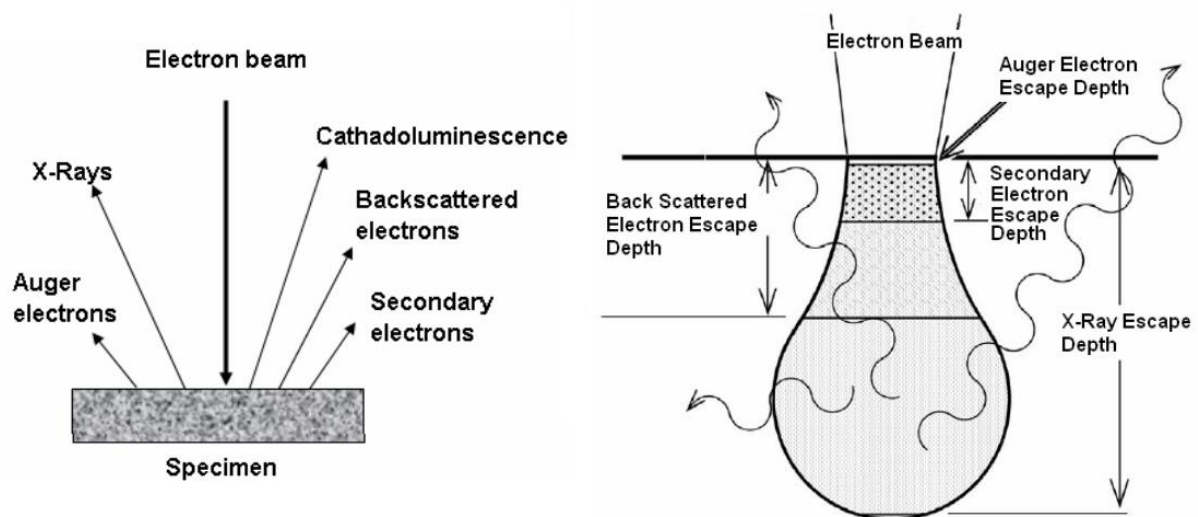


Figure 18 Signals and their origination from different volumes of interaction [106],[110],[114],[115]

The vacuum is generally made in most of the cases by an oil diffusion pump or a turbomolecular pump, whereas both systems are backed up by a mechanical

prevacuum pump. For some applications, vacuum airlocks are used as they support large chambers and fast sample exchange. [106],[108]

4.3.8 Antibacterial activity assessment

Antibacterial tests can be made as described in ISO/TC 61, SC 6, ISO 22196:2011 – Measurement of antibacterial activity on plastics and other non-porous surfaces. This standard describes the procedure for standardized antibacterial activity testing, and allowing *E. coli* and *S. aureus* for evaluating the effectivity of antibacterial surfaces (these bacterial strains should be used in every test for comparable results).

Antibacterial tests are made, in case of this thesis, by diffusion disk tests (that are same precise as dilution method if rigorously done). These tests consist in diffusion of active agent (antibacterial agent in our case) into an agar, which was before inoculated by microorganisms. Antimicrobial discs are laid onto inoculated soil, whereas 90 mm diameter plate can contain up to 6 disks distributed in circular shape. The distance between disc centres and distance from the edge of the plate must be minimally 20 mm. Active agents are applied to the agar plate on (filter-paper, polymer, etc.) discs dyed in filtrates or extracts. Active ingredients diffuse from the application spot and inhibit microorganism growth. Hence, sensitivity or resistance of selected bacteria is quantitatively and semi-quantitatively set due to inhibition zone forming around disc on agar after approved incubation time. The inhibition zone's diameter is measured in millimetres, including discs, usually in five places. The inhibition diameter is compared to boundary diameter for sensitive strains. If the examined strain forms inhibition zone of same or bigger diameter than the borderline one, the strain is said to be sensitive (or borderline sensitive) to antibacterial agent; in contrary, the strain is marked as resistant. Slight increase in boundary zones is ignored, as a sensitive strain is signed a strain with inhibition zone at least 12 mm. [116],[117]

The size of inhibition zone is influenced by:

- Sensitivity of bacteria to selected antibacterial agent.
- Amount of antibiotic on disc.
- Soil content.
- Height of agar layer.
- Speed of antibiotic diffusion into gel.

- Amount of microbial inoculum.
- Disc laying technique.

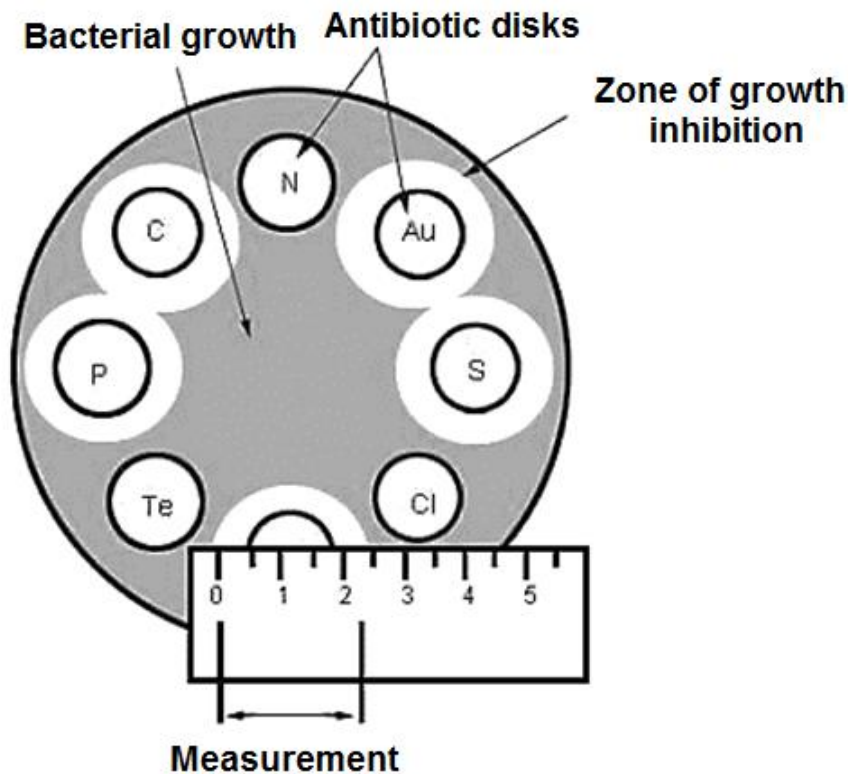


Figure 19 Disk diffusion method [118]

4.4 Experimental setup

Discharge barrier coupled plasma generator

Prepared samples were subjected to the both side low-temperature radio-frequency plasma treatment using the capacitive coupled reactor (FEMTO Diener, Germany). Radiofrequency of the reactor matching unit was 13.56 MHz and power was set to 50 W. Plasma process duration was 5 minutes, the feed rate of air as a carrier gas was 25 sccm.

Antibacterial activity assessment

The antibacterial activity of samples was tested for selected bacterial strains representing gram positive and negative bacteria by the *in vitro* inhibition

(diffusion) zone test on the agar (No. 2 M1269). Sterilized agar (3 hours, 130 °C) was equally split into Petri dishes in order to obtain the cultivation substrate. Each bacteria strain (CCM 4516, CCM 4517; $\approx 10^8$ CFU/mL) was transferred into test tubes with 10 mL of a physiological saline solution and agitated in a shaker. Then, 100 μ L of the bacterial suspension was spread onto whole agar in the each Petri dish. The circular specimens ($d = 8$ mm) were cut from all of the samples, washed in ethanol, dried and placed on inoculated agar plate. After 24 hour incubation at 37 °C, the inhibition zone diameter was measured in 5 directions, and the average value was calculated. Each test was triplicate to maintain the statistical accountability.

Contact angle measurement

The contact angle data were obtained by the Surface Energy Evaluation System (SEE system) by Advex Instruments, s.r.o. (Czech Republic). Deionized water, ethylene glycol and diiodomethane were used as testing liquids. The droplet volume was set to 5 μ l for all experiments to avoid errors connected with the gravity acting. All of the calculations were made by the SEE system software. Ten contact angle readings were averaged to obtain one representative value. The substrate surface free energy was evaluated using these data by Lifshitz-van der Waals “acid-base“ model.

Scanning electron microscopy

Scanning electron microscopy (SEM) was used for samples surface morphology evaluation. The images were obtained by the Tescan VEGA II LMU (Czech Republic) microscope. The analytical chamber is equipped by fully motorized sample manipulator. The 20,000 \times magnification at 25 kV was used as the initial one. Images of samples were taken at the 15° tilt angle for better topography observation.

Attenuated total reflection – Fourier transform infrared spectroscopy

The ATR-FTIR spectroscopy (Avatar 320 Nicolet, USA) was used for surface chemical examination. The Avatar 320 is a standard single-beam FTIR spectrometer. The spectra were collected at a resolution of 2 cm^{-1} , ATR ZnSe

crystal was placed to incident angle 45° . The wavenumber scale was calibrated by the wavenumber of monochromatic radiation of auxiliary He-Ne laser. The OMNIC 5.1b software (Nicolet Instrument corp., USA) was used for data evaluation.

X-ray photoelectron spectroscopy

The Escalab 200A (VG Scientific, UK) with the PISCES software for data acquisition and analysis was used for the X-ray photoelectron spectroscopy (XPS) to analyse chemical composition of the surface structure. For the analysis, the monochromatic Al $K\alpha$ X-ray source operating at 15 kV (300 W) was used, and the spectrometer, calibrated with the reference to Ag 3d_{5/2} (368.27 eV), was operated in CAE mode with 20 eV pass energy. The value of the ultra-vacuum was c. 10^{-8} Pa. Spectral analysis was performed using peak fitting with Gaussian-Lorentzian peak shape and Shirley type background subtraction.

Terahertz spectroscopy

The TPSTM Spectra 3000 by TeraView Ltd., which can measure in several modes depending on modules connected to the main body of the spectrometer was used as a primary terahertz time-domain (THz-TDS). The presented results were achieved using an ATR (contact angle 35°), transmission and imaging modules, which measures spectra by various techniques. The measured data of prepared samples are processed via device's software. The spectrometer was operating with resolution of 1.2 cm^{-1} (32 GHz), scanning frequency of 30 scans per second, and each measurement contained 100 scans in each point.

Another set of collected spectra (refractive indexes) came from the Tera OSCAT by Menlo Systems GmbH, which works as a classical THz-TDS system based on the pump-probe principle, which is based on a direct control of the time delay between the pulses by varying the pulse repetition rate of the laser source without any external mechanical delay line or two synchronized femtosecond lasers. The experimental setting had a standard transmission geometry. The laser source is a mode-locked femtosecond Er-doped fibre oscillator with 90 fs pulses at 1560 nm at a repetition rate of 250 MHz.

The reference was measured for both instruments only through air. Each sample was measured three times in case of SPECTRA and ten times in case of OSCAT in several places to control the accuracy of experiment. Thickness of each sample was measured at ten different places and averaged to get representative values of material for a total overview of selected behaviour in THz frequency. The measurements were not done under special conditions (e.g. nitrogen atmosphere), so the spectral contributions associated with atmospheric moisture may occurred, which in fact is not a problem for the experiment itself as we were looking for special vibrations of antibacterial surfactants. The frequency range of the experiment was set from 0 THz to 2.7 THz, and 0 THz to 4 THz using TPS Spectra™ ATR module where applicable.

Sample preparation

Samples from LDPE foil (chosen due to its chemical stability and because it is a commonly used plastics in biomedical applications and packaging industry and at the same time one of the cheapest thermoplastic polyolefin) with a 95.3 µm thickness were cut into 5 × 5 cm squares. These squares were washed by cationic tensor and consequently thoroughly rinsed with deionized water. Samples were dried for 2 hours in laboratory conditions. Such prepared samples were ready to further treatment in plasma generator and subsequent steps.

Using the RF plasma reactor for a consequent plasma pre-activation of the LDPE surface was similarly, as in the case of the material, chosen as it is a generally accessible equipment, which can also treat bigger materials in specific device settings. The samples were put in the middle of the sample holder, the ambient air was used as the process gas.

After plasma pre-activation, samples were placed in the allylamine (AA), *N*-allylmethylamine (AMA) or *N,N*-dimethylallylamine (DMAA) vapours for 15 seconds. These vapours serve for the sample surface grafting, where so called polymer brush with amines as functional groups were developed for the later antibacterial molecule binding by the intramolecular forces with it.

Samples were separately immersed into prepared vials with solutions of triclosan, and chlorhexidine, and kept standing in shaker at low rpm for 24 hours at laboratory conditions. Concentrations of antibacterial solutions were following: 2 % (w/v) triclosan in absolute ethanol, 2 % (w/v) chlorhexidine in

isopropylalcohol 70% (v/v) aq. solution. Finally, the samples were taken out of the solution and cleaned properly by the stream of water followed by 5 min ultrasonication in deionized water to eliminate the unanchored antibacterial agent molecules from the surface. The last cleaning was done by deionized water. Cleaned samples were dried in ambient conditions for 2 hours and then separately placed into desiccator.

5. Results

Following chapters presents results of doctoral thesis' experimental part. For better sake of clarity, results are divided according to used characterization technique. For easier orientation in the text, the samples were numbered as follows:

Table 6 Prepared and characterized (antibacterial) surfaces

Sample	Sample No.
Pristine LDPE	0
Plasma treated	1
Plasma, AA	2
Plasma, AA + Chlorhexidine	3
Plasma, AA + Triclosan	4
Plasma, AMA	5
Plasma, AMA + Chlorhexidine	6
Plasma, AMA + Triclosan	7
Plasma, DMAA	8
Plasma, DMAA + Chlorhexidine	9
Plasma, DMAA + Triclosan	10

5.1 Contact angle measurement

Table 7 Contact angle measurements data of different samples using deionized water (W), ethylene glycol (E), diiodomethane (D) as wetting agents (mean \pm standard deviation)

Sample No.	θ_W [°]	θ_E [°]	θ_D [°]
0	87.06 \pm 8.6	61.88 \pm 3.3	44.32 \pm 7.3
1	63.02 \pm 5.9	28.97 \pm 5.8	37.04 \pm 7.7
2	58.65 \pm 6.9	28.09 \pm 4.3	36.64 \pm 3.9
3	59.98 \pm 6.8	28.30 \pm 8.5	36.52 \pm 9.8
4	66.23 \pm 10.0	32.69 \pm 11.2	34.21 \pm 7.8
5	62.40 \pm 8.8	30.43 \pm 8.8	38.15 \pm 6.7
6	68.62 \pm 9.9	31.23 \pm 9.3	35.24 \pm 12.2
7	68.52 \pm 5.9	40.54 \pm 8.3	29.45 \pm 23.8
8	59.47 \pm 2.8	34.52 \pm 9.0	35.30 \pm 3.8
9	59.65 \pm 10.2	28.02 \pm 22.7	35.06 \pm 2.7
10	73.36 \pm 16.5	47.68 \pm 2.1	37.03 \pm 10.0

Table 7 shows details about the contact angles of deionized water (θ_w) of individual samples. It is obvious that the LDPE film (sample 0) has natural hydrophobic properties, which vary by the plasma treatment of the pure sample, where the increase of the hydrophilicity is observed. Hydrophilicity is then slightly decreased in all samples, which are linked to antibacterial agents (sample 3, 4, 6, 7, 9, and 10), yet is still higher than the pristine one (sample 0). The most significant decrease in hydrophilicity appears in the sample 10. Nonetheless the hydrophilicity of the samples is significantly higher than in the case of untreated/pristine LDPE sample.

Table 8 Surface energy values

Sample No.	γ^- [mJ/m ²]	γ^+ [mJ/m ²]	γ^p [mJ/m ²]	γ^d [mJ/m ²]	γ^{tot} [mJ/m ²]
0	4.74	0.06	1.10	37.37	38.47
1	14.91	0.48	5.35	41.07	46.41
2	20.40	0.25	4.55	41.26	45.80
3	18.64	0.31	4.78	41.32	46.10
4	12.59	0.30	3.87	42.39	46.26
5	16.31	0.39	5.03	40.53	45.56
6	9.32	0.63	4.86	41.92	46.78
7	13.65	0.00	0.08	44.45	44.53
8	22.69	0.01	1.16	41.89	43.05
9	19.01	0.25	4.34	42.00	46.35
10	11.47	0.00	0.27	41.07	41.35

From the resultant surface energy values shown in Table 8, it is clear that the sample 0 has the lowest value of the total surface energy (γ^{tot}), which corresponds with its natural hydrophobicity. The basic nature of the surface is expressed by the donor part exceeding the acceptor one ($\gamma^- > \gamma^+$). The surface treated by the plasma discharge (sample 1) increases its γ^{tot} , which corresponds with its higher hydrophilicity (see Table 7).

The significant increase of the polar component (γ^p) can be noted in the plasma treated sample (sample 1), which is caused by the incorporation of the artificial polar function groups containing the oxygen. In case of the sample 3 and 4 and the samples 6 and 7, the significant growth of γ^{tot} occurs in contrast to pristine sample. No outstanding differences are happening in the case of the plasma treated surfaces (except the sample 7, 8, and 10). Unlike other samples, the γ^{tot} decrease

markedly in the sample 10. This state corresponds with a higher contact angle θ_w and thus lower hydrophilicity of the same sample.

5.2 SEM

The image of the pristine sample (sample 0) shows relatively smooth and uniform morphology (Figure 20). At higher magnification, the low level of morphology is still apparent. The surface also exhibits some diagonal patterning, which probably arose during manufacturing the LDPE film. After undergoing significant alterations in the plasma reactor, the modification of the surface - corrosion - with the texture of the irregular shape texture is created. This new morphology has an effect on the subsequent coupling processes due to the increase of the surface's roughness.

Next, an image of the plasma treated sample exposed to the AA vapours (sample 2) can be seen. The morphology is similar to the plasma treated one, but more compact. It also cannot be said that there is a significant influence of the surface functionalization onto the total surface morphology. However, the surface with grafted AMA and coupled triclosan (sample 7) has entirely different structure. Here, the evident roughening of the surface after AMA grafting can be seen. This simplifies the consequent bounding of the triclosan, which covers the surface with thin layer.

Almost smooth surface is obtained for the sample, which was treated in the low-temperature plasma, exposed to the DMAA vapours and consequently bounded with chlorhexidine (sample 9). It is obvious that the chlorhexidine layer covers the roughened surface relief, which is hereby smoothed.

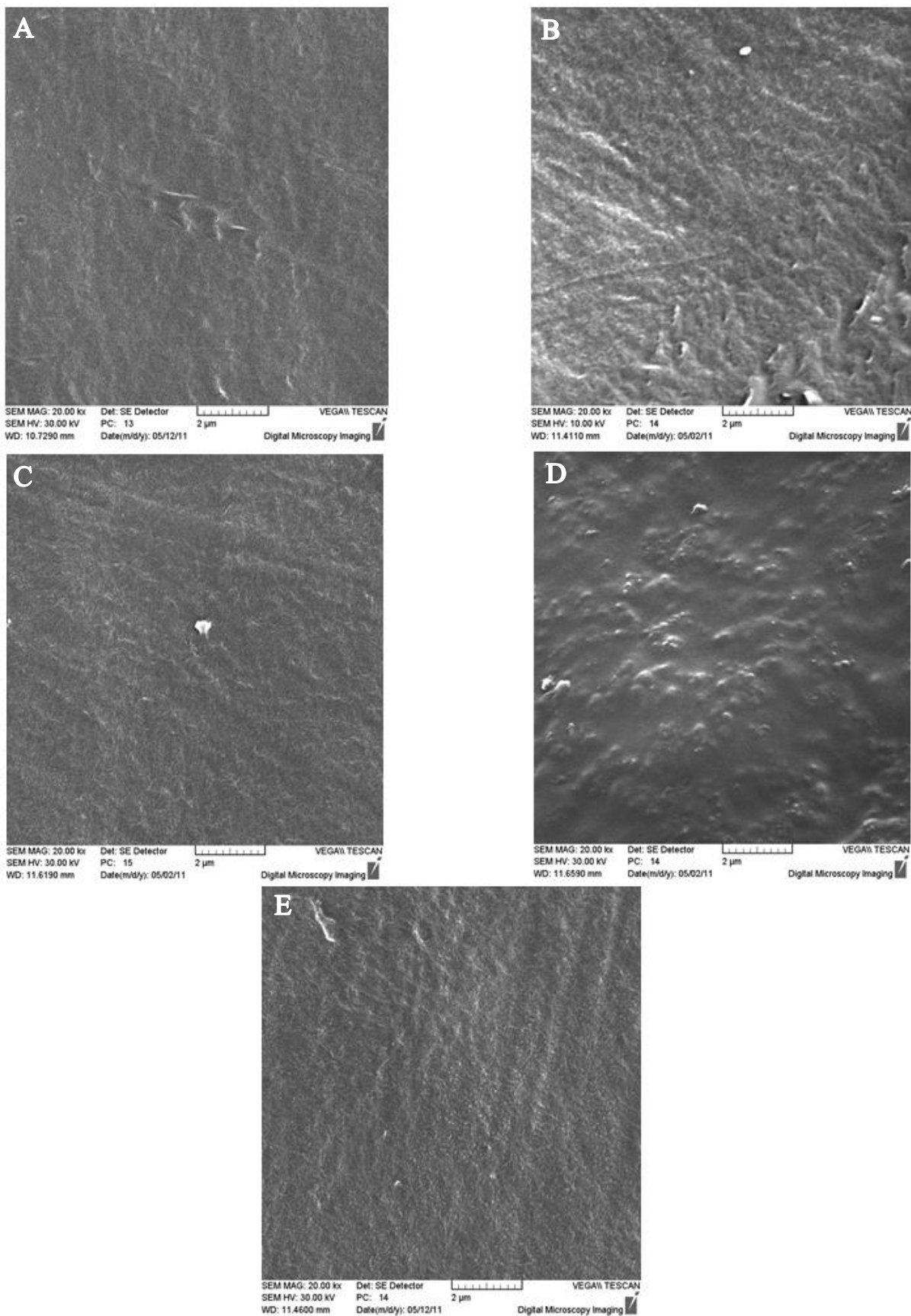


Figure 20 SEM micrographs, A - pristine LDPE (sample 0), B - plasma treated LDPE, (sample 1) C – plasma treated AA grafted LDPE (sample 2), D – plasma treated AMA grafted TC bonded LDPE (sample 7), E – plasma treated DMAA grafted TC anchored LDPE (sample 10)

5.3 ATR-FTIR

Figure 21 shows ATR-FTIR spectroscopy comparison of samples spectra. Results of pure LDPE sample (sample 0) give us typical image of long aliphatic hydrocarbon chain, because of main peaks at wavenumbers: 2915 cm^{-1} and 2847 cm^{-1} (typically assigned to the C-H stretching), 1472 cm^{-1} (belonging to the methylene deformation), 717 cm^{-1} (appurtenant the CH_2 rolling vibration), and $1380 - 1000\text{ cm}^{-1}$ (characteristic for the C-C skeletal vibration). Upon exposure pure sample to plasma discharge it wasn't detected any significant change. A slight increase of peak at 1715 cm^{-1} corresponding to the carbonyl stretch vibration and 1630 cm^{-1} indicating presence of the double bond stretching should be taken into considerations. These facts agree with literature describing polymer surface processing by air plasma treatment.

Samples functionalized by three monomers (sample 2, 5, and 8) gave us spectra slightly indicating presence of amine at wavenumber 3050 cm^{-1} (assigned to the N-H stretching vibration). Furthermore, analysis of surface covered by DMAA (sample 8) after plasma treatment revealed small peak at 1600 cm^{-1} which means bending vibration of the N-H groups. Presences of the amine suggest successful formation of polymer brushes on the substrate surfaces.

Changes after covering samples by antibacterial agents were hardly detectable (general graph in Figure 22 & 23). Peaks in the area $1510 - 1630\text{ cm}^{-1}$ indicate presence of aromatic rings due to their stretching vibration. A wide low peak arose in this area for samples treated by AA, AMA and DMAA and covered by antibacterials (samples 3, 4, 6, 7, 9, and 10). Their intensity is changing. The intensity of its signal slightly increase in a sequence AA, AMA and DMAA (samples 4, 7, and 10) in case of samples covered by the triclosan, and AA, DMAA and AMA (the highest) in case of the chlorhexidine as antibacterial agent (samples 3, 6, and 9). Presence of peaks in this region could also mean the presence of the C=N stretch vibration in the chlorhexidine molecule. Quality of signal at the end part of the spectra is not satisfied to check peaks corresponding to the C-Cl stretching occurring in both antibacterial molecules, which is expected in the range from 600 cm^{-1} to 800 cm^{-1} . However, FTIR spectroscopy results signalize bonding of antibacterial agents on the functionalized surface without any information about the character of that bond.

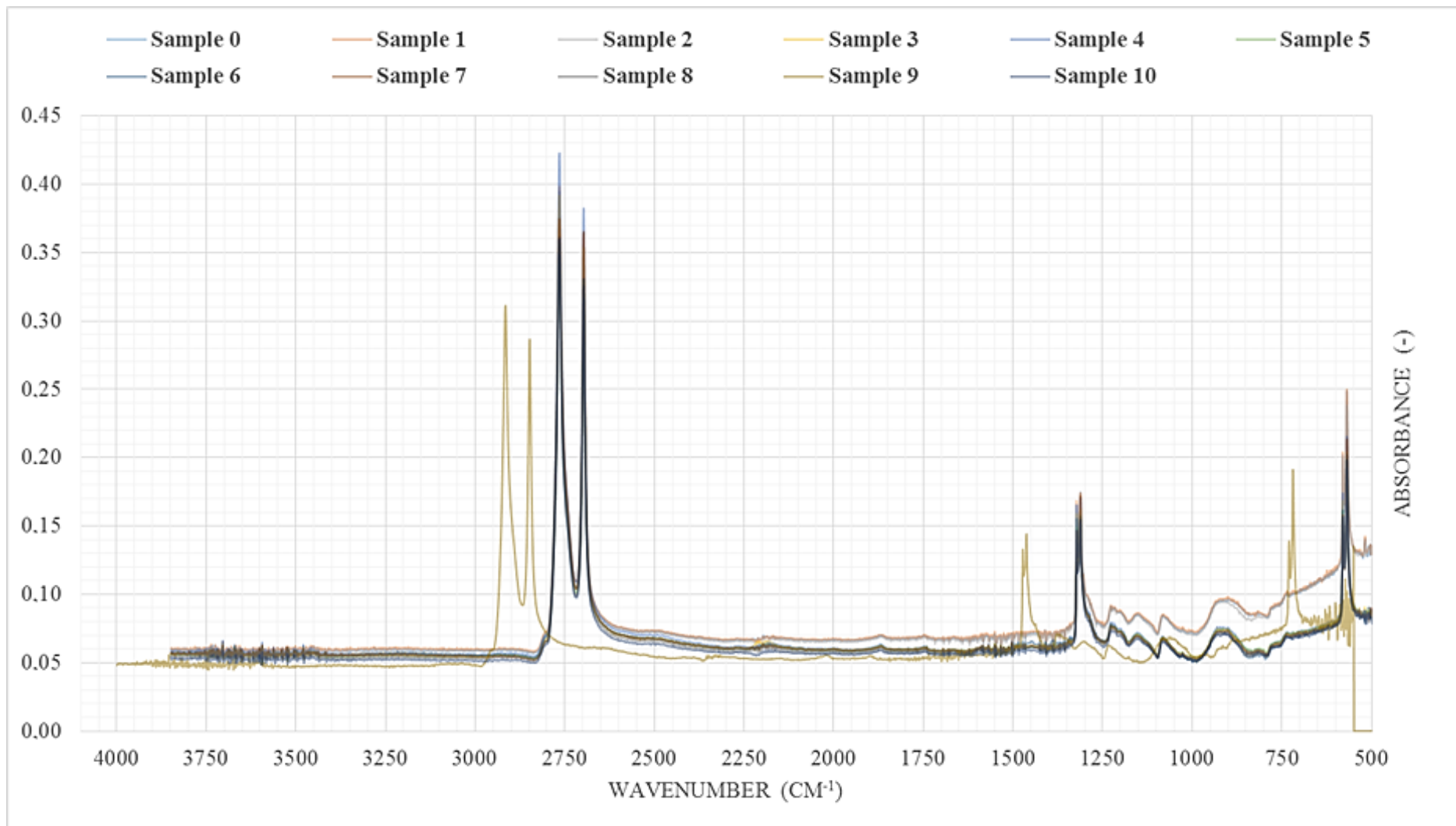


Figure 21 Comparison of all ATR-FTIR spectroscopy spectra

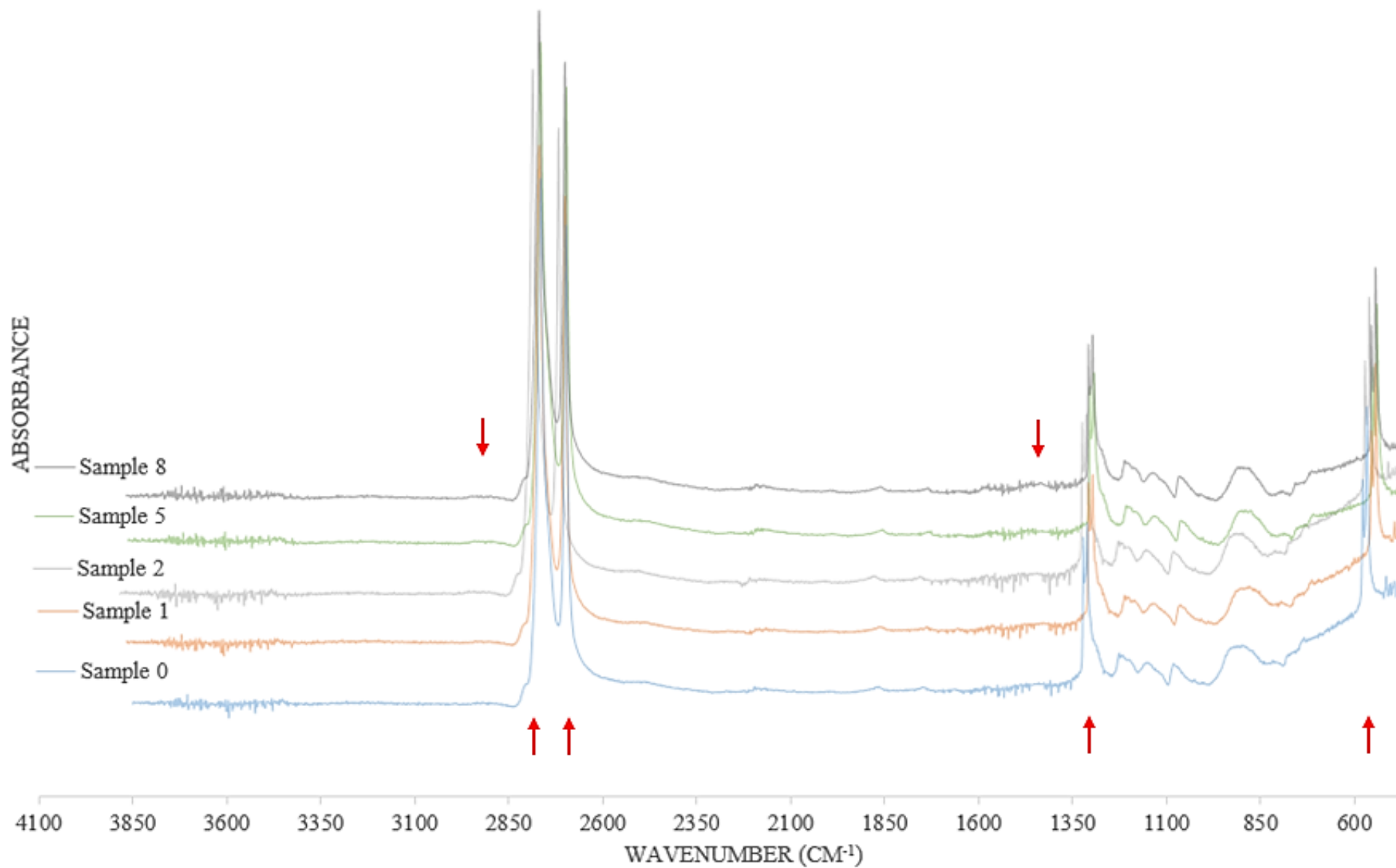


Figure 22 General graph of ATR-FTIR spectroscopy samples after plasma treatment with bonded monomers

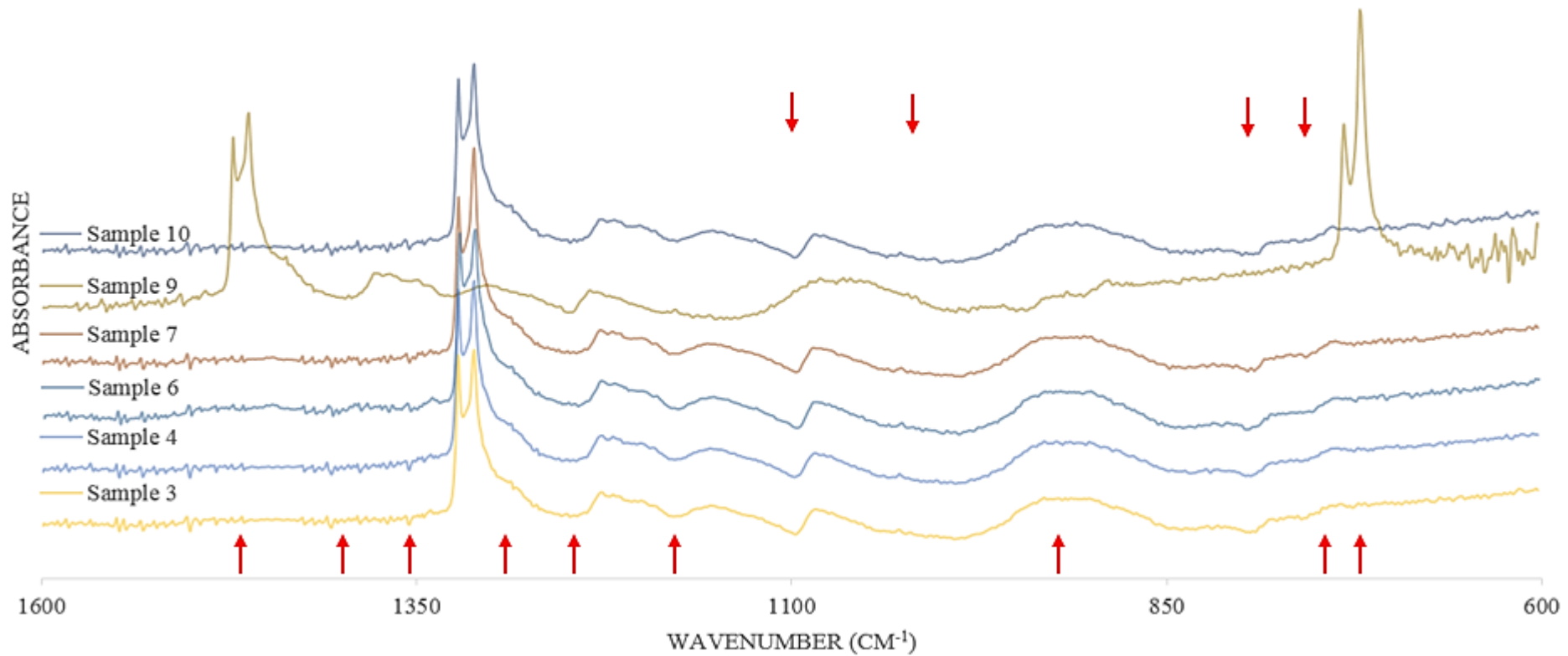


Figure 23 General graph of ATR-FTIR spectroscopy samples after plasma treatment with bonded monomers and antibacterials

5.4 XPS

All results are shown in the Table 9 as a surface element composition and elemental ratios percentage. When we focus on composition of samples grafted by AA, AMA and DMAA (samples 2, 5, and 8), we can indicate following changes. AMA and DMAA grafted samples (sample 5 and 8) compared to the AA grafted (sample 2) showed 1.2 % resp. 2.2 % increase of C1s elements. The content of the oxygen decreased of 0.7 % and 1.2 % respectively their O/C ration values were 0.0930 and 0.0785. Values of the nitrogen showed small decimal decrease in order AA (3.9 %, 0.0448 N/C ratio resp.; sample 2), AMA (3.6 %, 0.0408 N/C ratio resp.; sample 5) and DMAA (3.4 %, 0.0381 N/C ratio resp.; sample 8) grafted samples.

This progress denoted presence of all three grafting agents on the surface because composition of monomers AA, AMA and DMAA (sample 2, 5, and 8) differs from one or two nitrogen bonded methyl groups. The more methyl group in the grafting agent is, the more content of the C1s element and less of the O1s together with the N1s element is detected. These results are in agreement with the FTIR spectroscopy.

Table 9 Surface elemental compositions and ratios of samples

Sample No.	C 1s [%]	O 1s [%]	N 1s [%]	Cl 2p [%]	O/C	N/C	Cl/C
0	98.8	1.2	-	-	0.0121	-	-
1	86.8	12.1	1.1	-	0.1394	0.0127	-
2	87.0	8.9	3.9	-	0.1023	0.0448	-
3	84.5	7.1	6.4	2.0	0.0840	0.0757	0.0237
4	84.6	12.0	0.7	2.7	0.1418	0.0083	0.0319
5	88.2	8.2	3.6	-	0.0930	0.0408	-
6	83.9	6.4	5.8	3.9	0.0763	0.0691	0.0465
7	82.2	13.2	0.5	4.1	0.1606	0.0061	0.0499
8	89.2	7.0	3.4	-	0.0785	0.0381	-
9	84.1	6.4	5.7	3.8	0.0761	0.0678	0.0452
10	82.0	13.3	0.5	4.2	0.1622	0.0061	0.0512

Immobilization of antibacterial agents was well detectable by the XPS contrary to the FTIR analysis. Samples treated by AA and covered by chlorhexidine (sample 3) and triclosan (sample 4) showed similar composition. There are 2.5 % decrease in content of the carbon, noticeable presence of the chlorine (0.0237 and

0.0319 Cl/C ratios) in both samples, decrease of almost 2 % in content of the O1s element and $1.5 \times$ increase in the N/C ratio for sample with chlorhexidine (sample 3) and 3 % increase of oxygen groups, reduction of 90 % N1s groups (to the level 0.0083 N/C ratio) for triclosan covered sample (sample 4), compared to AA grafted sample (sample 2). Compared to that, slightly changed results were detected for samples grafted by AMA and DMAA and treated by chlorhexidine and triclosan (samples 6, 7, 9, 10). Molecules of triclosan includes the Cl and the OH group, which are detectable in more percent in spectra of sample grafted with AMA (amount of the chlorine group is almost 1.5 times higher and the rate of O/C elements increased of one tenth to 0.1606) then amount in the AA grafted and triclosan covered samples (sample 4). Sample grafted by DMAA (sample 8) showed more than one percentage growth of the oxygen concentration (the O/C rate is 0.1622) and the signal refers to the chlorine increased almost 2 times when grafted by the AA (sample 2). Even the chlorhexidine should be well detected according its nitrogen and chlorine groups in the structure. The chlorine group concentration is nearly 2 times more observable at AMA (sample 5) then AA sample (sample 2) covered by the chlorhexidine (its C/Cl rate grown from 0.0237 to 0.0465). Amount of the nitrogen group decrease by 0.5 % at same samples. It can be explained by two effects: covering the surface by the chlorhexidine together with overlapping amino groups of poly-AMA molecules. Even Sample grafted by the DMAA with chlorhexidine (sample 9) revealed almost identical behaviour as AMA grafted (sample 5) compared to AA with the chlorhexidine (sample 3).

This results give us certainty to suggest that all of grafted polymers are attached to the plasma treated surface and antibacterial agents are immobilized on the grafted surface more (in case of the chlorhexidine almost two times, in case of the triclosan $1.5 \times$ according to the C/Cl rate growth), when the AMA or the ADA grafting agent is used.

5.5 Antibacterial activity

The inhibition zones are shown in the Table 10. Due to the disc diameter 8 mm, the size 0.00 is written for all samples, where no inhibition occurs. This is because a possibility that the antibacterial substances act only in direct contact with the sample, and therefore the actual size of the diffusion zone is unknown, exists.

The assumption is that the sample shows antibacterial abilities when the inhibition zone is minimally 12 mm. Under this assumption, the pristine samples, samples with plasma treatment and the samples with AA, AMA and DMAA (samples 0, 1, 2, 5, 8) do not exhibit antibacterial powers against the *E. coli* and *S. aureus*. Although the discs with AA and chlorhexidine (sample 3) and with the DMAA and chlorhexidine (sample 9) create the diffusion zone, these are unfortunately under the limit for the evidential antibacterial ability against *E. coli*, and therefore should not be considered entirely conclusive.

Table 10 Inhibition zone area measurement after 24 hours

<i>Escherichia coli</i> Sample No.	Average inhibition zone [mm]			Average surface [mm ²]
	1.	2.	3.	
0	8.0	8.0	8.0	0.0
1	8.0	8.0	8.0	0.0
2	8.0	8.4	10.2	62.5
3	8.0	10.0	8.6	62.3
4	18.2	16.2	16.6	227.6
5	9.8	8.0	10.4	70.2
6	19.4	19.6	18.0	283.9
7	19.4	18.4	18.8	279.7
8	8.0	8.0	8.0	0.0
9	11.8	9.2	14.8	116.0
10	18.0	18.4	19.8	276.1
<i>Staphylococcus aureus</i> Sample No.				
0	8.0	8.0	8.0	0.0
1	8.0	8.0	8.0	0.0
2	11.4	14.6	8.4	108.3
3	11.0	11.0	13.8	113.2
4	21.2	22.6	31.4	509.5
5	8.0	8.0	8.0	0.0
6	26.8	19.4	26.6	471.8
7	28.4	34.0	36.4	860.7
8	8.0	8.6	8.0	52.9
9	23.4	21.0	23.4	402.2
10	35.0	32.2	34.0	894.8

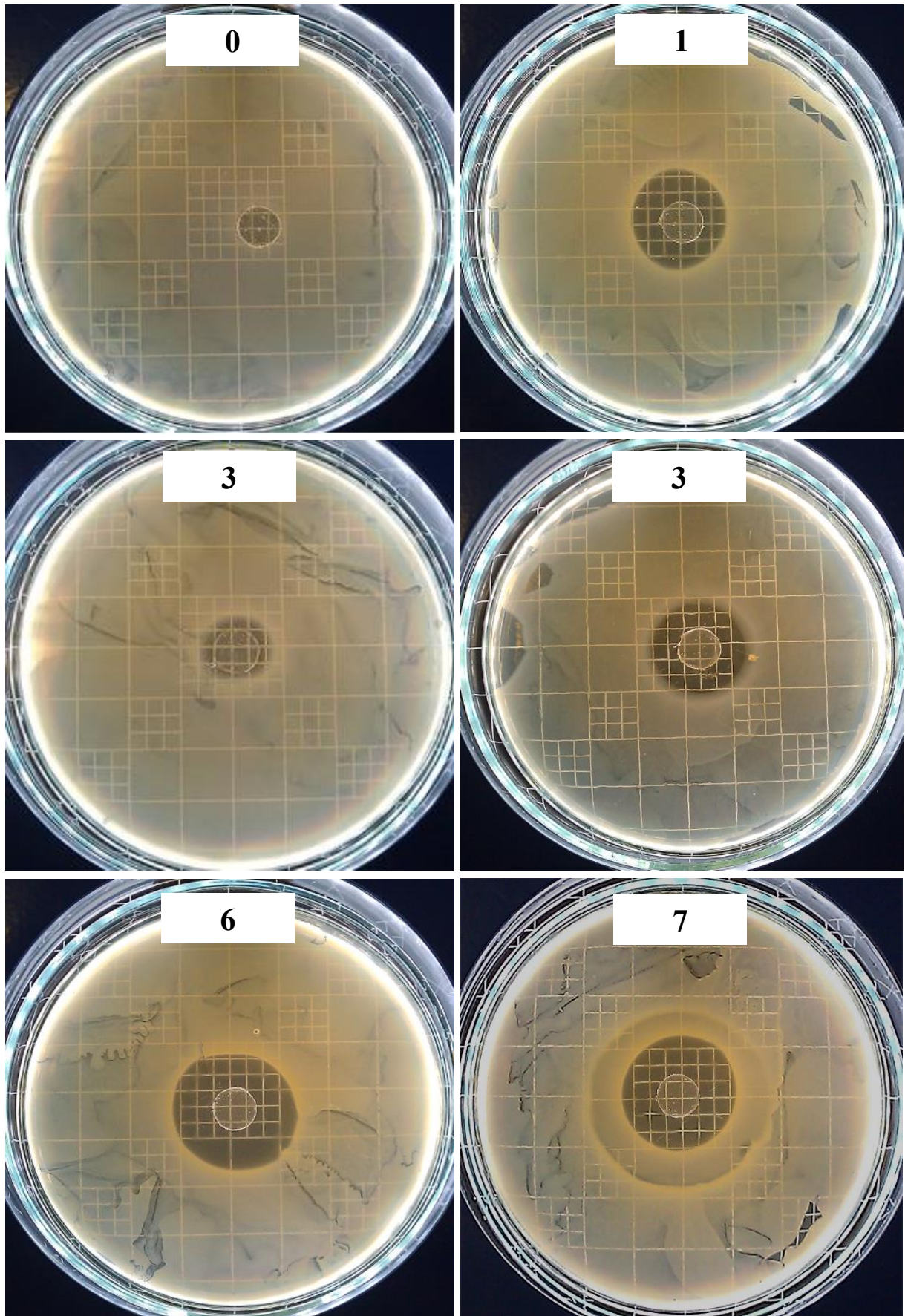


Figure 24 Example of antibacterial tests after 24 hours (left column: performed after manufacturing the materials, right column: 24 hour antibacterial activity performance after 6 months stocking)

Discs with AA and chlorhexidine (sample 3) do not establish sufficiently large diffusion zones in two out of five cases; however the third case shows satisfactory evidence of effectivity against *S. aureus*. This is due to the fact that some discs with the antibacterial agents have developed non-uniform zones of inhibition. In most cases, the required minimal diameter of the inhibition zone is achieved, although it is not projected into the overall average.

As the most effective antibacterial samples for the *E. coli* bacteria, the samples with AMA and triclosan or chlorhexidine (samples 6, 7) and the samples with DMAA and triclosan (sample 10) are identified. The most effective surface against the *S. aureus* bacteria documented the AMA with triclosan or chlorhexidine (samples 6, 7), whereas the DMAA and triclosan samples (sample 10) prove one of the best results. These very satisfactory results can be credited primarily to the functional groups of selected reactants used for the surface functionalisation (AMA and DMAA), to which the antibacterial agents incorporated better by the intermolecular powers.

As can be seen Table 10, the average surfaces are calculated in the homonymic column with the surfaces of the antibacterial discs. The most effective sample against the *S. aureus* is the one with the DMAA and triclosan (sample 10), which is larger by 68.3 % than the DMAA and chlorhexidine (sample 9). If compared to another samples with triclosan, the DMAA (sample 10) is larger by 4.3 % than the AMA (sample 7) and by 45.6 % than the AA sample (sample 4). The most effective sample against the *E. coli* is the AMA and chlorhexidine (sample 6), which is larger by 1.8 % than the AMA with triclosan (sample 7). In comparison to other samples with chlorhexidine, the DMAA and chlorhexidine (sample 9) is smaller by 70.6 % and the AA and with chlorhexidine (sample 3) is smaller by 94.9 %.

These antibacterial tests signify presence of antibacterial agents triclosan and chlorhexidine on the grafted surfaces by AA, AMA and DMAA (samples 3, 4, 6, 7, 9, 10). The quantity of the triclosan was significantly higher on surfaces grafted by AMA or DMAA (sample 7, 10) because of the larger inhibition zone area at both bacteria strains. The quantity of the chlorhexidine increased also more after AMA and DMAA (sample 6, 9) grafting then after AA (sample 4), while AMA grafted surface (sample 6) showed 3 times larger inhibition zone then the DMMA one (sample 9) and so that higher amount of the chlorhexidine attached to the surface. Triclosan or chlorhexidine antibacterial agents are more effective against gram-positive strain.

Table 11 Inhibition zone area measurement after 12/24 hours in repetitive test after 6 months

<i>Escherichia coli</i> Sample No.	Average inhibition zone [mm] 12/24 hrs.			Average surface [mm ²] 12/24 hrs.
	1.	2.	3.	
0	8.0/8.0	8.0/8.0	8.0/8.0	0.0/0.0
1	8.0/8.0	8.0/8.0	8.0/8.0	0.0/0.0
2	8.0/8.0	8.0/8.0	8.0/8.0	0.0/0.0
3	11.2/8.0	12.6/8.0	12.4/8.0	114.7/0.0
4	8.4/8.3	10.3/10.3	8.3/8.3	64.3/63.8
5	8.0/8.0	8.0/8.0	8.0/8.0	0.0/0.0
6	25.4/25.4	22.3/22.3	23.8/23.7	447.4/446.1
7	24.5/24.5	21.5/21.6	22.8/22.7	400.3/414.2
8	8.0/8.0	8.0/8.0	8.0/8.0	0.0/0.0
9	14.5/8.0	15.7/8.0	19.3/8.0	217.1/0.0
10	20.3/20.4	21.7/21.6	25.6/25.8	402.7/283.9
<i>Staphylococcus aureus</i> Sample No.				
0	15.2/8.0	14.8/8.0	15.4/8.0	179.9/0.0
1	12.0/12.1	11.9/13.1	12.2/11.9	113.7/120.3
2	8.0/8.0	8.0/8.0	8.0/8.0	0.0/0.0
3	14.3/8.0	14.1/11.7	12.4/11.7	145.8/88.4
4	31.2/30.3	33.2/35.1	37.7/42.1	915.5/1026.9
5	8.0/8.0	8.0/8.0	8.0/8.0	0.0/0.0
6	35.4/35.5	39.8/40.4	31.6/30.8	1004.2/1005.6
7	35.6/36.1	32.9/33.6	35.7/32	948.8/904.8
8	8.0/8.0	8.0/8.0	8.0/8.0	0.0/0.0
9	32.5/33.0	29.5/33.7	31.6/32.4	765.8/857.2
10	27.3/37.1	37.6/34.5	32.3/41.6	838.4/1125.0

Table 11 shows results of repetitive agar diffusion test. As can be seen, an interesting result was obtained for most specimens of plasma treated surfaces with anchored functionalization monomers and chlorhexidine. These samples were active for at least first 12 hours of incubation, while after this period the created inhibition zone overgrew again in one case (sample 7 – see Figure 24). In case of samples 0, and 1 substrates without antibacterial compounds showed an antibacterial activity out. This was probably caused by the cross-contamination of the material by antibacterials during cutting samples out. Not only the diffusion tests exhibit gradual release of antibacterial agent, but they also prove their ability to inhibit the bacterial growth after 6 months stocking in laboratory conditions.

The minimum 12 hours of efficiency is in light of the in-hospital care absolutely sufficient.

5.6 Terahertz spectroscopy

Observed signals from THz-TDS and ATR module were, as well as the previously collected spectra from ATR FTIR, low intensity. However, changes in treated materials are visible as can be seen from obtained transmittance and refractive indexes and can differentiate each material. The absorbance and transmittance from the Tera OSCAT and transmission module of TPS Spectra™ are inapplicable due to their very low or negative values caused by the material thickness. Therefore for obtaining the best results, the ATR module in combination with imaging module of TPS Spectra™ was used for studying prepared antibacterial surfaces.

Refractive indices

Table 12 Descriptive statistics of refractive indices (by Tera OSCAT).

Sample (No.)	Mean	SD	Median	Min	Max	SE	Thickness [μm]	SD
0	2.1008	0.0004	2.1280	-1.6330	4.0550	0.0037	95.3	0.0013
1	3.2776	0.0008	3.3040	-3.3570	8.0520	0.0068	83.7	0.0009
2	2.6441	0.0008	2.4690	-2.3790	5.2850	0.0056	87.8	0.0007
3	3.2259	0.0007	3.2300	-3.2360	7.8100	0.0049	84.6	0.0010
4	3.0614	0.0007	2.9890	-2.6750	7.0240	0.0039	96.2	0.0073
5	3.0392	0.0008	2.7720	-3.0020	6.0780	0.0050	88.4	0.0019
6	3.2958	0.0008	3.0370	-2.6660	7.1720	0.0011	99.6	0.0038
7	3.4247	0.0001	3.1190	-3.2190	7.5130	0.0049	84.3	0.0040
8	2.8732	0.0006	2.8880	-2.6360	6.7850	0.0030	99.5	0.0018
9	2.9723	0.0006	3.0020	-2.7860	6.9880	0.0037	95.7	0.0009
10	3.1888	0.0007	3.2170	-3.2990	7.7050	0.0039	87.3	0.0007

Each evaluated surface has its typical range of refractive index values (Table 12). In contrast to pristine LDPE (sample 0), all tested samples show changes in their surfaces, not only in displayed peaks but also in spectra shift (Figure 25). Differences in observations can be seen from the first step of a physicochemical preparation of substrates. Each sample (No. 0, 2, 5, 8) without antibacterial

agents has shifted refractive index value of approx. 0.2 from the previous one in row (0, 2, 5, 8) with increasing trend. The strongest peaks occur at 0.93 THz for each sample and most intensive one belongs to the plasma treated LDPE (sample 0). Around 0.55 THz and 1.39 THz a slight decrease of peaks (No. 5, AMA grafted surface) can be noticed after magnification of the spectra.

In comparison to refractive index values obtained by ATR module (Figure 26), the distinction of each modified material is easier by the classical transmission, as the ATR refractive indices are due to attenuation very similar and an attempt to distinguish between them may be therefore not accurate. On the other hand, ATR module brings insight into composition of material that may be omit during the utilization of classic transmission chamber (module) or other modules.

Refractive indexes from transmittance module on TPS Spectra™ show nearly no changes in modified materials, respectively the issue of very thin material occurred again and affected negatively the experimental results. Therefore, the Tera OSCAT is more suitable for such measurement due to its better performance, even though it is not as convenient for other ones.

Dielectric properties

The terahertz dielectric properties of our polymers were characterized by transmission THz-TDS on TPS Spectra™ in the frequency range extending from 0.6 to 2.7 THz to avoid the noise in the 0 – 0.6 and 2.7 - 4 THz region.

In Figure 27, the real part of dielectric constants of measured samples show a feature that is essentially the square of the dielectric constant, because of small absorptions by the samples. Furthermore, it can be seen that the real dielectric constant is in relatively good agreement with the given value 2.3 according to the ISO/TC 61 Standard. The consistency of the measured data for a given material property suggests that our measurement is exact. The graph also depicts changes in dielectric properties as the material was plasma treated and further grafted with functionalization monomers with consequent bonding of antibacterial agents. These changes are showed in Table 13, where the statistics of the region 0.6 to 2.7 THz is calculated. As a result, measurements in the THz range acquire a new meaning.

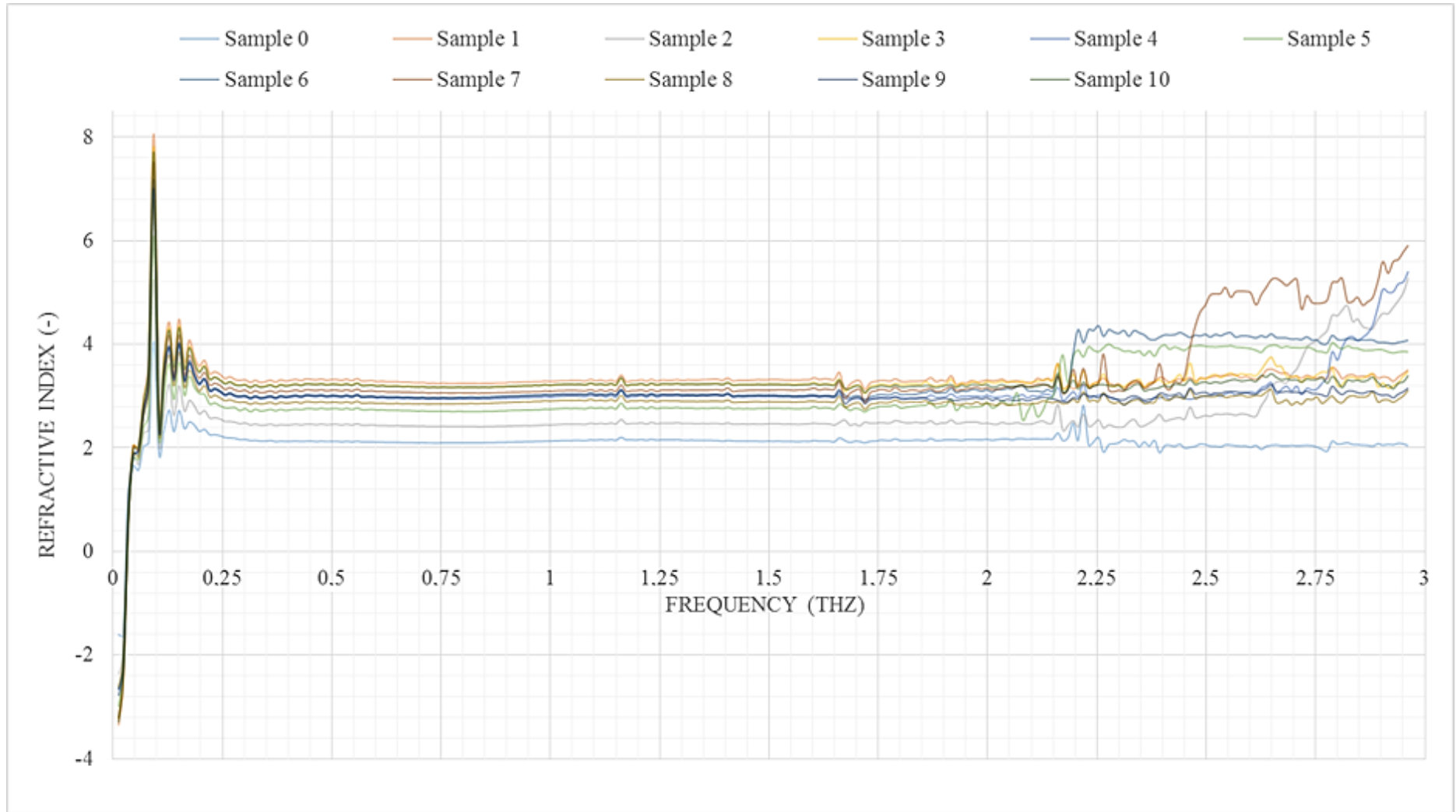


Figure 25 Comparison of refractive indices obtained from Tera OSCAT

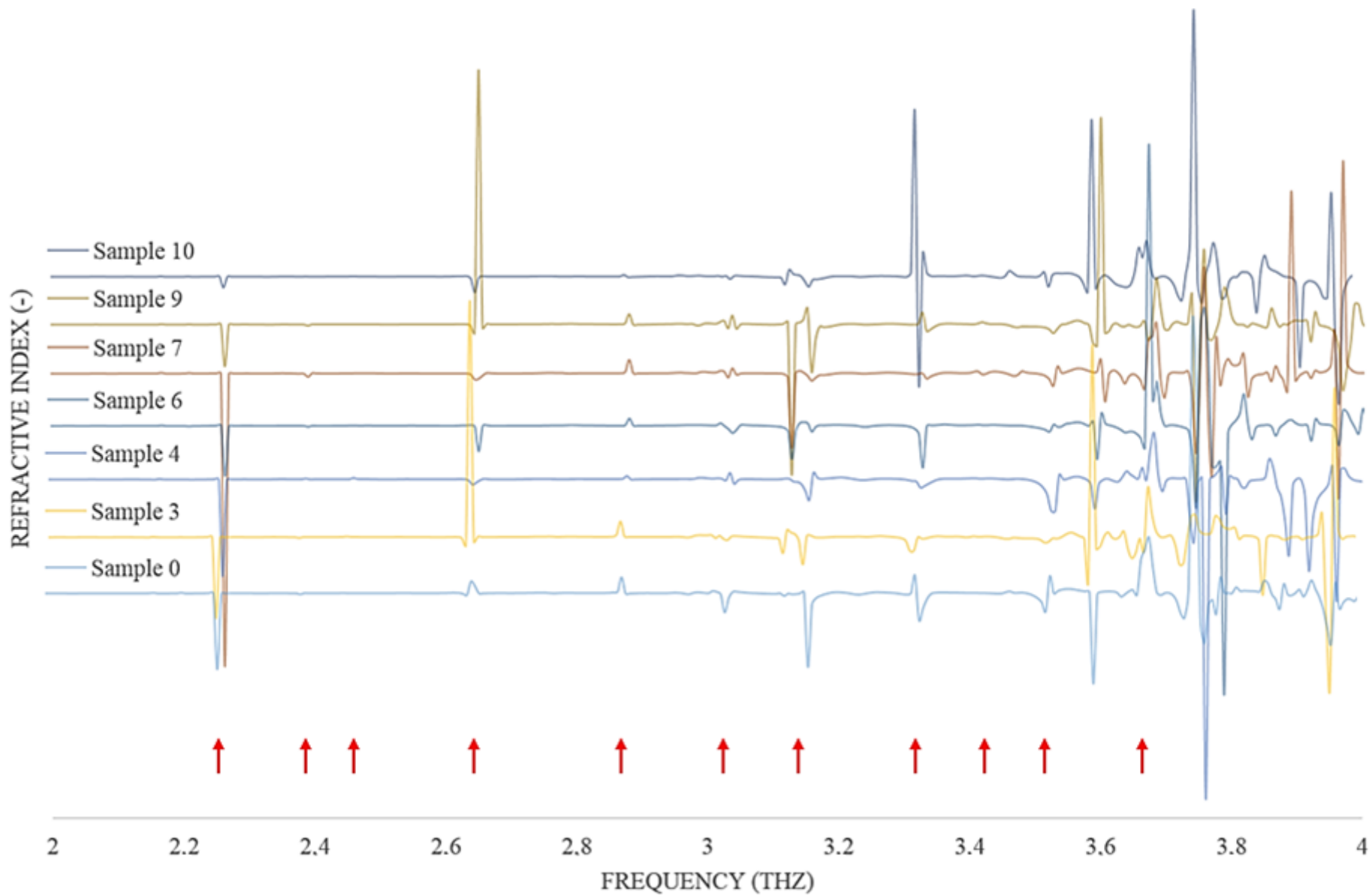


Figure 26 General graph of ATR THz spectroscopy refractive indices for antibacterial samples

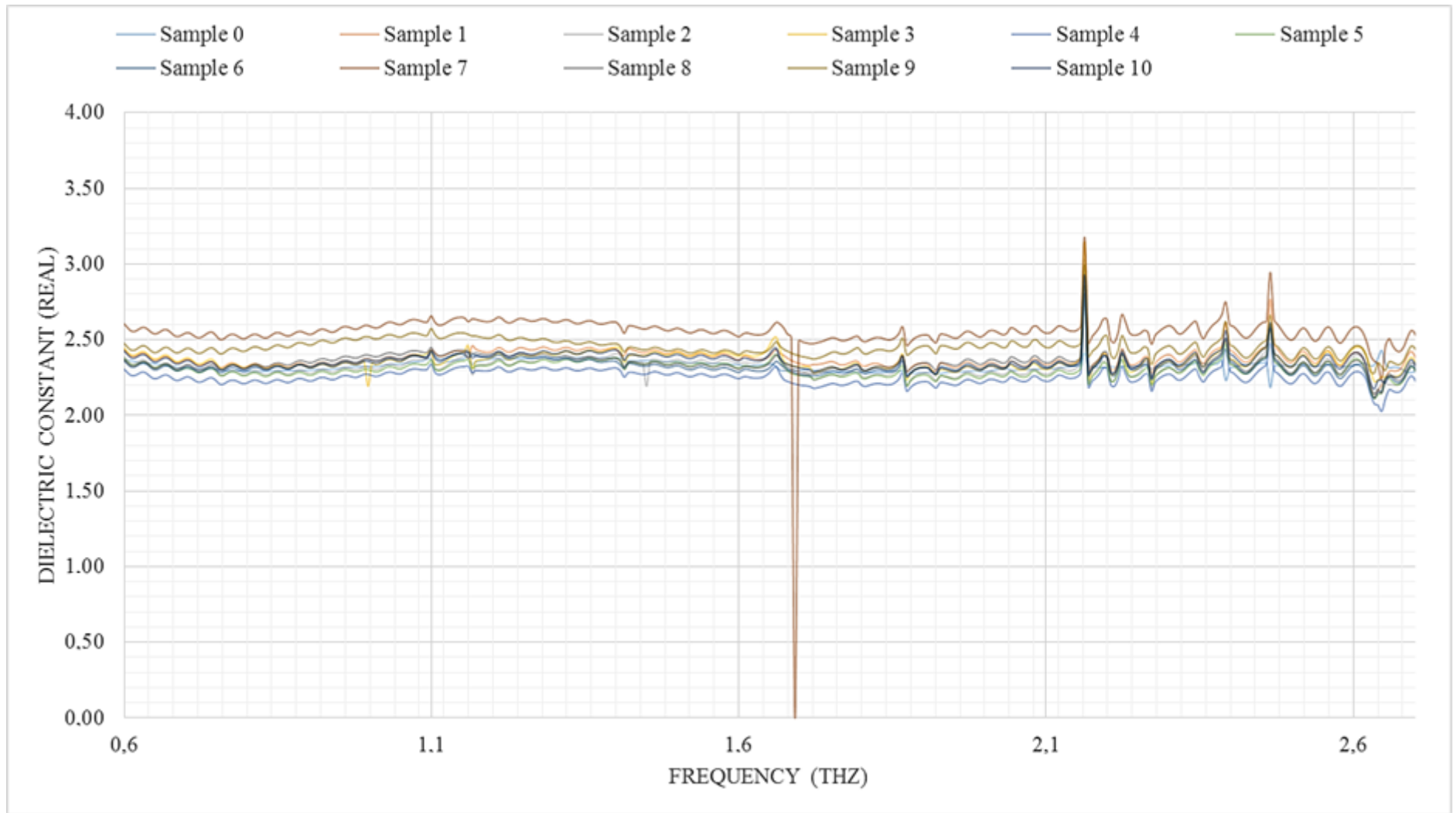


Figure 27 Dielectric constant (real part) of antibacterial surfaces.

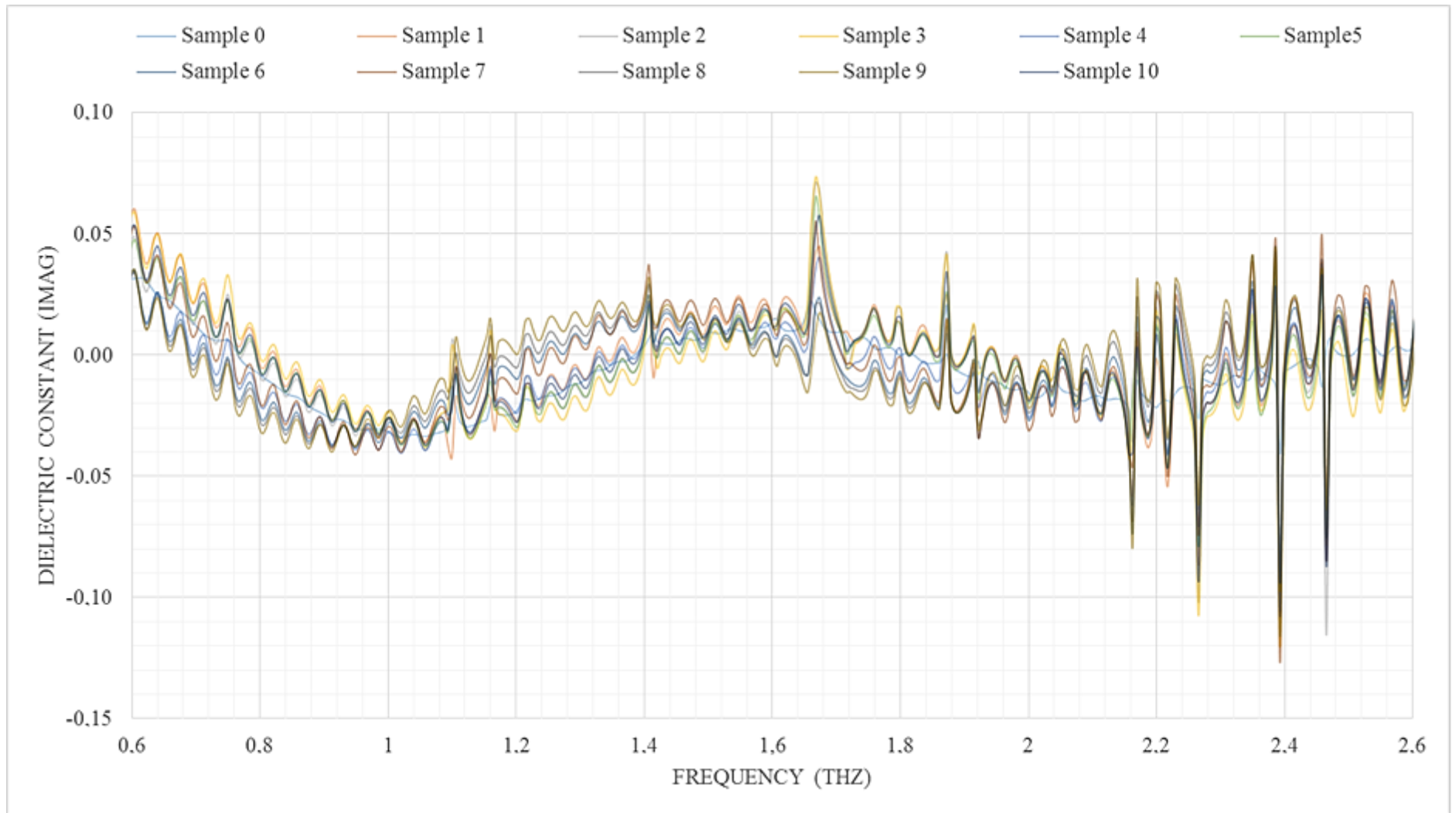


Figure 28 Dielectric constant (imaginary part) of antibacterial surfaces.

Table 13 Descriptive statistics of dielectric properties (ϵ_r).

Sample No.	Mean	SD	Median	Min	Max	SE
0	2.3262	0.0315	2.3258	2.1857	2.4284	0.0005
1	2.3751	0.0592	2.3692	2.1158	2.8544	0.0005
2	2.3599	0.0543	2.3120	2.1443	3.0264	0.0006
3	2.3599	0.0665	2.3527	2.1935	3.1451	0.0006
4	2.2531	0.0543	2.2525	2.0269	2.8001	0.0005
5	2.3257	0.1028	2.3095	2.1024	2.8548	0.0006
6	2.1521	0.3322	2.3109	1.1953	2.8040	0.0005
7	2.5598	0.0660	2.5536	2.2375	3.1761	0.0007
8	2.3487	0.0562	2.3442	2.1411	2.9102	0.0005
9	2.4525	0.0568	2.4470	2.2795	2.9914	0.0006
10	2.3559	0.0572	2.3520	2.1742	2.9260	0.0006

In Figure 27, the real part of dielectric constants of measured samples show a feature that is essentially the square of the dielectric constant, because of small absorptions by the samples. Furthermore, it can be seen that the real dielectric constant is in relatively good agreement with the given value 2.3 according to the ISO/TC 61 Standard. The consistency of the measured data for a given material property suggests that our measurement is exact. The graph also depicts changes in dielectric properties as the material was plasma treated and further grafted with functionalization monomers with consequent bonding of antibacterial agents. These changes are showed in Table 13, where the statistics of the region 0.6 to 2.7 THz is calculated. As a result, measurements in the THz range acquire a new meaning.

Absorbance

Characterization of our surfaces via ATR module on TPS Spectra™ (Figure 29) shows changes in spectrum strength between each material. The first changes that can differentiate each spectrum are in the 0 – 0.2 THz region that is connected with monomers functionalization (biggest peaks for samples No. 6, 10 – AMA with chlorhexidine and DMAA with triclosan) and can be also a signature of the methyl torsion group. A very small peak at 1.7 THz belongs to the N-H vibration, and the same intensity peak appears at 1.9 THz (the C-C vibration). Behaviours in the region of 2 – 4 THz are very good visible.

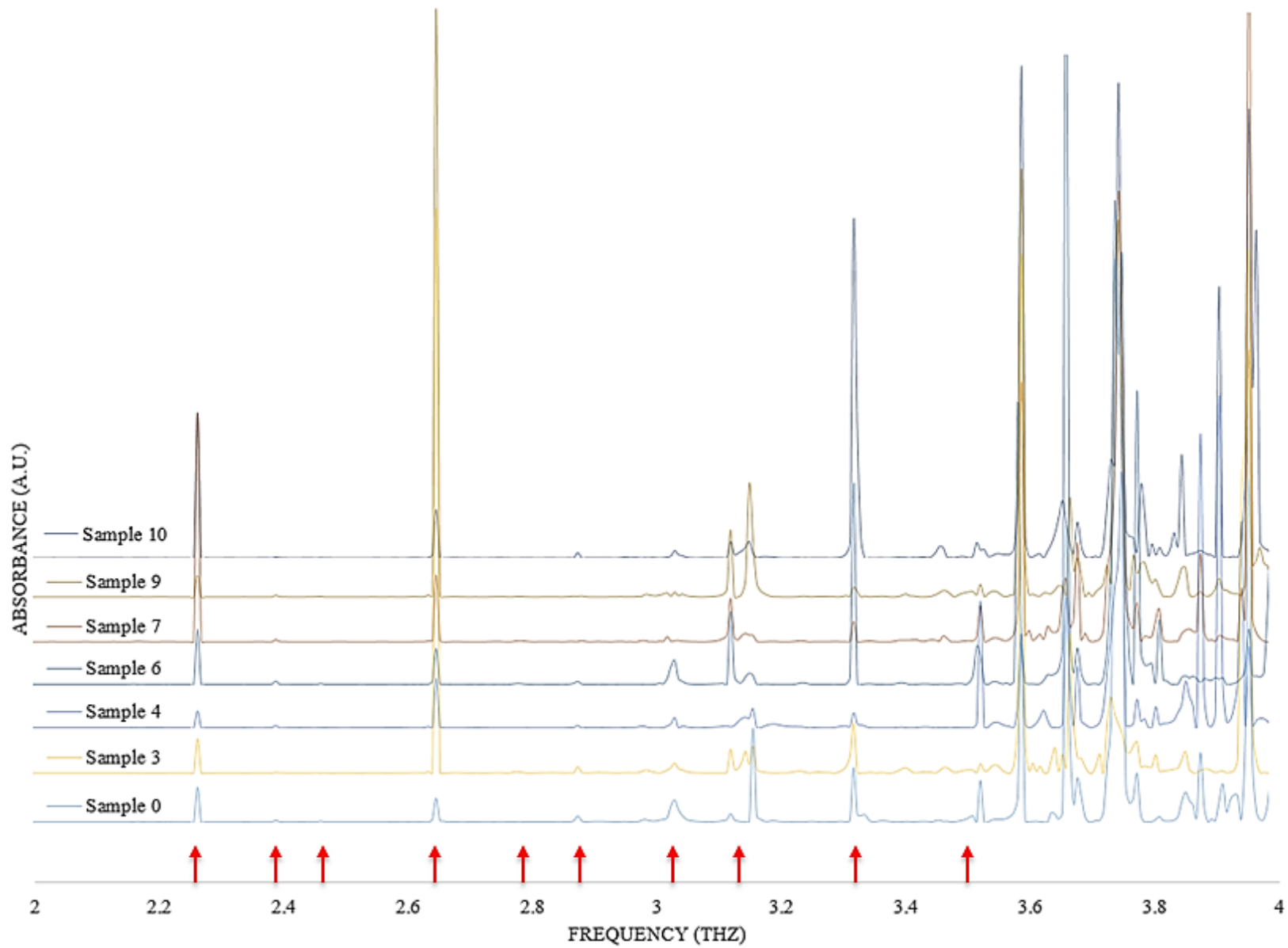


Figure 29 General graph of absorbance spectra – samples with antibacterial compounds

The area including 2, 2.2, 2.4 THz contains bonds with the nitrogen (e.g. the primary/secondary amines). The biggest peak in this area is in the position of 2.3 THz (sample No. 10 – DMAA with triclosan) and belongs to transitions between torsional levels of the CH₃ group (also at around 2.75 THz – sample No. 3). The peak at 2.9 THz match with the vibration of the nitrogen developed during functionalization of prepared surfaces, same as it is for O-H vibrations at 2.5 THz. The space between 3.6 THz and 4 THz is supposed to belong to vibration of bonds with the chlorine and other compounds (e.g. the CH₂, CH, NH₂, aromatic ring), belonging to the antibacterial agents anchored onto functionalized surfaces, which is possible to be detected in this part of spectrum (and proved by the FTIR spectroscopy), and partially the water moisture.

Absorbance spectra from transmittance module of the THz-TDS are very low values with no characteristic lines for prepared material. There are only few minor changes in behaviour for polymers with grafted antibacterial agents Triclosan and Chlorhexidine.

Transmittance

Another set of data belongs to transmittance spectra of materials from the ATR module. As is visible from the Figure 30, each material can be distinguishable from the other well in the region of 0 – 2.7 THz.

Unfortunately, behind the concerned region, the signal noise began to be high. In this case, it is caused by Fabry-Perot interferences of the spectrometer intensified by present water vapours from the air because of non-use of the nitrogen atmosphere. However, the region will not be usable even after employment of special atmosphere or vacuum.

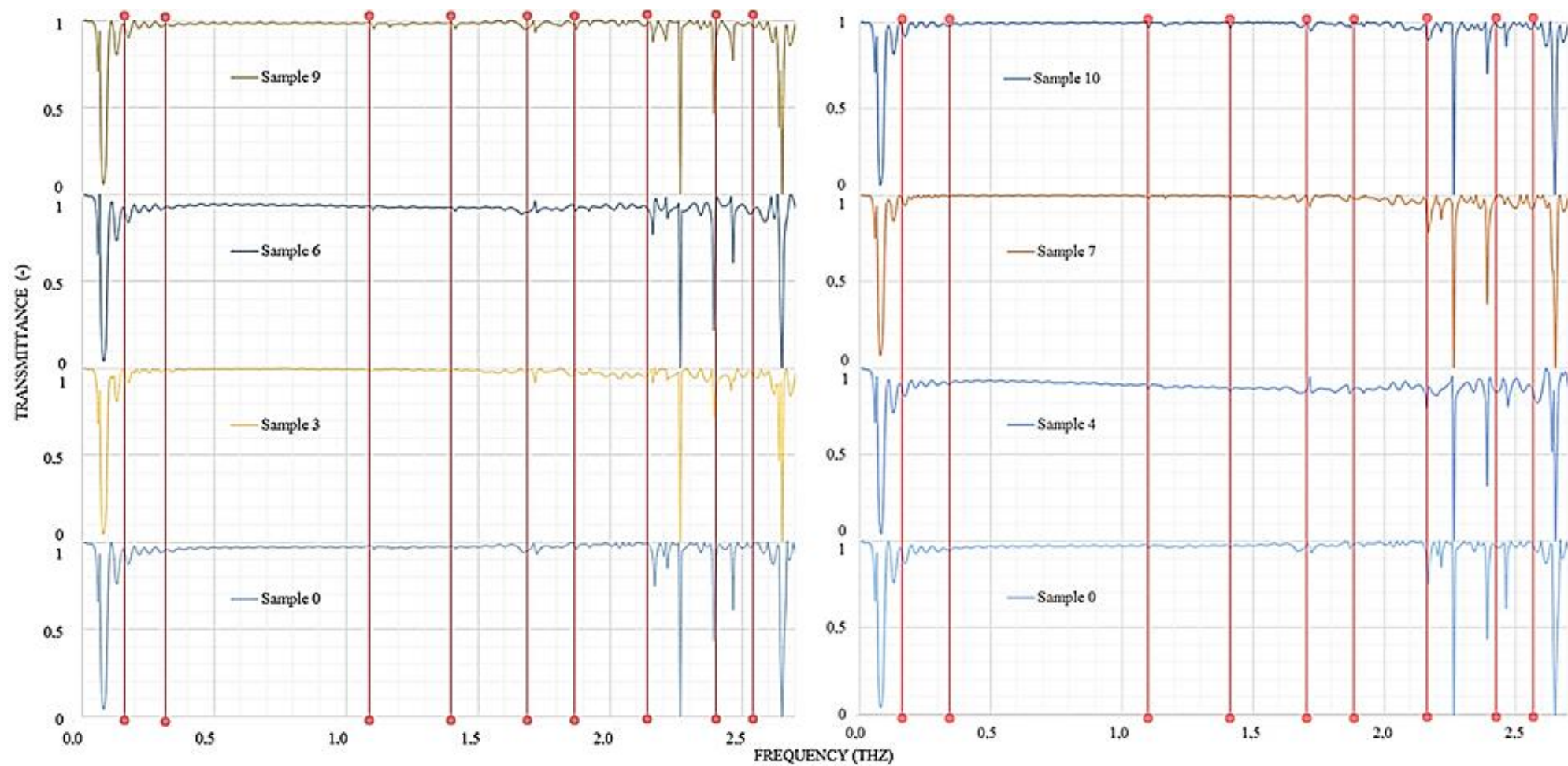


Figure 30 Transmittance of antibacterial surfaces with Triclosan (left) and Chlorhexidine (right) from ATR (TPS Spectra™)

Terahertz imaging

Terahertz imaging module is a useful tool for observing directly the surface of materials, enabling detecting of different cracks, air pockets, layers and other material defects.

According to 3D images obtained from TPS Spectra™ (Figure 31), it can be said that the base LDPE was bonded in the three-step procedure correctly and, as well as images from scanning electron microscopy showed, behaves as one flat surface with antibacterial features. This is supported by 2D images (Figure 32), where the prepared surface of sample 3 (AA and chlorhexidine) is displayed as a monolayer. Contrary to materials prepared within this thesis, materials manufactured by a different project were also subject to THz imaging (Figure 33). During these experiments, chitosan with pectin and glutaraldehyde were bonded onto the polypropylene. In this case, the air pocket is visible and arose probably during final coating of antibacterial layer, resp. this layer is duplex.

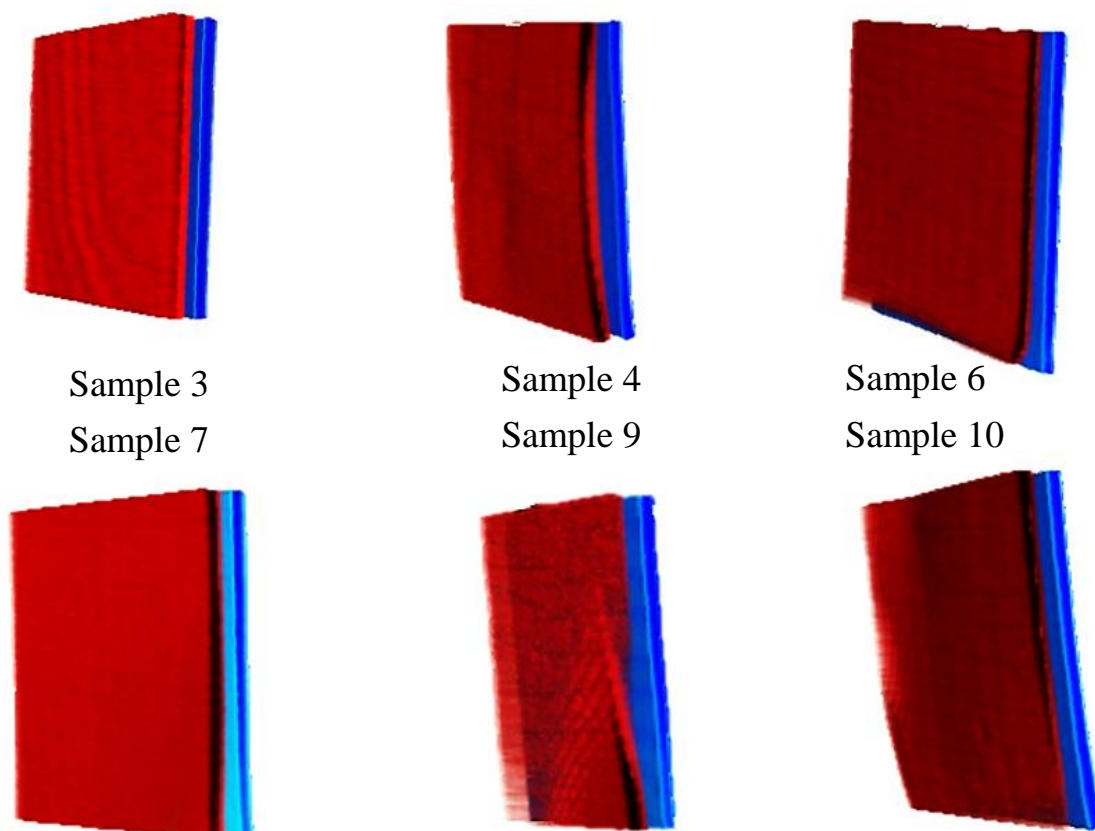


Figure 31 THz 3D imaging examination of antibacterial surface (the red layer is the surface, the blue colour belongs to golden mirror)

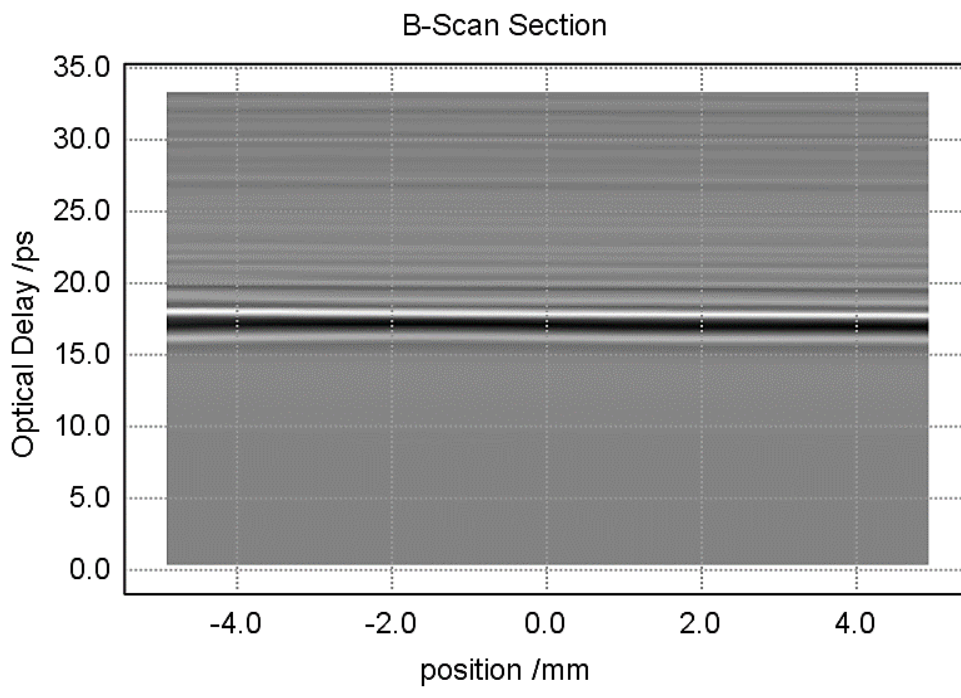


Figure 32 THz 2D imaging examination of antibacterial surface (sample 3) layer thickness

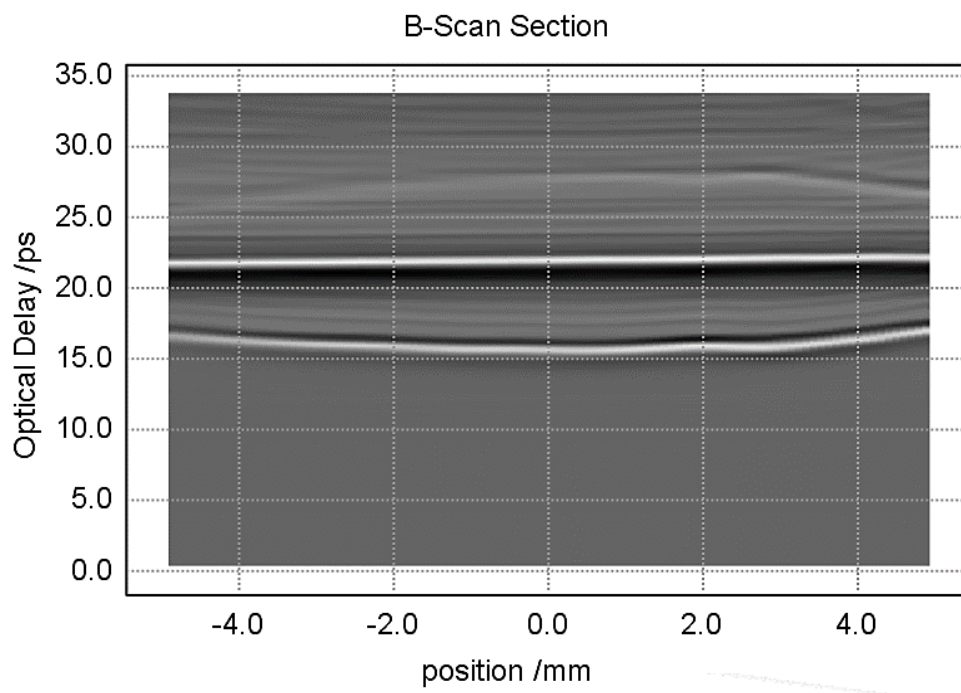


Figure 33 THz 2D & 3D imaging examination of antibacterial surface layer with air pocket

6. Contribution of work

As the most commonly utilized polymer material (LDPE) is used throughout our experiments, the main benefit of this work is a possibility of **practical use** of such materials **in commercial sphere**. Not only the antibacterial surfaces may be used **in food industry** as packaging materials to prolong the shelf-life and protect the food against pathogens, but can be also used **in medicine** as a tool for lowering the risk of inflammation and infection caused by wrongly or insufficiently treated tools, devices and other items.

Furthermore, utilization of the **THz spectroscopy** as a tool for characterization of modified materials is a **first of its kinds** and showed a **great possibility for characterizing and studying features of various materials**. THz spectroscopy is therefore very promising technology that can study not only structure, but e.g. intermolecular bonds as well.

Even though prepared materials with fucoidan and heparin was not successful, utilization of such organic compounds follows **global trends** of developing **materials from renewable resources** or at least **containing natural substances**. Moreover, polymers with combination of anticoagulant and antibacterial agent can provide functional antibacterial film/coating for implants and other applications (e.g. artificial organs) in surgery and tissue therapies.

7. Conclusion

Presented thesis is dealing with preparation and characterization of antibacterial surfaces shows utilization of physicochemical approach to anchor selected antibacterial agents onto pre-activated surfaces based on low density polyethylene. The work itself do not focus only on preparing antibacterial surface, but also to thorough study of prepared material by various techniques, such as FTIR spectroscopy, scanning electron microscopy, agar diffusion test or THz spectroscopy.

All of used techniques showed successful coating of both layers (grafting monomers and chosen agents), the agar diffusion test exhibit satisfactory antibacterial properties of prepared materials. The intermolecular bonding of antibacterial agents was proven not only by the FTIR spectroscopy, where the peaks are very low intensity, or by XPS, but by THz spectroscopy, which is more suitable for this type of bonds that are represented by higher intensity peaks as well. The XPS demonstrates successful bonding of all layers by higher amount of oxygen, nitrogen and chlorine (from the antibacterial compounds), whereas the percent amount of carbon is lowered by the whole multistep process. These results are further supported by outcomes of surface wettability and energy changes. Furthermore, bonding antibacterial compounds intermolecularly formed more effective antibacterial surface than incorporation of these types of compounds into the bulk material (as proved by other research groups e.g. [1]). The antibacterial activity is after 6 month of stocking in laboratory conditions 12 hours, which is satisfactory for use in medicine, as e.g. catheters are changed at regular intervals less than 12 hours; after this time, the materials seems to be only inhibitory.

The novel method for studying modified materials (THz spectroscopy) showed changes in spectra after each step of exploited process for obtaining antibacterial polymers. Where possible, the spectra was assigned to known compounds, as the method and wider range of spectra is still not fully examined and further research is needed. THz imaging proved creation of smooth antibacterial surfaces without defects in topography (these results are supported by data obtained from the scanning electron microscopy). Nevertheless, study performed in this thesis helps lay the foundations for further scientific work in the THz region.

As prepared materials exhibit its active way of functioning (except heparin and fucoidan containing materials), they may be in future used as a prevention against HCAs, as active or smart materials are in constant interest of physicians all over

the world in order to lower the risk of infections and other health issues, which can in the worst scenario lead to patient's death. Therefore, attempts to create the most effective and cheap antibacterial materials and technologies to satisfy increasing demand for such commodities are widely dispersed across the scientific community.

List of references

1. SEDLARIK, Vladimir. *Biodegradation - life of science*. Rolando CHAMY a Francisca ROSENKRANZ. InTech, 2013 Antimicrobial Modification of Polymers. 187-378 s. ISBN 978-953-51-1154-2.
2. RAAD, Issam et al. Improved Antibiotic-Impregnated Catheters with Extended-Spectrum Activity against Resistant Bacteria and Fungi. *Antimicrobial Agents and Chemotherapy*. 2012, vol. 56, no. 2, s. 935-941.
3. PETROVA, O. E. a K. SAUER. A novel signaling network essential for regulating *Pseudomonas aeruginosa* biofilm development. *PLoS Pathogens*. 2009, vol. 5, no. 11, s. e1000668. ISSN 1553-7374; 1553-7366.
4. KIM, Wooseong et al. Spaceflight Promotes Biofilm Formation by *Pseudomonas aeruginosa*. *PLoS ONE*. 2013, vol. 8, no. 4, s. e62437.
5. CHU, P. K. et al. Plasma-surface modification of biomaterials. *Materials Science and Engineering: R: Reports*. 2002, vol. 36, no. 5–6, s. 143-206. ISSN 0927-796X.
6. CHANG, Shih-Hang a Chin-He CHIAN. Plasma surface modification effects on biodegradability and protein adsorption properties of chitosan films. *Applied Surface Science*. 2013, vol. 282, no. 0, s. 735-740. ISSN 0169-4332.
7. BAZAKA, Kateryna et al. Plasma-assisted surface modification of organic biopolymers to prevent bacterial attachment. *Acta Biomaterialia* . 2011, vol. 7, no. 5, s. 2015-2028. ISSN 1742-7061.
8. PANDIYARAJAN, C. K. et al. Influence of the Molecular Structure of Surface-Attached Poly(N-alkyl Acrylamide) Coatings on the Interaction of Surfaces with Proteins, Cells and Blood Platelets. *Macromolecular Bioscience* . 2013, vol. 13, no. 7, s. 873-884. ISSN 1616-5195.
9. CRUZ, Mercedes Cecilia et al. Plasma deposition of silver nanoparticles on ultrafiltration membranes: Antibacterial and anti-biofouling properties. *Chemical Engineering Research and Design*. 2014, no. 0. ISSN 0263-8762.

10. ZHANG, Wei et al. Antibacterial properties of plasma-modified and triclosan or bronopol coated polyethylene. *Polymer*. 2006, vol. 47, no. 3, s. 931-936. ISSN 0032-3861.
11. LEVISON, M. E. Pharmacodynamics of antimicrobial drugs. *Infectious Disease Clinics of North America*. 2004, vol. 18, no. 3, s. 451-65, vii. ISSN 0891-5520; 0891-5520.
12. ZHANG, B. G. et al. Bioactive coatings for orthopaedic implants-recent trends in development of implant coatings. *International Journal of Molecular Sciences*. 2014, vol. 15, no. 7, s. 11878-11921. ISSN 1422-0067; 1422-0067.
13. ATAEFARD, Maryam et al. Investigating the effect of power/time in the wettability of Ar and O₂ gas plasma-treated low-density polyethylene. *Progress in Organic Coatings*. 2009, vol. 64, no. 4, s. 482-488. ISSN 0300-9440.
14. DE GEYTER, N. et al. Treatment of polymer films with a dielectric barrier discharge in air, helium and argon at medium pressure. *Surface and Coatings Technology*. 2007, vol. 201, no. 16–17, s. 7066-7075. ISSN 0257-8972.
15. ZHENG, Jianyun et al. TiN/TiCN multilayer films modified by argon plasma treatment. *Applied Surface Science*. 2013, vol. 280, no. 0, s. 764-771. ISSN 0169-4332.
16. BORCIA G. a N. M. D. Brown. Hydrophobic coatings on selected polymers in an atmospheric pressure dielectric barrier discharge. *Journal of Physics D: Applied Physics*. 2007, vol. 40, no. 7, s. 1927. ISSN 0022-3727.
17. GIL'MAN, A. B. Low-Temperature Plasma Treatment as an Effective Method for Surface Modification of Polymeric Materials. *High Energy Chemistry*. 2003, vol. 37, no. 1, s. 17-23. ISSN 0018-1439.
18. KO, Tze-Man, COOPER, Stuart L. a Paras N. PRASAD. Surface Characterization and Platelet Adhesion Studies of Plasma-Sulfonated Polyethylene. *Frontiers of Polymers and Advanced Materials*. 1994, 439-452 s. ISBN 978-1-4613-6040-7.
19. TITOV, V. A. et al. Kinetic Features of the Formation of Gaseous Products upon Oxygen-Plasma Surface Treatment of Polyethylene,

- Polypropylene, Poly(ethylene terephthalate), and Polyimide Films. *High Energy Chemistry*. 2002, vol. 36, no. 5, s. 354-357. ISSN 0018-1439.
20. DRNOVSKÁ, Hana et al. Surface properties of polyethylene after low-temperature plasma treatment. *Colloid and Polymer Science*. 2003, vol. 281, no. 11, s. 1025-1033. ISSN 0303-402X.
 21. SANCHIS, M. R. et al. Surface modification of low density polyethylene (LDPE) film by low pressure O₂ plasma treatment. *European Polymer Journal*. 2006, vol. 42, no. 7, s. 1558-1568. ISSN 0014-3057.
 22. VAN DEYNSE, A. et al. Surface activation of polyethylene with an argon atmospheric pressure plasma jet: Influence of applied power and flow rate. *Applied Surface Science*. 2015, vol. 328, no. 0, s. 269-278. ISSN 0169-4332.
 23. KARAM, Layal et al. Study of nisin adsorption on plasma-treated polymer surfaces for setting up materials with antibacterial properties. *Reactive and Functional Polymers*. 2013, vol. 73, no. 11, s. 1473-1479. ISSN 1381-5148.
 24. ZHANG, Wei et al. Plasma surface modification of poly vinyl chloride for improvement of antibacterial properties. *Biomaterials*. 2006, vol. 27, no. 1, s. 44-51. ISSN 0142-9612.
 25. YANG, Mu-Rong et al. The antibacterial activities of hydrophilic-modified nonwoven PET. *Materials Science and Engineering: C*. 2002, vol. 20, no. 1-2, s. 167-173. ISSN 0928-4931.
 26. HADJESFANDIARI, Narges et al. Polymer brush-based approaches for the development of infection-resistant surfaces. *Journal of Materials Chemistry B*. 2014, vol. 2, no. 31, s. 4968-4978. ISSN 2050-750X.
 27. SALWICZEK, Mario et al. Emerging rules for effective antimicrobial coatings. *Trends in Biotechnology*. 2014, vol. 32, no. 2, s. 82-90. ISSN 0167-7799.
 28. BÍLEK, František, Táňa KŘÍŽOVÁ a Marián LEHOCKÝ. Preparation of active antibacterial LDPE surface through multistep physicochemical approach: I. Allylamine grafting, attachment of antibacterial agent and antibacterial activity assessment. *Colloids and Surfaces B: Biointerfaces*. 2011, vol. 88, no. 1, s. 440-447. ISSN 0927-7765.

29. POPELKA, Anton et al. A new route for chitosan immobilization onto polyethylene surface. *Carbohydrate Polymers*. 2012, vol. 90, no. 4, s. 1501-1508. ISSN 0144-8617.
30. BÍLEK, František et al. Preparation of active antibacterial LDPE surface through multistep physicochemical approach II: Graft type effect on antibacterial properties. *Colloids and Surfaces B: Biointerfaces*. 2013, vol. 102, s. 842-848.
31. MCDONNELL, G. a A. D. RUSSELL. Antiseptics and disinfectants: activity, action, and resistance. *Clinical Microbiology Reviews*. 1999, vol. 12, no. 1, s. 147-179. ISSN 0893-8512; 0893-8512.
32. WEINSTEIN, Robert A. et al. Chlorhexidine: Expanding the Armamentarium for Infection Control and Prevention. *Clinical Infectious Diseases*. 2008, vol. 46, no. 2, s. 274-281.
33. SOUZA, Carlos A. Soriano de et al. Adsorption of chlorhexidine on synthetic hydroxyapatite and in vitro biological activity. *Colloids and Surfaces B: Biointerfaces*. 2011, vol. 87, no. 2, s. 310-318. ISSN 0927-7765.
34. URBANSKY, Edward Todd a Howard J. BELL. Concerns with chlorhexidine preservatives in refillable portable eyewashes. *Journal of Chemical Health and Safety*. 2013, vol. 20, no. 6, s. 24-34. ISSN 1871-5532.
35. SAAD, S., K. HEWETT a J. GREENMAN. Effect of mouth-rinse formulations on oral malodour processes in tongue-derived perfusion biofilm model. *Journal of Breath Research*. 2012, vol. 6, no. 1, s. 016001-7155/6/1/016001. Epub 2012 Jan 10. ISSN 1752-7163; 1752-7155.
36. ROS-LLOR, Irene a Pia LOPEZ-JORNET. Cytogenetic analysis of oral mucosa cells, induced by chlorhexidine, essential oils in ethanolic solution and triclosan mouthwashes. *Environmental Research*. 2014, vol. 132, no. 0, s. 140-145. ISSN 0013-9351.
37. GRASSI, Tony F. et al. DNA damage in multiple organs after exposure to chlorhexidine in Wistar rats. *International Journal of Hygiene and Environmental Health*. 2007, vol. 210, no. 2, s. 163-167. ISSN 1438-4639.
38. HIDALGO, E. a C. DOMINGUEZ. Mechanisms underlying chlorhexidine-induced cytotoxicity. *Toxicology in Vitro*. 2001, vol. 15, no. 4-5, s. 271-276. ISSN 0887-2333.

39. LI, Y. C. et al. Cytotoxicity and genotoxicity of chlorhexidine on macrophages in vitro. *Environmental Toxicology*. 2014, vol. 29, no. 4, s. 452-458. ISSN 1522-7278; 1520-4081.
40. DYNES, J. J. et al. Quantitative mapping of chlorhexidine in natural river biofilms. *The Science of the Total Environment*. 2006, vol. 369, no. 1-3, s. 369-383. ISSN 0048-9697; 0048-9697.
41. ZONG, Z. a L. E. KIRSCH. Studies on the instability of chlorhexidine, part I: kinetics and mechanisms. *Journal of Pharmaceutical Sciences*. 2012, vol. 101, no. 7, s. 2417-2427. ISSN 1520-6017; 0022-3549.
42. BASS, Pauline et al. Impact of chlorhexidine-impregnated washcloths on reducing incidence of vancomycin-resistant enterococci colonization in hematology–oncology patients. *American Journal of Infection Control*. 2013, vol. 41, no. 4, s. 345-348. ISSN 0196-6553.
43. MACIAS, Juan H. et al. Chlorhexidine is a better antiseptic than povidone iodine and sodium hypochlorite because of its substantive effect. *American Journal of Infection Control*. 2013, vol. 41, no. 7, s. 634-637. ISSN 0196-6553.
44. HUMAR, Atul et al. Prospective randomized trial of 10% povidone-iodine versus 0.5% tincture of chlorhexidine as cutaneous antisepsis for prevention of central venous catheter infection. *Clinical Infectious Diseases*. 2000, roč. 31, č. 4, s. 1001–1007.
45. LOKKEN, P., I. OLSEN a O. SPIGSET. Mouth-rinsing with chlorhexidine for prevention of pneumonia. *Tidsskrift for Den Norske Laegeforening : Tidsskrift for Praktisk Medicin, Ny Raekke*. 2010, vol. 130, no. 18, s. 1828-1829. ISSN 0807-7096; 0029-2001.
46. MILSTONE, A. M., C. L. PASSARETTI a T. M. PERL. Chlorhexidine: expanding the armamentarium for infection control and prevention. *Clinical Infectious Diseases : An Official Publication of the Infectious Diseases Society of America*. 2008, vol. 46, no. 2, s. 274-281. ISSN 1537-6591; 1058-4838.
47. LIM, K. S. a P. C. KAM. Chlorhexidine - pharmacology and clinical applications. *Anaesthesia and Intensive Care*. 2008, vol. 36, no. 4, s. 502-512. ISSN 0310-057X; 0310-057X.

48. MEYER, Todd a Mark SCHALLENBERGER. A Novel Chlorhexidine Hydrogel Coating for Peripheral Venous Catheters. *American Journal of Infection Control*. 2012, vol. 40, no. 5, s. e60. ISSN 0196-6553.
49. European Union, Scientific Committee on Consumer Safety. *Opinion on triclosan (antimicrobial resistance)*. European Union, 2010. 56 s. ISBN 1831-4767 /978-92-79-12484-6.
50. HEATH, R. J. et al. Mechanism of triclosan inhibition of bacterial fatty acid synthesis. *The Journal of Biological Chemistry*. 1999, vol. 274, no. 16, s. 11110-11114. ISSN 0021-9258; 0021-9258.
51. RUSSELL, A. D. Whither triclosan?. *The Journal of Antimicrobial Chemotherapy*. 2004, vol. 53, no. 5, s. 693-695. ISSN 0305-7453; 0305-7453.
52. ZORRILLA, Leah M. et al. The Effects of Triclosan on Puberty and Thyroid Hormones in Male Wistar Rats. *Toxicological Sciences*. 2009, vol. 107, no. 1, s. 56-64.
53. VELDHOEN, N. et al. The bactericidal agent triclosan modulates thyroid hormone-associated gene expression and disrupts postembryonic anuran development. *Aquatic Toxicology (Amsterdam, Netherlands)*. 2006, vol. 80, no. 3, s. 217-227. ISSN 0166-445X; 0166-445X.
54. STOKER, Tammy E., Emily K. GIBSON a Leah M. ZORRILLA. Triclosan Exposure Modulates Estrogen-Dependent Responses in the Female Wistar Rat. *Toxicological Sciences*. 2010, vol. 117, no. 1, s. 45-53.
55. U.S. EPA. *Registration eligibility decision for triclosan, list B, case no. 2340*. Frank T. Sanders Office of Prevention, Pesticides and Toxic Substances (7510P): EPA, 2008. 98 s. Dostupné z: <http://www.epa.gov/oppsrrd1/reregistration/REDS/2340red.pdf>.
56. BHUNIA, A. K., C. R. TAITT a M. S. KIM. *High throughput screening for food safety assessment*. Arun K. BHUNIA, Moon S. KIM a Chris R. TAITT. Woodhead Publishing. 2015. 1 - High throughput screening strategies and technology platforms for detection of pathogens: an introduction. 1-9 s. ISBN 9780857098016.
57. LODINOVÁ-ZÁDNÍKOVÁ, R., B. CUKROWSKA a H. TLASKALOVA-HOGENOVA. Oral administration of probiotic *Escherichia coli* after birth reduces frequency of allergies and repeated

- infections later in life (after 10 and 20 years). *International archives of allergy and immunology* . 2003, roč. 131, č. 3, s. 209–211.
58. GROZDANOV, L. et al. Analysis of the genome structure of the nonpathogenic probiotic *Escherichia coli* strain Nissle 1917. *Journal of Bacteriology*. 2004, vol. 186, no. 16, s. 5432-5441. ISSN 0021-9193; 0021-9193.
 59. KAMADA, Nobuhiko et al. Nonpathogenic *Escherichia coli* Strain Nissle 1917 Prevents Murine Acute and Chronic Colitis. *Inflammatory Bowel Diseases*. 2005, vol. 11, no. 5. ISSN 1078-0998.
 60. YANG, X. a H. WANG. Pathogenic *E. coli* (Introduction). *Encyclopedia of food microbiology (second edition)*. Oxford: Academic Press. 2014, 695-701 s. ISBN 9780123847331.
 61. ROJAS, Fabio, W. Carson BYRD a Sanjay SAINT. Institutional origins of health care–associated infection knowledge: Lessons from an analysis of articles about methicillin-resistant *Staphylococcus aureus* published in leading biomedical journals from 1960-2009. *American Journal of Infection Control*. 2014, no. 0. ISSN 0196-6553.
 62. DRAKE, Philip et al. Raman based detection of *staphylococcus aureus* utilizing single domain antibody coated nanoparticle labels and magnetic trapping. *Analytical Methods*. 2013, 4152 s. ISBN 1759-9660.
 63. DINGES, M. M., P. M. ORWIN a P. M. SCHLIEVERT. Exotoxins of *Staphylococcus aureus*. *Clinical Microbiology Reviews*. 2000, vol. 13, no. 1, s. 16-34, table of contents. ISSN 0893-8512; 0893-8512.
 64. TODD, E. C. D. Bacteria: *Staphylococcus aureus*. *Encyclopedia of food safety*. Yasmine MOTARJEMI. Waltham: Academic Press. 2014, 530-534 s. ISBN 9780123786135.
 65. *The 41st IEEE International Conference on Plasma Science and the 20 th International Conference on High-Power Particle Beams*. IEEE [cit. 05102015]. Dostupné Z: <http://ece-events.unm.edu/icops-beams2014/lowtemp.html>.
 66. FRIDMAN, Alexander. *Plasma Chemistry*. New York: Cambridge University Press, 2008. 1022-xlii s. ISBN 978-0-511-39857-5.
 67. KOGELSCHATZ, Ulrich. Dielectric-Barrier Discharges: Their History, Discharge Physics, and Industrial Applications. *Plasma Chemistry and Plasma Processing*. 2003, vol. 23, no. 1, s. 1-46. ISSN 0272-4324.

68. VALINČIUS, Vitas, GRIGAITIENE, Viktorija a TAMOŠIUNAS, Andrius. *Report on the Different Plasma Modules for Pollution Removal MO 03*. Kaunas: Lithuanian Energy Institute, 2012 [cit. 05102015]. Dostupné z: http://www.plastep.eu/fileadmin/dateien/Outputs/Report_on_the_different_Plasma_Modules_for_Pollution_Removal.pdf.
69. COOLS, Pieter et al. The use of DBD plasma treatment and polymerization for the enhancement of biomedical UHMWPE. *Thin Solid Films*. 2014, vol. 572, no. 0, s. 251-259. ISSN 0040-6090.
70. GEDALIN, Michael. *Lecture notes in physics - introduction to plasma physics*. Lecture Notes, Department of Physics, Ben-Gurion University Israel: 2013. 77 s. Dostupné z: <http://physweb.bgu.ac.il/COURSES/PlasmaGedalin/introplasma.pdf>
71. LEE, Yun-Shik. *Principles of Terahertz Science and Technology*. Springer US, 2009. XII, 340 s. ISBN 978-0-378-09539-4.
72. BRÜDERMANN, Erik, Heinz-Wilhelm HÜBERS a Maurice F. KIMMITT. *Terahertz Techniques*. Springer-Verlag Berlin Heidelberg, 2012. XXII, 386 s. ISBN 978-3-642-02591-4. Springer Series in Optical Sciences, Vol. 151.
73. SHEN, Yao-Chun. Terahertz pulsed spectroscopy and imaging for pharmaceutical applications: A review. *International Journal of Pharmaceutics*. 2011, vol. 417, no. 1–2, s. 48-60. ISSN 0378-5173.
74. PAUL, Douglas J. *Terahertz Research*. University of Glasgow, Semiconductor Device Group. 2014 [cit. 05102015]. Dostupné z: <http://userweb.eng.gla.ac.uk/douglas.paul/terahertz.html>.
75. YIN, X., B. W. H. NG a D. ABBOTT. *Terahertz Imaging for Biomedical Applications: Pattern Recognition and Tomographic Reconstruction*. Springer New York, 2012. ISBN 9781461418207.
76. PEIPONEN, Kai-Erik, Axel ZEITLER a Makoto KUWATA-GONOKAMI. *Terahertz Spectroscopy and Imaging*. Springer-Verlag Berlin Heidelberg, 2013. 644-XXXII s. ISBN 978-3-642-43904-9. Springer Series in Optical Sciences, Vol. 171.
77. JEPSEN, P. U., D. G. COOKE a M. KOCH. Terahertz spectroscopy and imaging. Modern techniques and applications. *Laser & Photonics Reviews*. 2011, vol. 5, no. 1, s. 124-166. ISSN 1863-8899.

78. ABBOTT, D. a X. -C ZHANG. Special Issue on T-Ray Imaging, Sensing, and Retection. *Proceedings of the IEEE*. 2007, vol. 95, no. 8, s. 1509-1513. ISSN 0018-9219.
79. SULOVSKÁ, Kateřina a Marián LEHOCKÝ. Characterization of plasma treated surfaces for food safety by terahertz spectroscopy. *Proc. SPIE 9252, Millimetre Wave and Terahertz Sensors and Technology VII*. 2014. 9252-09 s.
80. CHAN, Wai Lam, Jason DEIBEL a Daniel M. MITTLEMAN. Imaging with terahertz radiation. *Report on Progress in Physics*. 2007, vol. 70, s. 1325.
81. SAEEDKIA, D. *Handbook of terahertz technology for imaging, sensing and communications*. Elsevier Science. ISBN 9780857096494.
82. ZHANG, Q. et al. Terahertz pulsed imaging and magnetic resonance imaging as tools to probe formulation stability. *Pharmaceutics*. 2013, vol. 5, no. 4, s. 591-608. ISSN 1999-4923; 1999-4923.
83. STUART, Barbara. *Infrared Spectroscopy: Fundamentals and Applications*. Wiley, 2004. viii - 207 s. ISBN 0-470-86427-8.
84. CU, Boulder. *Infrared spectroscopy: Theory*. Online edition for students of organic chemistry lab courses at University of Colorado, Boulder, Dept of Chem. and Biochem. 2002. 10 s. Dostupné z: <http://orgchem.colorado.edu/Spectroscopy/irtutor/IRtheory.pdf>
85. Thermo Nicolet Corporation. *Introduction to Fourier Transform Infrared Spectrometry*. Madison, WI, USA: Thermo Nicolet, 2001, 8 s. Dostupné z: <http://mmrc.caltech.edu/FTIR/FTIRintro.pdf>
86. ROSSMAN, George R. *Ge 116 - Analytical Techniques in Geochemistry*. Pasadena, California, USA: CALTECH, Division of Geological and Planetary Sciences. 16-Feb-2012 [cit. 3.12.2015]. Dostupné z: <http://minerals.gps.caltech.edu/Ge116/Index.html>.
87. National University of Singapore, FS. *Fourier transform infra-red (FTIR) spectroscopy*. Singapore: Faculty of Science, Department of Physics, National University of Singapore. 12 s. Dostupné z: <http://www.physics.nus.edu.sg/~L3000/Level3manuals/FTIR.pdf>
88. BRUKER OPTICS, Inc. *Attenuated Total Reflection (ATR) Mode – Advantages for FT-IR Spectroscopy*. Bruker Optics, 16. Sept, 2013 [cit. 5.1.2016]. Dostupné z: <http://www.azom.com/article.aspx?ArticleID=5958>.

89. PIKE TECHNOLOGIES. *ATR - Theory and Applications*. Application Note ed. Madison, WI, USA: PIKE Technology, 2011 [cit. 4.1.2016]. Dostupné Z: <http://www.piketech.com/files/pdfs/ATRAN611.pdf>
90. SUGA, Shigemasa a Akira SEKIYAMA. *Photoelectron Spectroscopy. Bulk and Surface Electronic Structures*. Springer-Verlag Berlin Heidelberg, 2014. XVIII, 378 s. ISBN 978-3-642-37529-3. Springer Series in Optical Sciences, Vol. 176.
91. HOFMANN, Siegfried. *Auger- and X-ray Photoelectron Spectroscopy in Materials Science. A User-Oriented Guide*. Springer-Verlag Berlin Heidelberg, 2013. XX, 528 s. ISBN 978-3-642-27380-3. Springer Series in Surface Sciences, Vol. 49.
92. HÜFNER, Stephan. *Photoelectron Spectroscopy. Principles and Applications*. Springer-Verlag Berlin Heidelberg, 2003. XV, 662 s. ISBN 978-3-540-41802-3. Advanced Text in Physics.
93. MARTÍNEZ, Lidia, Elisa ROMÁN a Roman NEVSHUPA. X-ray Photoelectron Spectroscopy for Characterization of Engineered Elastomer Surfaces. *Advanced Aspects of Spectroscopy*. 2012, s. 165-194.
94. SÜZER, Sefik. Electron Spectroscopy for Material Characterization. *Turkish Journal of Chemistry*. 1998, vol. 22, s. 309-319.
95. MOULDER, J. F. a J. CHASTAIN. *Handbook of X-ray Photoelectron Spectroscopy: A Reference Book of Standard Spectra for Identification and Interpretation of XPS Data*. Physical Electronics, 1995. ISBN 9780964812413.
96. HAASCH, R. T. X-ray Photoelectron and Auger Electron Spectroscopy. *Practical Materials Characterization*. 2014, s. 99-132.
97. MARTIN, P. M. *Handbook of Deposition Technologies for Films and Coatings: Science, Applications and Technology*. Elsevier Science, 2009. ISBN 9780815520320.
98. SMART, Roger, Stewart MCINTYRE a Igor BELLO. *X - ray photoelectron spectroscopy*. Berlin: 2011. 14-14 s.
99. Universität Konstanz, Clusterphysics Group Ganteför. *Cluster ion deposition*. Universität Konstanz, 2009 [cit. 5.10.2015]. Dostupné z: <http://cms.uni-konstanz.de/en/cluster-ion-deposition/>.

100. LAW, Kock-Yee a Hong ZHAO. *Surface Wetting. Characterization, Contact Angle, and Fundamentals*. Springer International Publishing, 2016. VI, 193 s. ISBN 978-3-319-25212-4.
101. YUAN, Yuehua a T. R. LEE. *Surface Science Techniques*. 2013. ISBN 978-3-642-34242-4.
102. KETELSON, Howard A. et al. Exploring the Science and Technology of Contact Lens Comfort. Is there more we can do to improve comfort and reduce dropouts?. *Contact Lens Spectrum*. 2011, no. September.
103. TOMKOVÁ, E. *Fyzika povrchů*. Prague. 1-18 s. [cit. 5.10.2015]. Dostupné z: http://physics.mff.cuni.cz/kfpp/skripta/Fyzika_povrchu/1_Struktura_povrchu.pdf
104. FOWKES, Frederick M. Attractive Forces at Interfaces. *Industrial & Engineering Chemistry*. 1964, vol. 56, no. 12, s. 40-52. ISSN 0019-7866.
105. HEJDA, F., P. SOLAŠ a J. KOUSAL. Surface Free Energy Determination by Contact Angle Measurements – A Comparison of Various Approaches. *WDS'10 Proceedings of Contributed Papers*. 2010, no. 3, s. 25-30. ISSN 9788073781415.
106. BENIAC, Danie et al. *An introduction to electron microscopy*. 2010. 40-40 s. ISBN 978-0-578-06276-1.
107. GOLDSTEIN, Joseph et al. *Scanning Electron Microscopy and X-ray Microanalysis*. Springer US, 2003. XIX, 690 s. ISBN 978-0-306-47292-3.
108. Jeol Ltd. *SEM: Scanning electron microscope A to Z*. 2009. 32-32 s. TY: GEN. [cit. 5.10.2015]. Dostupné z: <http://www.jeolusa.com/RESOURCES/ElectronOptics/DocumentsDownloads/tabid/320/Default.aspx?EntryId=598>
109. BROWN, Elisabeth. *Spotlight on Science: Scanning Electron Microscopy*. Wordpress, 2014 [cit. 5.10.2015]. Dostupné z: <https://geologelizabeth.wordpress.com/2014/03/26/spotlight-on-science-scanning-electron-microscopy/>.
110. HAFNER, Bob. *Scanning electron microscopy primer*. Minnesota. 2007 [cit. 5.10.2015]. 1-29 s. Dostupné z: http://www.charfac.umn.edu/sem_primer.pdf
111. CAIS, Jaromír. *Elektronová mikroskopie. metalografie. metodická příručka*. Prague: 2015 [cit. 2.1.2016]. 28-28 s. ISBN 978-80-86302-67-6.

112. CHVÁTALOVÁ, Lucie. *Elektronové Mikroskopy*. Brno: 2003 [cit. 3.1.2016]. Dostupné z: http://www.fch.vutbr.cz/~zmeskal/obring/presentace_2003/20_elektronove_mikroskopy.pdf
113. PLECENIK, Andrej a Miroslav ZAHORAN. *Skripta SEM a SPM*. Bratislava, SK: STU. 30-30 s. Dostupné z: http://www.mikroskopia.sk/materials/SKRIPTA_SEM_a_SPM.doc
114. CHENEY, Brandon. *Introduction to scanning electron microscopy*. San Jose State University. 2007 [cit. 5.1.2016]. Dostupné z: <http://www.ncbi.nlm.nih.gov/pubmed/3313016>
115. VOUTOU, Bettina, STEFANAKI, Eleni-chrysanthi a GIANNAKOPOULOS, Kostantinos. *Electron Microscopy : The Basics*. Physics of Advance Materials Winter School 2008 [cit 5.1.2016]. Dostupné z: <https://optiki.files.wordpress.com/2013/03/electron-microscopythe-basics.pdf>
116. SUPPI, Sandra et al. A novel method for comparison of biocidal properties of nanomaterials to bacteria, yeasts and algae. *Journal of Hazardous Materials*. 2015, vol. 286, no. 0, s. 75-84. ISSN 0304-3894.
117. ASADINEZHAD, Ahmad et al. A Physicochemical Approach to Render Antibacterial Surfaces on Plasma-Treated Medical-Grade PVC: Irganon Coating. *Plasma Processes and Polymers*. 2010, vol. 7, no. 6, s. 504-514. ISSN 1612-8869.
118. STREET, Tyler a Scott T. SCHMIDT. *Antimicrobial Susceptibility*. Medscape, 2014 [cit. 5.10.2015]. Dostupné z: <http://emedicine.medscape.com/article/2103786-overview#showall>.
119. ACQUISTO, N. M. Heparin. *Encyclopedia of Toxicology (Third Edition)*. 2014, s. 837–839. ISBN 9780123864550
120. ACTIS, Lisa et al. Antimicrobial surfaces for craniofacial implants: state of the art. *Journal of the Korean Association of Oral and Maxillofacial Surgeons*. 2013, roč. 39, č. 2, s. 43–54.
121. ALAVI, Sajid et al. *Polymers for Packaging Applications*. 2014, s. 486. ISBN 978-1-926895-77-2
122. ALVAREZ-ORDÓÑEZ, Avelino a Miguel PRIETO. *Fourier Transform Infrared Spectroscopy in Food Microbiology*. 2012, s. VI, 55.
123. ATAEEFARD, Maryam et al. Surface Properties of Low Density Polyethylene upon Low-Temperature Plasma Treatment with Various

- Gases. *Plasma Chemistry and Plasma Processing*. 2008, roč. 28, č. 3, s. 377–390. ISSN 0272-4324.
124. BERA, A. a T. BABADAGLI. Status of electromagnetic heating for enhanced heavy oil/bitumen recovery and future prospects: A review. *Applied Energy*. 2015, roč. 151, s. 206–226.
 125. BIRDI, K. S. *Handbook of Surface and Colloid Chemistry, Fourth Edition*. B.m.: CRC Press, 2015. ISBN 9781466596689.
 126. BONEZ, Pauline Cordenonsi et al. Chlorhexidine activity against bacterial biofilms. *American Journal of Infection Control*. 2013, roč. 41, č. 12, s. e119–e122. ISSN 0196-6553.
 127. BRAMBILLA, Marco. Fundamentals of Plasma Physics and Controlled Fusion. *Nuclear Fusion*. 2002, roč. 38, s. 641–642. ISSN 00295515.
 128. BRUKER OPTICS. *Application Note AN # 79 Attenuated Total Reflection (ATR) – a versatile tool for FT-IR spectroscopy Refractive index*. 2011 [cit 5.1.2016]. Dostupné Z: https://www.bruker.com/fileadmin/user_upload/8-PDF-Docs/OpticalSpectroscopy/FT-IR/ALPHA/AN/AN79_ATR-Basics_EN.pdf
 129. CALLEN, James D. Fundamentals of Plasma Physics. *Plasma Physics and Controlled Fusion*. 2003, s. 1–335. ISSN 0741-3335.
 130. CARMONA-RIBEIRO, Ana a Leticia DE MELO CARRASCO. Cationic Antimicrobial Polymers and Their Assemblies. *International Journal of Molecular Sciences*. 2013, roč. 14, č. 5, s. 9906–9946. ISSN 1422-0067.
 131. CARVALHO G. DE AZEVEDO, Tarciana et al. Heparinoids algal and their anticoagulant, hemorrhagic activities and platelet aggregation. *Biomedicine & Pharmacotherapy*. 2009, roč. 63, č. 7, s. 477–483. ISSN 0753-3322.
 132. COATES, John. Interpretation of Infrared Spectra, A Practical Approach. *Encyclopedia of Analytical Chemistry*. 2000, s. 10815–10837. ISSN 00219606.
 133. COONEY, C M. PERSONAL CARE PRODUCTS: Triclosan Comes under Scrutiny. *Environmental health perspectives*. 2010, roč. 118, č. 6, s. A242. ISSN 0091-6765; 1552-9924.

134. CRNS UNIVERSITÉ DE LYON, FRANCE a Stansan International GROUP. *Microfluidics and Lab-on-a-Chip for biomedical applications. Chapter 4: Micromanufacturing*. 2013, roč. Lecture. [cit 5.1.2016]. Dostupné z: <http://www.slideshare.net/stanislas547/sk-microfluidics-and-lab-onachipch4>
135. DE GEYTER, N. a R. MORENT. 7 - Cold plasma surface modification of biodegradable polymer biomaterials. *Biomaterials for Bone Regeneration*. 2014, s. 202–224.
136. DINIS-OLIVEIRA, Ricardo Jorge et al. Clinical and forensic signs related to chemical burns: A mechanistic approach. *Burns*. 2015, roč. 41, č. 4. ISSN 0305-4179.
137. DIXON, Jessica M a Robin L CARVER. Daily chlorohexidine gluconate bathing with impregnated cloths results in statistically significant reduction in central line-associated bloodstream infections. *American Journal of Infection Control*. 2010, roč. 38, č. 10, s. 817–821. ISSN 0196-6553.
138. DONNENBERG, Michael S. *Escherichia Coli (Second Edition) Pathotypes and Principles of Pathogenesis. Escherichia Coli (Second Edition)*. 2013, s. 612. ISBN 978-0-12-397048-0.
139. TEMMERMAN, Eef et al. Surface modification with a remote atmospheric pressure plasma: dc glow discharge and surface streamer regime. *Journal of Physics D: Applied Physics*. 2005, roč. 38, č. 4, s. 505. ISSN 0022-3727.
140. EGERTON, Ray. *Physical Principles of Electron Microscopy. An Introduction to TEM, SEM, and AEM*. 2005, s. XII, 202. ISBN 978-0-387-25800-3.
141. FEI COMPANY. *All you wanted to know about Electron Microscopy ... but didn't dare to ask!*. 2006 [cit. 5.1.2016]. Dostupné z: [http://web.pdx.edu/~pmoeck/pdf/all you wanted to know about electron microscopy.pdf](http://web.pdx.edu/~pmoeck/pdf/all%20you%20wanted%20to%20know%20about%20electron%20microscopy.pdf)
142. FITZPATRICK, Richard. *Plasma Physics graduate lecture at The University of Texas at Austin*. 2006 [cit. 5.1.2016]. Dostupné z: https://www.cfa.harvard.edu/~scanmer/Ay253/LecNotes/fitzpatrick_plasma_physics.pdf
143. FONSECA DE OLIVEIRA, J. et al. Assessment of the effect of Fucus vesiculosus extract on the labeling of blood constituents with technetium-99m and the histological modifications on the shape of the red blood cells.

- Food and Chemical Toxicology*. 2003, roč. 41, č. 1, s. 15–20. ISSN 0278-6915.
144. GIANNELLI, M. et al. Effect of chlorhexidine digluconate on different cell types: A molecular and ultrastructural investigation. *Toxicology in Vitro*. 2008, roč. 22, č. 2, s. 308–317. ISSN 0887-2333.
145. GIBSON, K. et al. Plasma Assisted Decontamination of Biological and Chemical Agents. 2011, NATO Science for Peace and Security Series A: Chemistry and Biology. ISBN 9781402084393.
146. HASAN, Jafar, Russell J. CRAWFORD a Elena P. IVANOVA. Antibacterial surfaces: the quest for a new generation of biomaterials. *Trends in biotechnology*. 2013, roč. 31, č. 5, s. 295–304. ISSN 0167-7799.
147. HLOCH, Ondřej. Základní koagulační vyšetření. 2014 [cit. 30.9.2015]. Dostupné z: <http://new.propedeutika.cz/?p=534>
148. HOFFMANN, Clotilde, Carlos BERGANZA a John ZHANG. Cold Atmospheric Plasma: methods of production and application in dentistry and oncology. *Medical gas research*. 2013, roč. 3, č. 1, s. 21. ISSN 2045-9912.
149. HOLLAS, J. Michael. Modern Spectroscopy. Fourth ed. 2004, s. 483. ISBN 0-470-84416-7.
150. HUMPOLICEK, Petr. et al. Blood coagulation and platelet adhesion on polyaniline films. *Colloids and surfaces.B, Biointerfaces*. 2015, roč. 133, s. 278–285. ISSN 1873-4367; 0927-7765.
151. HUMPOLÍČEK, Petr et al. Blood coagulation and platelet adhesion on polyaniline films. *Colloids and Surfaces B: Biointerfaces*. 2015, roč. 133, č. JUNE, s. 278–285. ISSN 09277765.
152. CHALMERS, John M a Geoffrey DENT. Vibrational Spectroscopic Methods in Pharmaceutical Solid-state Characterization. *Polymorphism*. 2006, s. 95–138.
153. CHAN, C M. *Polymer Surface Modification and Characterization*. B.m.: Hanser, 1994. SPE books. ISBN 9781569901588.

154. CHOI, Jong-il, et al. Effect of gamma irradiation on the structure of fucoidan. *Radiation Physics and Chemistry* . 2014, roč. 100, č. 0, s. 54–58. ISSN 0969-806X.
155. CHUKANOV, Nikita V. a Alexandr D. CHERVONNYI. *Infrared Spectroscopy of Minerals and Related Compounds*. 2016, s. 1200. ISBN 978-3-319-25347-3.
156. JAGANATHAN, SaravanaKumar et al. Review: Radiation-induced surface modification of polymers for biomaterial application. *Journal of Materials Science*. 2015, roč. 50, č. 5, s. 2007–2018. ISSN 0022-2461.
157. JASPER, Joseph J. The surface tension of pure liquid compounds. *Journal of Physical Chemistry Reference Data*. 1972, roč. 1, č. 4, s. 841. ISSN 0021-9797
158. JIN, Jun-O a Qing YU. Fucoidan delays apoptosis and induces pro-inflammatory cytokine production in human neutrophils. *International journal of biological macromolecules*. 2015, roč. 73, č. 0, s. 65–71. ISSN 0141-8130.
159. KARBASSI, Elika et al. Antibacterial Performance of Alginic Acid Coating on Polyethylene Film. *International journal of molecular sciences*. 2014, roč. 15, č. 8, s. 14684–14696.
160. KARBASSI, Elika et al. Bacteriostatic activity of fluoroquinolone coatings on polyethylene films. *Polymer Bulletin*. 2015, roč. 72, č. 8, s. 2049-2058, ISSN 0170-0839.
161. KARKI, S. a A. C. CHENG. Impact of non-rinse skin cleansing with chlorhexidine gluconate on prevention of healthcare-associated infections and colonization with multi-resistant organisms: a systematic review. *Journal of Hospital Infection*. 2012, roč. 82, č. 2, s. 71–84. ISSN 0195-6701.
162. KIM, Do-Yeong a Weon-Sun SHIN. Unique characteristics of self-assembly of bovine serum albumin and fucoidan, an anionic sulfated polysaccharide, under various aqueous environments. *Food Hydrocolloids*. 2015, roč. 44, č. 0, s. 471–477. ISSN 0268-005X.
163. KIM, Jong Min et al. A method for coating fucoidan onto bare metal stent and in vivo evaluation. *Progress in Organic Coatings*. 2015, roč. 78, č. 0, s. 348–356. ISSN 0300-9440.

164. KNAB, Joseph, Jing-Yin CHEN a Andrea MARKELZ. Hydration Dependence of Conformational Dielectric Relaxation of Lysozyme. *Biophysical journal*. 2006, roč. 90, č. 7, s. 2576–2581. ISSN 0006-3495.
165. KUBIAK, K. J. et al. Wettability versus roughness of engineering surfaces. *The 12th International Conference on Metrology and Properties of Engineering Surfaces*. 2011, roč. 271, č. 3–4, s. 523–528. ISSN 0043-1648.
166. LEE, Eun Ju a Kwang-Hee LIM. Relative charge density model on chitosan–fucoidan electrostatic interaction: Qualitative approach with element analysis. *Journal of Bioscience and Bioengineering*. 2015, roč. 119, č. 2, s. 237–246. ISSN 1389-1723.
167. LI, Ning, Quanbin ZHANG a Jinming SONG. Toxicological evaluation of fucoidan extracted from *Laminaria japonica* in Wistar rats. *Food and Chemical Toxicology*. 2005, roč. 43, č. 3, s. 421–426. ISSN 0278-6915.
168. LIM, Sangyong, Jong-il CHOI a Hyun PARK. Antioxidant activities of fucoidan degraded by gamma irradiation and acidic hydrolysis. *Radiation Physics and Chemistry*. 2015, roč. 109, č. 0, s. 23–26. ISSN 0969-806X.
169. LÓPEZ GARCÍA, Jorge et al. Cell Proliferation of HaCaT Keratinocytes on Collagen Films Modified by Argon Plasma Treatment. *Molecules*. 2010, roč. 15, č. 4, s. 2845–2856. ISSN 1420-3049.
170. LÓPEZ-GARCÍA, Jorge et al. Enhanced printability of polyethylene through air plasma treatment. *Vacuum*. 2013, roč. 95, č. 0, s. 43–49. ISSN 0042-207X.
171. LÓPEZ-GARCÍA, Jorge et al. Polyphenolic Extracts of Edible Flowers Incorporated onto Atelocollagen Matrices and Their Effect on Cell Viability. *Molecules*. 2013, roč. 18, č. 11, s. 13435–13445. ISSN 1420-3049.
172. LÓPEZ-GARCÍA, Jorge et al. HaCaT Keratinocytes Response on Antimicrobial Atelocollagen Substrates: Extent of Cytotoxicity, Cell Viability and Proliferation. *Journal of Functional Biomaterials*. 2014, roč. 5, č. 2, s. 43–57.
173. MAKI, D. G., C. J. ALVARADO a M. RINGER. Prospective randomised trial of povidone-iodine, alcohol, and chlorhexidine for prevention of

- infection associated with central venous and arterial catheters. *Lancet*. 1991, roč. 338, č. 8763, s. 339–343. ISSN 0140-6736.
174. MARANO, C. et al. Effects of coating composition and surface pre-treatment on the adhesion of organic–inorganic hybrid coatings to low density polyethylene (LDPE) films. *European Polymer Journal*. 2009, roč. 45, č. 3, s. 870–878. ISSN 0014-3057.
175. MAXDORF, s. r. o. Velký lékařský slovník. 2015 [cit. 10.10.2015]. Dostupné z: <http://lekarske.slovníky.cz/lexikon-pojem>
176. MENYHAY, S. Z. a D. G. MAKI. Disinfection of needleless catheter connectors and access ports with alcohol may not prevent microbial entry: the promise of a novel antiseptic-barrier cap. *Infection control and hospital epidemiology: the official journal of the Society of Hospital Epidemiologists of America*. 2006, roč. 27, č. 1, s. 23–27. ISSN 0899-823X; 0899-823X.
177. MONTECALVO, Marisa A. et al. Chlorhexidine Bathing to Reduce Central Venous Catheter-associated Bloodstream Infection: Impact and Sustainability. *The American Journal of Medicine*. 2012, roč. 125, č. 5, s. 505–511. ISSN 0002-9343.
178. MORENT, R. et al. Study of the ageing behaviour of polymer films treated with a dielectric barrier discharge in air, helium and argon at medium pressure. *Surface and Coatings Technology*. 2007, roč. 201, č. 18, s. 7847–7854. ISSN 0257-8972.
179. MOURIER, Pierre et al. Quantitative compositional analysis of heparin using exhaustive heparinase digestion and strong anion exchange chromatography. *Analytical Chemistry Research*. 2015, roč. 3, č. 0, s. 46–53. ISSN 2214-1812.
180. MRAD, O. et al. Aging of a medical device surface following cold plasma treatment: Influence of low molecular weight compounds on surface recovery. *European Polymer Journal*. 2011, roč. 47, č. 12, s. 2403–2413. ISSN 0014-3057.
181. IDOTA, Naokazu et al. Novel temperature-responsive polymer brushes with carbohydrate residues facilitate selective adhesion and collection of hepatocytes. *Science and Technology of Advanced Materials*. 2012, roč. 13, č. 6, s. 64206. ISSN 1468-6996.

182. NARDELLO-RATAJ, V. a L. LECLERCQ. Encapsulation of biocides by cyclodextrins: toward synergistic effects against pathogens. *Beilstein journal of organic chemistry*. 2014, roč. 10, s. 2603–2622. ISSN 1860-5397.
183. NAVARRO, Rodrigo et al. Preparation of Surface-Attached Polymer Layers by Thermal or Photochemical Activation of α -Diazoester Moieties. *Langmuir*. 2013, roč. 29, č. 34, s. 10932–10939. ISSN 0743-7463.
184. NI, H. et al. Self-decontaminating properties of fluorinated copolymers integrated with ciprofloxacin for synergistically inhibiting the growth of *Escherichia coli*. *Journal of biomaterials science. Polymer edition*. 2014, roč. 25, č. 17, s. 1920–1945. ISSN 1568-5624; 0920-5063.
185. NIE, Chuanxiong et al. Novel heparin-mimicking polymer brush grafted carbon nanotube/PES composite membranes for safe and efficient blood purification. *Journal of Membrane Science*. 2015, roč. 475, č. 0, s. 455–468. ISSN 0376-7388.
186. PAISOONSIN, Sutida, Orathai PORNSUNTHORNTAWEE a Ratana RUJIRAVANIT. Preparation and characterization of ZnO-deposited DBD plasma-treated PP packaging film with antibacterial activities. *Applied Surface Science*. 2013, roč. 273, č. 0, s. 824–835. ISSN 0169-4332.
187. PANDIYARAJ, K. Navaneetha et al.. Influence of non-thermal plasma forming gases on improvement of surface properties of low density polyethylene (LDPE). *Applied Surface Science*. 2014, roč. 307, č. 0, s. 109–119. ISSN 0169-4332.
188. PANKAJ, Shashi Kishor. Applications of Cold Plasma Technology in Food Packaging. *Trends in Food Science & Technology*. 2014, roč. 35, s.5-17
189. PÉREZ-PERRINO, Mónica et al. Binding of Functionalized Polymers to Surface-Attached Polymer Networks Containing Reactive Groups. *Macromolecules*. 2014, roč. 47, č. 8, s. 2695–2702. ISSN 0024-9297.
190. POPELKA, Anton et al. Antibacterial treatment of LDPE with halogen derivatives via cold plasma. *EXPRESS Polymer Letters*. 2015, roč. 9, č. 5, s. 402–411.

191. POPELKA, Anton et al. Anti-bacterial Treatment of Polyethylene by Cold Plasma for Medical Purposes. *Molecules*. 2012, roč. 17, č. 12, s. 762–785. ISSN 1420-3049.
192. RIBEIRO, Daniel Araki et al. Genotoxicity of antimicrobial endodontic compounds by single cell gel (comet) assay in Chinese hamster ovary (CHO) cells. *Oral Surgery, Oral Medicine, Oral Pathology, Oral Radiology, and Endodontology*. 2005, roč. 99, č. 5, s. 637–640. ISSN 1079-2104.
193. SADEGHNEJAD, Abdolhamid et al. Antibacterial nano silver coating on the surface of polyethylene films using corona discharge. *Surface and Coatings Technology*. 2014, roč. 245, č. 0, s. 1–8. ISSN 0257-8972.
194. SAWANT, S. D., A. A. BARAVKAR a R. N. KALE. FT-IR spectroscopy: Principle, technique and mathematics. *International Journal of Pharma and Bio Sciences*. 2011, roč. 2, č. 1, s. 513–519. ISSN 09756299.
195. SENTHILKUMAR, Kalimuthu a Se-Kwon KIM. Chapter Eleven - Anticancer Effects of Fucoidan. *Marine Carbohydrates: Fundamentals and Applications, Part A*. 2014, roč. 72, č. 0, s. 195–213. ISSN 1043-4526.
196. SHEN, Ya, Sonja STOJICIC a Markus HAAPASALO. Antimicrobial Efficacy of Chlorhexidine against Bacteria in Biofilms at Different Stages of Development. *Journal of endodontics*. 2011, roč. 37, č. 5, s. 657–661. ISSN 0099-2399.
197. SCHUH, Kerstin, Oswald PRUCKER a Jürgen RÜHE. Tailor-Made Polymer Multilayers. *Advanced Functional Materials*. 2013, roč. 23, č. 48, s. 6019–6023. ISSN 1616-3028.
198. SIOW, Kim Shyong et al. Plasma methods for the generation of chemically reactive surfaces for biomolecule immobilization and cell colonization - A review. *Plasma Processes and Polymers*. 2006, roč. 3, č. 6-7, s. 392–418. ISSN 16128850.
199. ŠIMKOVIC, Ivan et al. Cationization of heparin for film applications. *Carbohydrate Polymers*. 2015, roč. 115, č. 0, s. 551–558. ISSN 0144-8617.

200. ŠURANSKÝ, Martin. *Depozice polysiloxanových vrstev v nízkoteplotním plazmatu*. 2014, Master thesis. Tomas Bata University in Zlín, Faculty of Technology, s. 94.
201. ŠVORČÍK, V. et al. Modification of surface properties of high and low density polyethylene by Ar plasma discharge. *Polymer Degradation and Stability*. 2006, roč. 91, č. 6, s. 1219–1225. ISSN 0141-3910.
202. THEJASWINI, H. C. *Atmospheric-Pressure Dielectric Barrier Discharge: Synthesis and Deposition of Organic Plasma Polymers and their Characterizations*. B.m., 2012. Ernst-Moritz-Arndt-Universität Greifswald.
203. THOME, I. P. S. et al. Bactericidal Low Density Polyethylene (LDPE) urinary catheters: Microbiological characterization and effectiveness. *Materials Science & Engineering C-Materials for Biological Applications*. 2012, roč. 32, č. 2, s. 263–268. ISSN 09284931.
204. THUY, Thanh Thi Thu et al. Anti-HIV activity of fucoidans from three brown seaweed species. *Carbohydrate Polymers*. 2015, roč. 115, č. 0, s. 122–128. ISSN 0144-8617.
205. VAN DEYNSE, Annick et al. Influence of ambient conditions on the aging behavior of plasma-treated polyethylene surfaces. *Surface and Coatings Technology*. 2014, roč. 258, č. 0, s. 359–367. ISSN 0257-8972.
206. VEENA, Coothan Kandaswamy et al. Beneficial role of sulfated polysaccharides from edible seaweed *Fucus vesiculosus* in experimental hyperoxaluria. *Food Chemistry*. 2007, roč. 100, č. 4, s. 1552–1559. ISSN 0308-8146.
207. VERALDI, Noemi et al. Heparin derivatives for the targeting of multiple activities in the inflammatory response. *Carbohydrate Polymers*. 2015, roč. 117, č. 0, s. 400–407. ISSN 0144-8617.
208. WESSELS, Stephen a Hanne INGMER. Modes of action of three disinfectant active substances: A review. *Regulatory Toxicology and Pharmacology*. 2013, roč. 67, č. 3, s. 456–467. ISSN 0273-2300.
209. WIJESINGHE, W. A. J. P. a You-Jin JEON. Biological activities and potential industrial applications of fucose rich sulfated polysaccharides and fucoidans isolated from brown seaweeds: A review. *Carbohydrate Polymers*. 2012, roč. 88, č. 1, s. 13–20. ISSN 0144-8617.

210. WORZ, A. et al. Protein-resistant polymer surfaces. *Journal of Materials Chemistry*. 2012, roč. 22, č. 37, s. 19547–19561. ISSN 0959-9428.
211. WU, X. Z. a D. CHEN. Effects of sulfated polysaccharides on tumour biology. *West Indian Medical Journal*. 2006, roč. 55, č. 4, s. 270–273.
212. ZENG, Pengyun et al. Concentration dependent aggregation properties of chlorhexidine salts. *International journal of pharmaceutics*. 2009, roč. 367, č. 1–2, s. 73–78. ISSN 0378-5173.

List of figures

Figure 1	Bacterial colonization stages	11
Figure 2	General process of antibacterial agent immobilization onto pre-activated surface	15
Figure 3	Chlorhexidine's chemical structure	17
Figure 4	Mechanism of chlorhexidine action	18
Figure 5	Chemical structure of triclosan	19
Figure 6	E. coli	20
Figure 7	S. aureus	21
Figure 8	Low-temperature atmospheric pressure plasma sources	22
Figure 9	Electromagnetic spectrum	36
Figure 10	Schematic TPI Spectra 3000 showing coherent detection mechanism (left), Tera OSCAT spectrometer layout (right).....	43
Figure 11	2D THz imaging	45
Figure 12	Example of FTIR spectrometer NICOLET layout by Thermo Electron Corporation	50
Figure 13	Example of ATR FTIR spectrometer layout	51
Figure 14	X-ray photoelectron spectroscopy layout.....	56
Figure 15	Droplet profile analysis	58
Figure 16	Surface tension and contact angles.....	60
Figure 17	Scanning electron microscopy layout.....	64
Figure 18	Signals and their origination from different volumes of interaction	67
Figure 19	Disk diffusion method	69
Figure 20	SEM micrographs	77
Figure 21	Comparison of all ATR-FTIR spectroscopy spectra.....	79
Figure 22	General graph of ATR-FTIR spectroscopy samples after plasma treatment with bonded monomers	80
Figure 23	General graph of ATR-FTIR spectroscopy samples after plasma treatment with bonded monomers and antibacterials	81
Figure 24	Example of antibacterial tests after 24 hours	85
Figure 25	Comparison of refractive indices obtained from Tera OSCAT	90
Figure 26	General graph of ATR THz spectroscopy refractive indices for antibacterial samples.....	91
Figure 27	Dielectric constant (real part) of antibacterial surfaces.....	92
Figure 28	Dielectric constant (imaginary part) of antibacterial surfaces.....	93

Figure 29	General graph of absorbance spectra – samples with antibacterial compounds	95
Figure 30	Transmittance of antibacterial surfaces with Triclosan (left) and Chlorhexidine (right) from ATR (TPS Spectra™).....	97
Figure 31	THz 3D imaging examination of antibacterial surface (the red layer is the surface, the blue colour belongs to golden mirror).....	98
Figure 32	THz 2D imaging examination of antibacterial surface (sample 3) layer thickness.....	99
Figure 33	THz 2D & 3D imaging examination of antibacterial surface layer with air pocket	99

List of tables

Table 1	Commonly used polymers in medicine	12
Table 2	Plasma divided according to temperature	24
Table 3	The properties of commonly used ATR crystals	52
Table 4	Examples of surface tension components‘ values for selected liquids	59
Table 5	Characteristics of commonly used electron guns.....	65
Table 6	Prepared and characterized (antibacterial) surfaces.....	74
Table 7	Contact angle measurements data of different samples	74
Table 8	Surface energy values.....	75
Table 9	Surface elemental compositions and ratios of samples.....	82
Table 10	Inhibition zone area measurement after 24 hours	84
Table 11	Inhibition zone area measurement after 12/24 hours in repetitive test after 6 months	87
Table 12	Descriptive statistics of refractive indices (by Tera OSCAT).	88
Table 13	Descriptive statistics of dielectric properties (ϵ_r).	94

List of symbols and abbreviations

<i>A. baumannii</i>	<i>Acinetobacter baumannii</i>
$(AB^+)^*$	Vibrationally excited ion
$[C]$	Weighting factors/concentrations matrix
$[D]$	Recorded XPS data matrix
$[R]$	Independent component spectra matrix
$\langle\sigma v\rangle$	Reaction rate coefficient
$\langle v_e\rangle$	Averaged thermal velocity of electrons
$2D$	2-dimensional
$3D$	3-dimensional
A	Collision partner; absorbance
a	Atom
a_0	Bohr radius
AA	Allylamine
$AB^-(v_i)$	Non-stable intermediate negative ion
AMA	<i>N</i> -allylmethylamine
ATR	Attenuated total reflection
B	Collision partner
b	Impact parameter
$B(\bar{\nu}), \bar{\nu}$	Apectral power density at particular wavenumber
BSE	Backscattered electrons
c	Apeed of light
CCM	Czech collection of microorganism
CCP	Capacitively coupled discharge
CFU	Colony-forming unit
CHX	Products containing chlorhexidine
$\cos\theta_{zd}$	Contact angle on rough surface
C_x	Atom fraction determination
D	Lens diameter; optical path difference
d	Material thickness; thickness
d_0	Resolution of display
$DMAA$	<i>N,N</i> -dimethylallylamine
d_p	Penetration depth; resolution of scanned specimen
E	Electric field
e	Charge
<i>E. coli</i>	<i>Escherichia coli</i>
E_0	Amplitude
$E_0 - E_n$	Quantized discrete energy levels
E_B	Binding energy of the electron in the atom

<i>EBS</i>	Electron backscatter diffraction
<i>EEDF</i>	Electron energy distribution function
<i>EDS/WDS</i>	Energy dispersive spectrometer
E_F	Fermi level energy
E_K	Kinetic energy of emitted electrons
<i>ENR</i>	Enoyl-acyl carrier protein reductase
<i>EPA</i>	Environmental Protection Agency
E_{pas}	Pass energy
E_V	Vacuum level energy
f	Focal length
$f(\epsilon)$	Electron energy distribution function
$f(v)$	Velocity distribution function
$f\#$	F-number
<i>FA</i>	Factor analysis
<i>FDA</i>	Food and Drug Administration
<i>FE</i>	Field emission
<i>FEG</i>	Field emission gun
<i>FFT</i>	Fast Fourier-transform
f_{ik}	Force of oscillator for transition $i \rightarrow k$
<i>FIR</i>	Far-infrared
fs	Femtosecond
<i>FTIR</i>	Fourier Transform InfraRed (spectroscopy)
g_{AB}, g_{AB} and g_e	Statistical weights
h	Planck constant; height
<i>HCAIS</i>	Health-care associated infections
$\hbar\Gamma_i$	Energy width of resonance pikes
$h\nu$	Incident photon energy
I	Ionization potential; transmitted intensity
i	Transition from one atomic state to another one (k); oscillator
$I(\delta)$	Relationship between intensity falling on detector
I_0	Initial light source intensity
II	Interface index
<i>IR</i>	Infrared
I_x	Peak are
j	Current density
k	Boltzmann constant; force constant
<i>K.E.</i>	Kinetic energy
k_{e0}	Gas-kinetic rate coefficient
$k_i(T_e)$	Ionization rate coefficient

<i>KRS-5</i>	Thallium bromoiodide
<i>l</i>	Orbital moment
<i>LD₅₀</i>	Median lethal dose
<i>LDPE</i>	Low-density polyethylene
<i>LLSF</i>	Linear least squares fitting
<i>LTE</i>	Local thermodynamic equilibrium
<i>m, M</i>	Mass
<i>m₀</i>	Rest mass of the electron
<i>M²</i>	M-square-value
<i>MIR</i>	Mid-infrared
<i>mmW</i>	Microwave
<i>m_n</i>	Mass of atom
<i>MRSA</i>	Methicillin-resistant <i>Staphylococcus aureus</i>
<i>n</i>	Refractive index; quantum number
\hat{n}	Complex refractive index
<i>n(z)</i>	Refractive index in z direction
<i>n, l, j</i>	Quantum number
<i>n₁</i>	Refractive index of sample
<i>n₂</i>	Refractive index of crystal
<i>NAD⁺</i>	Nicotinamide adenine dinucleotide
<i>n_B</i>	Particle B concentration
<i>n_e</i>	Plasma density (electron)
<i>n_i</i>	Plasma density (ion)
<i>NIR</i>	Near-infrared
<i>nsinα</i>	Numeric aperture
<i>N_x</i>	Number of elements moles
<i>OWRK</i>	Owen-Wendt-Rabel-Kaelble method
<i>p</i>	Pressure; relativistic momentum of electron
<i>P. aeruginosa</i>	<i>Pseudomonas aeruginosa</i>
<i>q</i>	Complex radius of curvature
<i>r</i>	Radius
<i>R</i>	Radius of the circle projected over the droplet; curvature radius
<i>R(z)</i>	Radius of curvature
<i>R₀</i>	Sample's surface reflection amplitude
<i>r₀</i>	Radius of droplet
<i>RF</i>	Radiofrequency
<i>r_{in}</i>	Incoming ray
<i>R_n</i>	n th interface reflection amplitude
<i>r_{out}</i>	Resulting ray

R_y	Rydberg constant
s	Spin
<i>S. aureus</i>	<i>Staphylococcus aureus</i>
<i>S. enterica</i>	<i>Salmonella enterica</i>
<i>SD</i>	Standard deviation
<i>SE</i>	Secondary electrons; standard error
<i>SEE system</i>	Surface energy evaluation system
<i>SEM</i>	Scanning electron microscopy
<i>STEM</i>	Scanning transmission electron microscopy
S_x	Atomic sensitivity factor
T	Transmittance
T_0	Temperature of heavy particles
<i>TDS</i>	Time-domain
T_e	Electron temperature
<i>TEM</i>	Transmission electron microscope
<i>TEM₀₀</i>	Transverse electric and magnetic mode
<i>THz</i>	Terahertz
T_i	Ions temperature
<i>TPI</i>	Terahertz pulsed imaging
<i>TPS</i>	Terahertz pulsed spectroscopy
T_r	Temperature of rotational molecules degrees of freedom
T_v	Temperature of vibrational excitation of molecules
U	Coulomb interaction energy; electric potential
<i>UHV</i>	Ultra-high vacuum
<i>UV</i>	Ultra-violet
v	Velocity
v/v	Volume concentration (volume/volume)
w	Gaussian beam waist radius
$w(z)$	Gaussian beam radius
w/v	Mass concentration (mass/volume)
$W_A^{p/d}$	Adhesion work
x	Constituent
<i>XPS</i>	X-ray photoelectron spectroscopy
Z	Wave's impedance
z	THz beam direction
Z_m	Magnification
z_R	Rayleigh range
Z_v	Number of valence electrons in atom
α	Linear absorption coefficient

γ	Average fraction of kinetic energy transferred; damping constant
γ^-	Electron-donor part of free surface energy
γ^+	Electron-acceptor part of free surface energy
γ^{AB}	Polar component (acid-base) of surface tension
γ^C	Coulomb forces
γ^D	Dispersion powers
γ^d	Dispersion part/component
Γ_i	Probability of $AB^-(v_i)$ decay through channels
γ^I	Induction powers
γ_{lg}	Liquid-gaseous phase
γ^{LW}	Dispersion component (Lifshitz-van der Walls) of surface energy
γ^n	Non-dispersion part
γ^p	Polar component
γ_{sg}	Solid-gaseous phase
γ_{sl}	Solid-liquid phase
γ^{tot}	Total surface energy
Δ	Resolution
ΔE_{li}	Energy of transition to the intermediate state
ΔE_{chem}	Chemical shift
ΔE_{ik}	Energy of transition
ΔE_{Mad}	Madelung constant
ΔE_{rel}	Relaxation effect
Δt	Time delay
$\Delta \varepsilon$	Energy transferred to the valence electron
ε	Relative dielectric permittivity; kinetic energy, surface roughness
ε_r	Dielectric constant – real part
ε_v	Kinetic energy of the valence electron
θ	Incident radiation angle; opening angle, electron take-off angle, wetting angle
θ'	Viewing angle
θ_D	Diiodomethane
θ_E	Ethylene glycol
θ_W	Deionized water
λ	Mean free path; wavelength; attenuated length; electron wavelength
μ	Relative magnetic permeability; reduced mass
ν	Interaction frequency; wavenumber

σ	Dependence of cross section
$\sigma_{ik}(\varepsilon)$	Dependence for excitation in electronic terms
τ	Period of oscillation
v	Relative velocity
v_i	Vibrational quantum number of non-stable negative ion
w	Number of elementary processes
ϕ	Complex phase
Φ_1, Φ_2	Relative representation in measured solid surface
ϕ_a	Analyser function
ϕ_{in}	Ray slope
ϕ_{out}	Resulting ray slope
ω_0	Oscillator resonance frequency
ω_p	Plasma frequency
θ_D	Contact angle of diiodomethane
θ_E	Contact angle of ethylene glycol
θ_W	Contact angle of deionized water

Author's publication activities

Papers in journals with impact factor:

BÍLEK, František, SULOVSÁ, Kateřina, LEHOCKÝ, Marián, SÁHA, Petr, HUMPOLÍČEK, Petr, MOZETIČ, Miran and JUNKAR, Ita. Preparation of active antibacterial LDPE surface through multistep physicochemical approach II: Graft type effect on antibacterial properties. *Colloids and Surfaces B: Biointerfaces*. 2013, vol. 102, s. 842-848. doi:10.1016/j.colsurfb.2012.08.026

Kateřina SULOVSÁ and Marián LEHOCKÝ. Terahertz Spectroscopy Characterization of Antibacterial Surfaces Prepared via Multistep Physicochemical Procedure. *Optical Engineering*. 2015; 54(3):034107. doi: 10.1117/1.OE.54.3.034107

Papers in conference proceedings:

Kateřina SULOVSÁ and Marián LEHOCKÝ. *Characterization of plasma treated surfaces for food safety by terahertz spectroscopy*. Proc. SPIE 9252, Millimetre Wave and Terahertz Sensors and Technology VII, 925209 (October 7, 2014); doi:10.1117/12.2067162 (**invited paper**)

BÍLEK, František, SULOVSÁ, Kateřina and LEHOCKÝ, Marián. *Graft type effect on antibacterial properties of LDPE*. In PLASTKO 2012. Zlín: Univerzita Tomáše Bati ve Zlíně, 2012, s. 1-6. ISBN 978-80-7454-137-7

Curriculum Vitae

Name Kateřina Sulovská
Address Beckovská 2687, 760 01 Zlín, the Czech Republic
E-mail kachenka9@gmail.com

Nationality Czech
Date of birth 12th November 1984
Gender Female

Work experience

10.1.2013 – present Assistant & Junior Research, Tomas Bata University in Zlín, Faculty of Applied Informatics
03.01. – 9.30.2013 Researcher – Ph.D. student, Security research, The Centre for Security, Information and Advanced Technologies, Tomas Bata University in Zlín
11. 03. - 11. 30. 2010 Trainee, Zlín Regional Authority, Department of Trade and the Regional Legal Office
10. 11. - 10. 12. 2007 Organiser of the 9th general meeting of Association of Primary Art Schools of the Czech Republic
6. 3. - 8. 31. 2004 Cashier – Shop assistant, SPAR Czech Republic, s.r.o.,
7. 1. - 7. 20. 2003, Assistant of director, MEDITRONIC s.r.o
8. 23. - 12. 31. 2002

Education and training

2011 – present Chemistry and Materials Technology: Technology of Macromolecular Compounds, Tomas Bata University in Zlín, Faculty of Technology
2009 – present Engineering Informatics: Engineering Informatics, Tomas Bata University in Zlín, Faculty of Applied Informatics
2009 – 2011 Chemistry and Materials Technology: Technological Risk Management, Tomas Bata University in Zlín, Faculty of Technology
2004 – 2009 Engineering Informatics: Security Technologies, Systems and Management, Tomas Bata University in Zlín, Faculty of Applied Informatics, Zlín, the Czech Republic
2000 – 2004 Economic lyceum, Secondary Technical School Zlín

Personal skills and competences

Mother tongue(s) Czech language
Other languages English (C1, FCE certificate), German (A2), French (A1)

Other experiences

Senator of the Academic Senate of Faculty of Applied Informatics, Tomas Bata University in Zlín (2. 20. 2012 – 12. 31. 2014), Student chamber, member of Legislative Committee

Senator of the Academic Senate of Tomas Bata University in (3. 6. 2007 - 3. 6. 2010, 6. 29. 2010 – 7. 3. 2013), Student chamber, member of Legislative Committee, representative of the Timetable Commission, representative of the Council for Information Systems

Tutoring English language and Maths

Gastroma a.s. – interpreting activities (2004 - 2005)

Supermarket Albert - cashier (2003)

Organization of balls for the Primary Art School Zlín – Jižní Svahy (2002 - 2008)

Creation of promotional materials for the Primary Art School Zlín – Jižní Svahy (2000 - 2008)

Research/study fellowships

2003 - Vrij Technisch Instituut, Izegem, Belgium

R&D Projects

IGA/FAI/2012/016

IGA/FAI/2013/001

IGA/FAI/2014/001

CZ.1.05/2.1.00/03.0089

LO1303

Kateřina Sulovská

Preparation and Characterization of Antibacterial Surfaces

Připrava a charakterizace antibakteriálních povrchů

Doctoral Thesis

Published by Tomas Bata University in Zlín,
nám. T. G. Masaryka 5555, 760 01 Zlín.

Number of copies: 9

Composition: Kateřina Sulovská

Publication did not undergo linguistic or editorial adjustments.

Year of publication: 2016